Pt/TiO_2 Photocatalysts Synthesized by Atomic Layer Deposition

by

Yun Zhou

B.S., East China Normal University, P.R. China, 2001

A thesis submitted to the
Faculty of the Graduate School of the
University of Colorado in partial fulfillment
of the requirement for the degree of
Doctor of Philosophy
Department of Chemical and Biological Engineering
2011

This thesis entitled:

Pt/TiO_2 Photocatalysts Synthesized by Atomic Layer Deposition

Written by Yun Zhou

Has been approved for the Department of Chemical and Biological engineering

_____

Alan W. Weimer

_____

Charles B. Musgrave

_____

Date

The final copy of this thesis has been examined by the signatories, and we find that both the content and the form meet acceptable presentation standards of scholarly work in the above mentioned discipline.

ABSTRACT

Zhou, Yun (Ph.D., Chemical and Biological Engineering)

Pt/TiO_2 Photocatalysts Synthesized by Atomic Layer Deposition (ALD)

Thesis directly by Professor Alan W.Weimer

Photocatalytic oxidation is a promising technique for environmental pollutants remediation. TiO_2 is widely used as a photocatalyst due to its superior characteristics such as high photoactivity, chemical stability and low cost. This dissertation focuses on the TiO_2 photocatalyst and its modification for environmental applications, through both experimental and theoretical methods.

The experimental method is by the atomic layer deposition (ALD) technique, including two major parts. One is to deposit TiO_2 ALD thin films on magnetic core particles to create a magnetic photocatalyst. This novel composite material is both magnetic and photocatalytically active, providing for a promising strategy for environmental treatment. The other is to deposit Pt nanoparticles on TiO_2 photocatalyst to increase the photoactivity. The Pt/TiO_2 photocatalyst with high Pt surface dispersion was synthesized by optimizing the Pt ALD deposition temperature and the Pt loading, resulting in a significant improvement on the TiO_2 photoactivity. One ALD cycle of Pt deposited TiO_2 has been demonstrated to increase the photoactivity of TiO_2 nanoparticles by threefold for decomposition of methylene blue with the Pt loading of 0.64 wt%.

The theoretical work is via density functional theory (DFT), involving the study of the Pt particle growth on TiO_2 surfaces and the effect of the Pt deposition on the photoactivity of TiO_2. The Pt was found to prefer 3D rather than 2D growth, due to the large cohesive energy of Pt.

Large particles are thermodynamically favorable, however the low mobility of Pt over the TiO_2 surface coupled with the high desorption barrier for Pt detaching from particles limits the large particle growth. This results in a large number of small particles during Pt ALD processing. The role of the Pt deposition on the photoactivity of TiO_2 was explored. The initial increase and subsequent decrease in TiO_2's photoactivity with increasing Pt loading was explained by the competition between increased O_2 adsorption induced by Pt and the electron-hole recombination in Pt. For Pt loadings above the optimum level, the increased electron-hole recombination outweighs the increased O_2 adsorption, which is limited by its concentration and diffusion in solution.

Dedicated to my husband, Mingming

ACKNOWLEDGEMENTS

I would like to express my sincere gratitude and appreciation to many individuals who made this thesis possible.

It is difficult to overstate my gratitude to my advisor, Professor Alan W. Weimer. I know I owe a great debt of gratitude for him. It is him who offered me the opportunity to pursue my degree in this department. It is him who provided me the chances to make up the essential chemical engineering knowledge, from a different undergraduate background. It is him who always support and encourage me throughout my Ph.D. study, even in my maternity period. He is such a person with great vision and desire to make the world better, which inspired me to work enthusiastically to science and engineering.

To the members of my Ph.D. committee: Profs. Alan W. Weimer, Charles B. Musgrave, J. Will Medlin, Steven M. George, and Aaron Saunders, I would like to thank each of you for the support you have shown throughout my academic process here through insightful discussions, challenging questions, and positive outlook. Special thanks go to Prof. Charles Musgrave for giving me the great help in the DFT theoretical work. He taught me the way of thinking, the method of writing and the ethic of Ph.D. research. His advice and support is priceless. I also like to thank Prof. Dave Clough, the Professor of my first class I took in the United States. He teaches so well and is humor and friendly, allowing me to own a great experience in the first period of studying here.

I owe many thanks to the present and former members in Team Weimer who helped me with experiments or discussions that were very valuable for my dissertation. Special thanks to Xinhua Liang and David M. King, who always gave me great suggestions and valuable

discussion along my whole Ph.D. study. A special thank is also deserved by Christopher Muhich. I really enjoy the corporation with him, and I feel so happy that I have the chance to work with him in the last year of my Ph.D. Eran N. Rozewski, the outstanding undergraduate student that I had the opportunity to work with in my graduate studies. I'd like to thank her for her hard work and commitment. Thanks are also due to Luis Hakim, Kathryn Barrett, Jianhua Li, Paul Lichty, Hans Funke, Brian Neltner, Casey Carney, Todd Francis, Chip Fisher, Troy Gould, Janna Martinek, Maria Saade Saade, Victoria Aston, Melinda Tucker, Bryan Woodruff, Alia Lubers, Aaron Palumbo and Kimberly Zimmer.

I wish to thank a long list of friends who have extended their love and support to me, such as Yue Cao, who helped me to understand the DFT better; such as Chunfang Ye, my best friend, who encourages me constantly, and all others who make my life in Boulder easier and happier.

My greatest gratitude goes to my parents. They are my permanent support despite the distance. I'd like to thank my parents-in-law, too. Without either parents' help for baby care, my work is impossible. Darren, my dear son, I don't know how to express my grate to you. I feel so sweet every moment when I think of you. I now know the happiest moment in my life is the time you first call "Mom".

The last and most grateful words are for Mingming Feng, my husband, the love of my life. I do not have appropriate words to thank him for his unconditional support, endless inspiration, and great love. This work is dedicated to him.

TABLE OF CONTENTS

LIST OF TABLES

LIST OF FIGURES

CHAPTER 1

Introduction and Background

1.1 TiO_2 Photocatalyst

1.1.1 TiO_2 photocatalyst for environmental application

Today, environmental pollution has become a serious problem. The organic pollutants in wastewater streams and volatile organic compounds in the atmosphere have continuously increased over the last decades. In order to address this significant problem, more and new approaches are required to reduce and eliminate these contaminants from the environment. Semiconductor photocatalytic degradation is a promising strategy to achieve this remediation goal.

Since the discovery of the photocatalytic property of the TiO_2 semiconductor in the 1970's, the scientific and engineering interest in the application of TiO_2 for environmental treatment has grown exponentially. There are many semiconductor materials, but, few are sufficiently robust photochemically and chemically to be described as a 'photocatalyst'. Most semiconductors, such as CdS, ZnO or WO, are either photochemically or chemically unstable. TiO_2 has proven to be the most suitable for widespread environmental applications [1-3].

The effect of TiO_2 photocatalyst for destruction of a wide range of organic compounds has been demonstrated by numerous reports [1-8]. These organic chemicals include various dyes [11], various substituted aromatics[4], volatile organic compounds in air [12], etc. A rather complete list of all photocatalytically degradable organic pollutants has been established by Blake [13], as the Table 1.1 shows.

Table 1.1 A list of photocatalytically degradable organic pollutants [9]

Class of organics	Examples
Alkanes	Isobutane, pentane, heptane, cyclohexane, paraffins
Haloalkanes	Mono-, di-, tri- and tetrachloromethane, tribromoethane, 1,1,1-trifluoro-2,2,2-trichloroethane
Aliphatic alcohols	Methanol, ethanol, propanol, glucose
Aliphatic carboxylic acids	Formic, ethanoic, propanoic, oxalic, butyric, malic acids, propene,
Alkenes	cyclohexene
Haloalkenes	1,2-dichloroethylene, 1,1,2-trichloroethylene
Aromatics	Benzene, naphthalene
Haloaromatics	Chlorobenzene, 1,2-dichlorobenzene
Nitrohaloaromatics	Dichloronitrobenzene
Phenolic compounds	Phenol, hydroquinone, catechol, methylcatechol, resorcinol, *o*- *m* -, *p*-cresol, nitrophenols
Halophenols	2-, 3-, 4-Chlorophenol, pentachlorophenol, 4-fluorophenol,
Amides	Benzamide
Aromatic carboxylic acids	Benzoic, 4-aminobenzoic, phthalic, salicylic, *m*- and
Acids	*p*-hydroxybenzoic, chlorohydroxybenzoic chlorobenzoic acids
Surfactants	Sodium dodecylsulfate, polyethylene glycol, sodium dodecyl benzene sulfonate, trimethyl phosphate, tetrabutylammmonium phosphate
Herbicides–pesticides	Atrazine, prometron, propetryne, bentazon, 2-4 D, monuron.... DDT, parathion, lindane,
Organo-phosphorus	tetrachlorvinphos, phenitrothion...
Dyes	Methylene blue, rhodamine B, methyl orange, fluorescein, Congo Red

Although there are some drawbacks for the environmental applications of TiO_2 photocatalyst, such as, UV light source required; slow complete degradation when oxidation degree is very low; photocatalytic engineering to be developed, etc., the advantages of TiO_2 are much greater than the disadvantages [2, 4, 14]:

1) the ability to degrade a broad range of pollutants;

2) low cost of titania;

3) safe, non-toxic;

4) no chemical additives required;

5) chemical stability of TiO_2 in aqueous media and in large range of pH ($0 \leq pH \leq 14$);

6) biological stability;

7) process at ambient temperature and pressure;

8) the possibility to work for systems containing very low pollutants concentrations;

9) absence of inhibition or low inhibition by ions generally present in water.

Due to such superior characteristics, semiconductor photocatalysts with a primary focus on TiO_2 are widely used for environmental applications. This method is believed to be a good supplementary and complementary method compared to conventional approaches for environmental treatment.

1.1.2 Mechanism of TiO_2 photocatalysis

The difference of photocatalysis from conventional catalysis is the mode of activation of the catalyst: thermal activation in conventional catalysis is replaced by a photonic activation in photocatalysis. The photonic activation process is due to the electronic structure of the semiconductor, which is characterized by a filled valence band and an empty conduction band. When a photon with an energy of *hv* matches or exceeds the band gap energy, E_g (3.2ev), of the TiO_2, which corresponds to wavelengths less than ~385nm, an electron is promoted from the valence band(VB) into the conduction band (CB) and, thus, leaves an electron deficiency or hole in the valence band. This is a rapid process occurring in femtoseconds. In this manner, electron/hole pairs are generated [2, 3, 11, 15-18].

The photoexcited electrons and holes can recombine, dissipating the input energy as heat if suitable electron and hole scavengers are absent; or diffuse to the surface, where they are trapped by TiO_2 surface defects or are transferred to adsorbed surface species [19]. If the electrons and holes become trapped, or react with electron donor and electron acceptor species adsorbed on the semiconductor surface, the recombination is prevented and subsequent reductive and oxidative processes may occur [3]. The general photoelectrochemical mechanism and

reaction steps for heterogeneous photocatalysis on TiO_2 proposed by Hoffmann et al [3] and Litter et al [16] are shown in Figure 1.1:

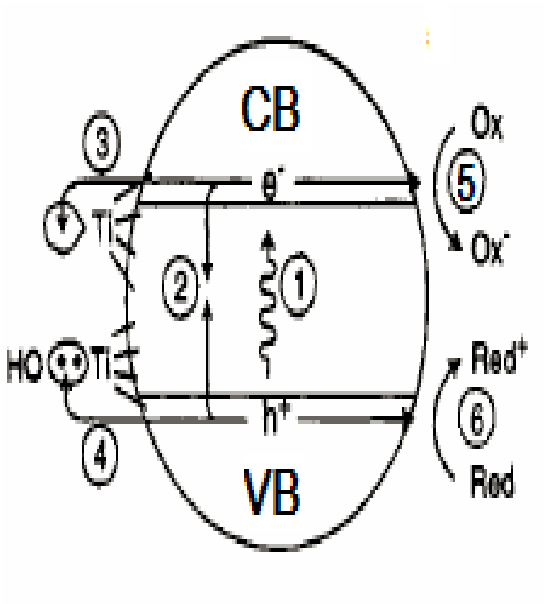

Charge-pair generation

$$TiO_2 + h\nu \longrightarrow e_{cb}^- + h_{vb}^+ \quad (1)$$

Recombination

$$e_{cb}^- + h_{vb}^+ \longrightarrow TiO_2 \quad (2)$$

Charge trapping

$$Ti^{4+} + e_{cb}^- \longrightarrow Ti^{3+} \quad (3)$$

$$>OH^- + h_{vb}^+ \longrightarrow Ti^{4+} + >OH^{\bullet} \quad (4)$$

Interface electron transfer

$$e_{cb}^-(Ti^{3+}) + Ox \longrightarrow Ox^- \quad (5)$$

$$h_{vb}^+(>OH^{\bullet}) + Red \longrightarrow Red^+ \quad (6)$$

Figure 1.1. Primary steps in the photoelectrochemical mechanism: (1) formation of charge by a photon; (2) charge carrier recombination to liberate heat;(3) trapping of a conduction-band electron in a dangling surficial bond to yield Ti(III); (4) trapping of a valence-band hole at surficial titanol group; (5) initiation of a reductive pathway by a conduction –band electron;(6) initiation of a oxidative pathway by a valence-band hole

where >TiOH represents the primary hydrated surface functionality of TiO_2, e_{cb}^- is a conduction band electron, h_{vb}^+ is a valence band hole, Red is an electron donor (e.g. reductant), and Ox is an electron acceptor (e.g. oxidant).

According to the mechanism illustrated above, the overall photocatalysis efficiency is determined by two critical factors: electron-hole recombination and interfacial electron transfer rate. An increase in either the recombination lifetime of charge carriers or the interfacial electron transfer rate constant is expected to result in higher TiO_2 photocatalytic performance[3]. Many factors may contribute to the different recombination lifetimes and interfacial electron-transfer rate constant, such as different crystal structures, surface morphologies, and surface doping [3].

The crystal structure of TiO_2 has an important effect on the photocatalysis performance. Titania exists as anatase, rutile and brookite crystalline forms. The latter is not common; it does not possess good photocatalytic properties and is rarely used as a photocatalyst. The anatase phase appears to be the most photoactive and, thus, it is the most practical for widespread environmental application [11, 20-23]. So the anatase was chosen as the crystal form for the theoretical study in this dissertation work.

Anatase is generated by the usual low temperature production method, such as alkaline hydrolysis of titanium(IV) compounds followed by calcination at moderate temperatures (400-500 ℃). The rutile phase is generally formed by sintering anatase at elevated temperatures (> 700 ℃) [24]. As a consequence, rutile usually has a much lower specific surface area (by a factor of 10 or more) than the anatase from which it was derived. Lower specific surface area of rutile contributes to the lower photoactivity than anatase. The second contributing factor is the dehydroxylation caused by the transformation from anatase, or by thermal treating. Dehydroxylation decreases photo-oxidations because it reduces the surface hydroxyls' hole trapping, and thereby enhancing the electron/hole recombination [16]. Moreover, Zhao et al suggest that the conduction band location of anatase is more favorable for driving conjugate reactions involving electrons, since the energy band-gaps of anatase and rutile are 3.23 and 3.02 ev, respectively [14]. This difference may also contribute to the higher photoactivity of anatase.

In recent years, Degussa P25 has set the standard for photoactivity in environmental applications. The TiO_2 P25 nanoparticles were used for the experimental study in this dissertation project. Degussa P25 is a nonporous 70:30 anatase-to-rutile mixture with a BET surface area of $50m^2/g$.

1.2 Thin film deposition

1.2.1 Atomic Layer Deposition

Atomic Layer deposition (ALD), originally named atomic layer epitaxy (ALE), is a vapor-phase deposition technique that was first invented by T. Suntola in the 1970's [25-27]. Initially, this method was used to produce thin film electroluminescent flat panel displays. With the down-scaling of semiconductor device dimensions, the ALD technique has received a lot of attention from the semiconductor industry in order to meet the demands of increasing processor speeds, shrinking line width and gate insulator thickness, as well as overall chip performance [28, 29]. ALD can deposit on a variety of surfaces in addition to flat substrates, such as ultrafine particles, porous structures, and extremely complex shapes. ALD can be used to deposit passivating films to prevent nanoparticles from oxidation while maintaining bulk properties[30]. It can be employed to modify surface optical or mechanical properties of particles[31, 32]. It also allows modification of interparticle forces between nanoparticles[33]. In addition, the ALD method employed for catalyst fabrication has increased quickly in recent years [34-37]. These applications of ALD result from its superior benefits including thickness control at the atomic scale, production of highly conformal and uniform films, and low temperature growth.

ALD is an analog of chemical vapor deposition (CVD). During a CVD reaction, the chemical reactants are fed simultaneously, which results in both surface and gas-phase reactions and no film thickness automatic control. So, the CVD films are generally relatively thick, non-conformal and highly granular. Instead, the ALD reaction splits the binary CVD reaction into two separate half-reactions by sequentially feeding precursors into the reactor. It consists of low-pressure feeding of individual reactive precursors to a substrate surface, until the surface saturation occurs. The reaction stops automatically when all of the surface reactive sites are

reacted, i.g. the surface saturation is achieved, even if the precursor continues to be fed into the reactor chamber [38-40]. One cycle of the ALD process comprisesfour steps: (1) the self-terminating first half reaction by exposure of precursor A, (2) purge or evacuation of the chamber using an inert gas such as N_2 or Ar to remove extra unreacted precursor A and gas by-product, (3) self-terminating second half reaction using precursor B, (4) purge or evacuation of the reaction to remove extra unreacted precursor B and gas by-product. By this ABAB sequential, self-limiting surface reaction process, ALD is used to deposit materials in an atomic layer-by-layer fashion. The self-limiting nature leads to excellent step coverage and conformal deposition. The produced films remain extremely conformal to the original substrate with angstrom-level thickness control [39, 41].

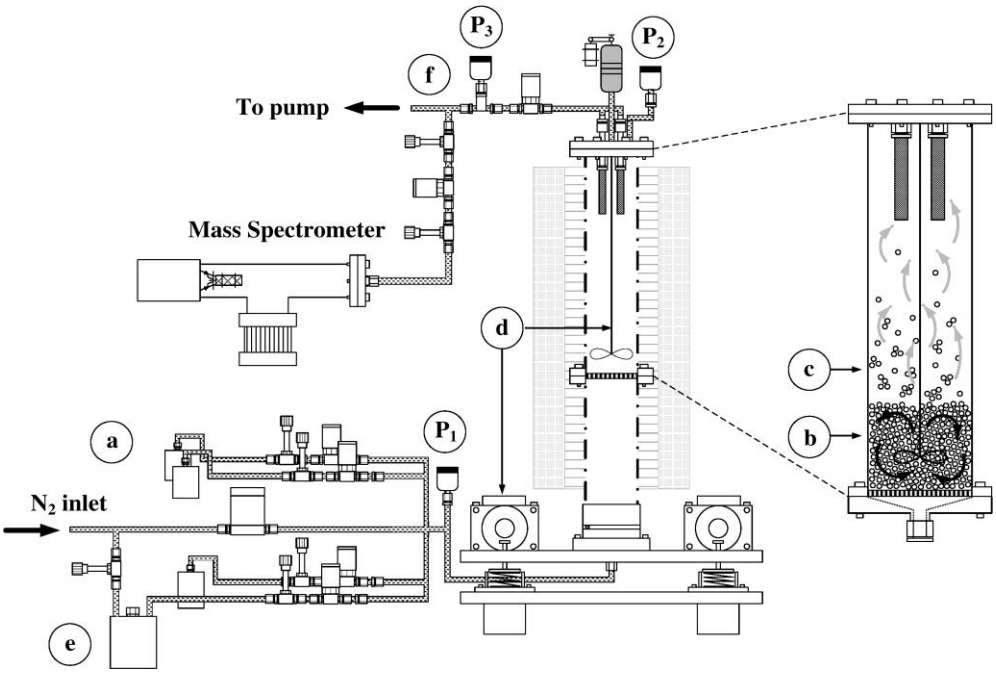

Figure. 1.2 Schematic of the fluidized bed reactor configuration with in situ mass spectrometry for particle ALD [9].

Due to the superior characteristics, ALD applied on particles has been of more and more recent interest. The ALD on particles can be carried out in a fluidized bed reactor. As shown in the Figure 1.2, the fluidized bed reactor is comprised of several operations including feeding, reaction, and outgas. (a) is the dosing zone which allows for the controlled delivery of a variety of precursors. (b) is the particle bed where substrate particles are fluidized using either the inert purge gas or the reactive precursor itself. During fluidization, the upward force pressure drop across the fluidized bed equals the downward force of the particle mass, which leads to the fluidization of the particles. The particles entering the splash zone (c) fluidize as soft agglomerates, and the operating velocities are controlled to minimize particle elutriation to the top filters. A bottom filter exists on the bottom of the fluidized bed reactor too to allow only gas and precursors enter the reactor. Mechanical bed agitation (d) is used to facilitate fluidization. The precursor bubblers (e) contain the precursors and the precursor feeding can also help to maintain fluidization during dosing. Real-time gas sampling occurs at the outlet of the reactor (f) using in situ mass spectrometry. With the mass spectrometry, the reaction can be monitored and controlled in situ, which allows the ALD reaction to be well studied and the precursor efficiently used because the reaction can be stopped as soon as the reaction is completed, i.e. so minimal/no precursor wastes. Three capacitance manometers (P1, P2, P3) are employed to monitor fluidization and proper system operation. The pressure information is very useful for trouble shooting if there is any blockage or leakage issues with the system. In order to prevent gas precursors from condensing before entering the reactor, all the feeding lines are surrounded by heating tapes to maintain higher temperatures [9, 31, 42, 43].

1.2.2 TiO_2 ALD

Since TiO_2 is a good photocatalyst, applying TiO_2 thin films as self-cleaning material for environmental treatment has been widely reported. There are many methods to produce TiO_2 thin films, such as sol-gel, electrodeposition, chemical vapor deposition and physical vapor deposition [8], while ALD should be the best technique to deposit uniform and pinhole-free TiO_2 films on nanoparticles. TiO_2 ALD has been well-studied, and has been deposited by means of many different precursors [44-46]. $TiCl_4$ and H_2O_2 were selected as precursors in this study as they have been proven to be favorable for TiO_2 ALD [44, 47, 48]. $TiCl_4$ molecules tend to have a higher reactive surface site concentration due to the low steric hindrance offered by its single-atom ligands. Other organometallic titanium-containing precursors, such as titanium tetraisopropoxide and titanium tetraethoxide typically grow at a lower stochastic rate of the chloride analog. Though $TiCl_4$-based TiO_2 ALD processes typically result in a higher growth rate, the trade-off is the corrosive nature of the precursor and HCl byproducts. Special caution is required to protect the pump from corrosives due to the acid HCl byproduct. In our process, three $NaHCO_3$ traps were positioned before the pump to remove HCl, and the $NaHCO_3$ micro-powders were replaced frequently. With concentrated H_2O_2 (50% in H_2O) as the oxidation agent, instead of H_2O, higher TiO_2 growth rates and lower chlorine contents have been attained at lower deposition temperatures, due to the stronger oxidation potential of the peroxide [47]. This ALD reaction is based on the binary CVD reaction:

$$TiCl_4 + H_2O_2 \rightarrow TiO_2 + 2HCl + Cl_2 \tag{1.1}$$

This reaction divided into the following two surface reactions, where the asterisks denote the surface species:

$$A: Ti(OH)_2{*} + TiCl_4 \rightarrow TiO_2TiCl_2{*} + 2HCl \tag{1.2}$$

$$B: TiCl_2 * + H_2O_2 \rightarrow Ti(OH)_2 * + Cl_2 \tag{1.3}$$

In an ABAB reaction sequence, the TiO_2 film can be deposited with atomic-level control. This set of sequential surface reactions has been studied extensively by means of mass spectrometry and other *in situ* techniques and it has been shown that the individual half-reactions are self-limiting [47, 48].

1.2.3 AlN ALD

Besides oxide ALD, nitride ALD was well developed too. Nitrides have been grown for the elements in group 4-6 and 13,14 [40]. Though nitride films have many special properties, their passivation function is a most important characteristic, resulting in such applications for the nitride films of AlN, TiN and Hf_3N_4 [49-51]. Aluminum nitride (AlN) is deposited on particle surfaces with ALD in this study to function as a diffusion barrier for protecting core particles from oxidation. Trimethylaluminium (TMA) and ammonia (NH_3) were chosen as precursors for AlN ALD. These are the simplest forms of an alkyl aluminum metalorganic and a nitrogen-containing precursor available. Their suitability for the production of both bulk and thin film AlN structures is well known[52, 53].

AlN ALD growth is based on the following CVD reaction: [53, 54]

$$Al(CH_3)_3 + NH_3 \rightarrow AlN + 3CH_4 \tag{1.4}$$

Similar to TiO_2 ALD, the binary reaction in Equation (1.4) can be divided into two half-reactions for AlN ALD as follows: [55]

$$A: AlNH_2 * + Al(CH_3)_3 \rightarrow AlNAlCH_3 * + 2CH_4 \tag{1.5}$$

$$B: AlCH_3 * + NH_3 \rightarrow AlNH_2 * + CH_4 \tag{1.6}$$

The ALD of AlN can be performed at a temperature as low as 250 ℃, which is one of the lowest temperatures for which nitride layers have been deposited using ALD [40].

1.3 Pt nanoparticle deposition

1.3.1 Introduction

Although TiO_2 photocatalyst is extensively used for many environmental applications, the treatment efficiency is still not high enough for it to be used at large scale. First, the quantum efficiency of TiO_2 is low. Serpone et al reported that about 90% of the photogenerated electron-hole pairs recombined rapidly within or at the surface of TiO_2 particles [56]. Second, the solar energy adsorption of TiO_2 is low. The best photoactivity of TiO_2 is only under ultraviolet irradiation with light wavelength lying between 300 and 400 nm which represents ~ 3% of the solar spectrum [57]. Therefore, the improvement of the TiO_2 photoactivity has emerged as a research subject of considerable importance and urgency.

Surface modification of TiO_2 is a good method to improve TiO_2 photocatalytic performance. Nobel metals or transition metal oxides have received considerable attention to be the deposited metal [12, 16, 58, 59]. In particular, many papers have reported that the phototocatalytic oxidation was enhanced dramatically by Pt deposition. Sano et al observed that the photocatalytic degradation rate of toluene and acetaldehyde increased significantly with Pt doping [60]. Lee et al compared different doped titanias, such as Pd/TiO_2, Ru/TiO_2, Ag/TiO_2, and Pt/TiO_2 on the photocatalytic degradation of volatile organic compounds, and indicated that Pt/TiO_2 provided for the best improvement effect [61]. Sivalingam et al showed that the photoactivity on methylene blue varies in the order Pt/TiO_2 >Mn/TiO_2 >Cu/TiO_2 [11]. Cho et al also reported that Pt is the most active metal to enhance the photocatalytic oxidation of O_3 [62].

Therefore, the overall study of the Pt modification for TiO_2 photocatalyst is the focus of this study.

1.3.2 Traditional Pt deposition methods

Many factors influence the modification effect of Pt deposits on the photoactivity of TiO_2; and the Pt deposition method is one of the most important factors. Many traditional methods to deposit Pt clusters on TiO_2 have been reported, as summarized below.

(1) Photo-deposition

The most common method to deposit Pt onto TiO_2 and other semiconductor photocatalysts, is photo-deposition[24]:

$$Pt^{n+} + SED \xrightarrow{semiconductor, hv} Pt \downarrow + products \qquad (1.7)$$

where Pt^{n+} is the Platinum salt (such as H_2PtCl_6) and the SED is a sacrificial electron donor, which can be almost any easily and irreversibly oxidized organic solvent, or dissolved species (such as EDTA or cysteine), even water; for Pt photo-deposition, however, methanol or ethanol is preferred [24]. This method was first reported by Krecutler and Bard [63] in 1978.

The key mechanism of the Pt photo depositionis related to the photoreaction induced by the semiconductor material. Under ultra-bandgap irradiation, electron-hole pairs are generated in the semiconductor particles and migrate to the particle surface, where the photo-generated holes oxidize water or organics and the photo-generated electron reduces Pt salt to its zero valence metal form. In this manner, the Pt metal is deposited on the surface of the semiconductor particles [24].

The experimental procedure of photo-deposition involves suspending TiO_2 particles in a solution containing H_2PtCl_6 and acetic acid. After adjusting PH, the catalyst-containing solution

is purged with nitrogen in order to produce an anaerobic environment since O_2 interferes with the Pt salt reduction; and is then illuminated with a Xe-Hg lamp [1, 64-67]. The Pt loading amount can be controlled by the concentration of Pt salt, H_2PtCl_6. Different pH values and different concentrations of acetic acid during the deposition process can result in different platinum deposit forms. Generally, an increase in pH leads to the deposition having a higher platinum oxidation state, but increases in acetic acid concentration has the reverse effect [68].

(2) Impregnation

Impregnation is an early, now classic, approach to deposit Pt on TiO_2 surfaces. This method is to impregnate the semiconductor particles with a Pt salt (such as H_2PtCl_6) followed by reduction in a stream of H_2 at high temperature (~480 ℃) [4, 24, 57].

(3) Chemical reduction of Pt salt

Another deposition method involves the chemical reduction of a Pt salt at room temperature in the presence of semiconductor particles. The reducing agent is usually sodium borohydride but, more recently, zinc powder has been used [24].

(4) Colloid coagulation method

This method was developed by Gratzel et al in 1981 [69]. In this method, a Pt-citrate colloid is prepared, followed by removal of the protective citrate by coagulating the colloid using an ion-exchange resin, in the presence of the semiconductor powders, and then sonication of the resulting mixture [24, 70]. However, some problems are easily encountered using this procedure, such as Pt adhering to the resin and incomplete precipitation of the non-protected Pt sol onto the semiconductor powder [70].

(5) Vapor deposition

Vapor deposition is also used by some authors. For example, Hiehata et al have deposited Pt metal on TiO_2 surface by exposure of TiO_2 powders to the Pt vapor followed by subsequent annealing [71].

1.3.3 Pt metal Atomic Layer Deposition (ALD)

As discussed above, the Pt can be deposited on semiconductor particles by various methods. Different procedures of the deposition method will affect the Pt modification effect to the photoactivity. For example, acid is used for photo-deposition and some other methods, where slight acidic etching would change the surface of TiO_2 and then photoactivity. During the impregnation method, annealing is required. Varying the annealing temperature would change the TiO_2 crystal structure and, therefore, the TiO_2 photoactive property. More importantly, different deposition methods provide different control abilities for the Pt deposit size and dispersion. These provide for different catalytic performance as well. Many researchers have agreed that the homogeneous distribution of smaller Pt deposits on the surface of TiO_2 would supply better photocatalysis performance [61, 64]. However, the traditional methods cannot accurately control the Pt deposition, especially when it is desirable to uniformly modify surfaces with small, highly dispersed Pt islands or nanoparticles.

The ALD method was demonstrated in this study to be a good alternative to overcome the drawbacks of the traditional methods. This study is the first attempt by using an ALD method to deposit Pt on TiO_2 for the purpose of increasing photoactivity of TiO_2. As mentioned above, ALD is a thin film growth technology that allows for excellent conformal and uniform growth with precision control over both thickness and composition. This technology uses sequential self-limiting surface reaction steps to deposit materials in an atomic layer-by-layer fashion [32, 33,

41]. It is known that during the early stages of ALD growth, the nucleation of precursors on surface sites can be based on the Volmer-Weber growth mechanism. Five microstructural stages are included in the Volmer-Weber growth mode: nucleation of discrete islands, island growth, island impingement and coalescence, percolation of the island array, and channel filling to eventually form a continuous thin film[72]. In this manner, the ALD technique cannot only deposit films but also islands when only early stages of ALD growth are applied. Moreover, different deposition temperatures will lead to different island densities. Therefore, the loading and dispersion of Pt can be controlled by varying the number of ALD cycles and the deposition temperature. These powerful characteristics make ALD an attractive technology to produce both high-quality films and nanoparticles on the surfaces of flat or particulate substrates.

Pt deposition via ALD has received significant recent attention [34, 35, 41, 73]. King et al. revealed that the Pt islands deposited on catalyst substrates using the ALD method were highly dispersed and exhibited high catalytic activity [41]. Liu et al. compared different deposition methods and concluded that ALD could overcome the difficulties associated with traditional methods and grow a uniform array of size-controllable Pt nanoclusters [74]. Hoover et al. demonstrated that Pt ALD started with the formation of islands several atoms high before a complete thin film was produced [35]. Each of these reports suggested that ALD may be an ideal strategy to deposit islands of Pt on TiO_2 substrates to improve its photocatalytic activity.

In this study, Pt was deposited on TiO_2 via the ALD technique using alternating exposures of Methylcyclopentadienyl-(trimethyl) Platinum(IV) ($MeCpPtMe_3$) and oxygen. This method was first reported by Aaltonen et al. in 2003[75]. A linear growth rate was demonstrated and the self –limiting reaction mechanism was proposed by Aaltonen [75, 76]:

$$CH_3C_5H_4Pt(CH_3)_3 + Pt - O_x \rightarrow Pt(s) + CO_2(g) + H_2O(g) + otherbyproducts \quad (1.8)$$

$$Pt(s) + O_2 \rightarrow Pt - O_x \quad (1.9)$$

After that, the reaction mechanism of Pt ALD was further studied and Kessels et al proposed a more complete one with quantitative information [77]:

$$2CH_3C_5H_4Pt(CH_3)_3(g) + 3O(ads) \rightarrow 2CH_3C_5H_4Pt(CH_3)_2(ads) + CH_4 + CO_2(g) + H_2O(g) \quad (1.10)$$

$$2CH_3C_5H_4Pt(CH_3)_2(ads) + 24O_2(g) \rightarrow 2Pt(s) + 3O(ads) + 16CO_2(g) + 13H_2O(g) \quad (1.11)$$

1.4 *Ab initio* calculation of Pt / TiO_2 system

1.4.1 Density Functional Theory

Density functional theory (DFT) is one of the most widely used quantum mechanical calculation methods and has been proven to correctly provide a fundamental understanding for a wide variety of phenomena, especially in physics and chemistry [10, 78-84]. It investigates the electronic ground state structure of many body systems. The basis of quantum simulation is the Schrödinger Equation, which for a single electron moving in an external potential ν(r) reads:

$$\left[-\frac{\hbar^2\nabla^2}{2m} + \upsilon(r)\right]\Psi(r) = \varepsilon\Psi(r) \quad (1.12)$$

The wave function, Ψ, contains all the information about the given system. For many-electron systems, however, the Schrödinger Equation, with the wave function Ψ (r_1, r_2, … r_N), is impossible to be solved in its complete many-body form. DFT recasts this problem in terms of the electronic density distribution and makes the extremely complex N-body problem into computational solvable N 1-body problems. The local density of electrons is

$$n(r) = |\psi(r)|^2 \quad (1.13)$$

DFT was put up by Hohenberg and Kohn (1964) and further developed through the approximation methods by Kohn and Sham (1965). The conceptual root of DFT is the Hohenberg-Kohn(HK) Theorem. This theorem states that for a system of N interacting electrons, the non-degenerate ground state wave function is uniquely determined from ground state density:

$$\Psi_0(r_1, r_2 ..., r_N) = \Psi[n_0(r)] \tag{1.14}$$

As a consequence, the dependence on the wave function can be replaced by a dependence on the electron density distribution n(r). This is the essence of the HK theorem. In this way, the total energy can be expressed as:

$$E_v[n] = T[n] + V[n] + U[n] \tag{1.15}$$

where T[n] is the energy contribution from the kinetic energy of the electrons:

$$T[n] = -\frac{\hbar}{2m}\sum_i \int \psi_i \nabla^2 \psi_i d^3 r \tag{1.16}$$

and V[n] is the potential energy field caused by electron-ion interactions:

$$V[n] = \int d^3 r n(r) v(r) \tag{1.17}$$

Once the system is specified, i.e. the positions of the ions are fixed (and hence ν(r) is fixed), V[n] becomes simple to calculate since it only depends on the distribution of the electrons n(r).

U(n) calculates the energy contribution from electron-electron interactions and is composed of two terms:

$$U[n] = \frac{e^2}{2}\int \frac{1}{r_{12}} n_1 n_2 d^3 r_1 d^3 r_2 + E_{xc}[n] \tag{1.18}$$

The first term is the Coulombic electron-electron repulsion energy and the second term is the electron exchange-correlation energy.

The above equations are called the Kohn-Sham (KS) equations. And the Schrödinger Equation can be expressed by the KS equation:

$$\left[\frac{-\hbar^2}{2m}\nabla^2 + V_{ion}(r) + V_H(r) + V_{xc}(r)\right]\psi_i(r) = \varepsilon_i \psi_i(r) \tag{1.19}$$

KS approach makes DFT practical by introducing sufficiently accurate approximations to E_{xc} and then solving appropriate single electron problems. Only the minimum value of the KS energy function has physical meaning, representing the ground state of the system. There are several approximations people carry out to express the above total energy as a function of local electron density. Now we discuss this for each of the terms.

As we will show later in this section, the electron kinetic energy can be expressed as an exact form of electron density. So no approximation is needed for this term.

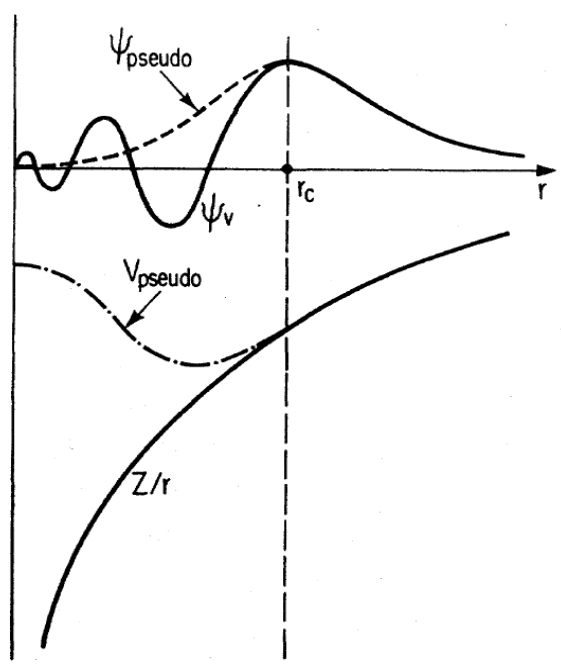

Figure. 1.3 Schematic illustration of all-electron (solid lines) and pseudoelectron (dashed lines) potentials and their corresponding wave functions. The radius at which all-electron and pseudoelectron values match is designated r_c [10].

For the term of ion-electron interaction, pseudopotential approximation was applied to make the calculation tractable. In the realistic solid, the wave function oscillates drastically within a few angstroms near the atomic core (see Figure 1.3), resulting in significant difficulty to calculation. However, what is relevant to the physical properties is the wave function in longer distance, having a "most probable location of electron" (the peak in the tail of the wave functions) and the long-range decay of the wave function tail. Pseudopotential approximation removes the core electrons and replaces the core electrons and strong ionic potential by a weaker pseudopotential. As shown in Figure 1.3, a set of smooth pseudo wave functions substitute the true oscillating wave functions near the core region. And the longer distance behavior of the wave function with the pseudopotential matches the actual potential. So, the pseudopotential is finite near the atomic core. This will make the calculation much more efficient and save a significant amount of time.

For the last term in the total energy KS equation, electron-electron interaction U includes the Coulomb repulsion, which can be expressed exactly as a product of electron density. Since electron density does not explicitly include electron correlation or exchange, U is corrected by this additional term, E_{xc}, which includes the complex electron-electron interaction information that is not included in non-interacting systems. This is the most difficult part in the DFT as no exact function is known. Without a practical approximation of E_{xc}, DFT would be of very little interest or use. The simplest method of describing the exchange-correlation energy of an electronic system is the local-density approximation (LDA, Kohn and Sham 1965):

$$E_{xc}^{LDA}[n] = \int n\varepsilon_{xc}^{\text{hom}}(n)dr \qquad (1.20)$$

where $\varepsilon_{xc}^{\text{hom}}$ is the exchange-correlation energy per electron in a homogeneous electron gas of density n. LDA assumes that the exchange-correlation energy functional is purely local, ignoring

the nearby inhomogeneity in the electron density.

Up to now we can solve the KS equation in principle. In practice, one difficulty remains to be treated: to capture the density in the real solid, it is essential to sample many points in real space and over many unit cells. This significantly increases the cost of calculation. To solve this problem, we resort to the Fourier transform of real space, i.e. the reciprocal lattice and use Bloch's theorem.

The real space periodicity is reflected in its Fourier transform. The existence of energy dependence on electron motion, i.e. the dispersion, suggests that it might be possible and reasonable to solve this iterative equation in the reciprocal space. As will be clear from the following discussion, this allows the corresponding energy matrix to be sparse, thus increasing the speed and reducing the complexity of the calculation. The Fourier transform changes the problem of calculating an infinite number of electron orbitals for an infinite number of points in real space to one of calculating a finite number of electron orbitals at an infinite number of k points. However, most of the k points are either decoupled or weakly coupled. For the specific k point that we are interested in we only need to consider a few numbers of orbitals.

Bloch's theorem is essential for the choice of the boundary condition. For solid state calculation, the periodic boundary condition method was used so that only a few unit cells (called a super cell) are required as input to simulate an infinite lattice. It requires the wave function (thus the density) to repeat itself as a period of the super cell. It would not be a good idea to choose a small super cell since the charge density modulation in many cases have a periodicity larger than a single unit cell. Bloch's theorem states that in a periodic solid each electronic wave function differs only by a phase factor $\exp(i\boldsymbol{k}\boldsymbol{R})$ between equivalent positions in the lattice.

$$\Psi_0(r+R) = \exp(ik \bullet R)\Psi(r) \tag{1.21}$$

where k is the momentum of the electron and $\Psi(r+R) = \Psi(r)$. The prefactor exp(ikR) takes the form of a plane wave. Actually in the DFT calculation, the plane wave function is a commonly chosen basis for expanding the wave function and the density.

Now we rewrite the KS equation (1. 19) term by term into the reciprocal space:

$$\sum_{G'}\left[\frac{\hbar^2}{2m}|k+G|^2\delta_{GG'} + V_{ion}(G-G') + V_H(G-G') + V_{xc}(G-G')\right]c_{i,k+G'} = \varepsilon_i c_{i,k+G} \tag{1.22}$$

where G is the reciprocal lattice vector. Note the kinetic energy term is rewritten in a more compact way in the reciprocal space than in the real space. The KS equation can be solved self-consistently, as shown in the procedure given in the flow chart (DFT self-consistent field (SCF)) (Figure 1.4). We guess an initial density, and construct V_{xc} with the guess density. New orbitals are determined from solution of the secular equations, the density is determined from those orbitals, and it is compared to the density from the preceding iteration. Once convergence of the SCF is achieved, the energy is computed by plugging the final density into the original energy equation.

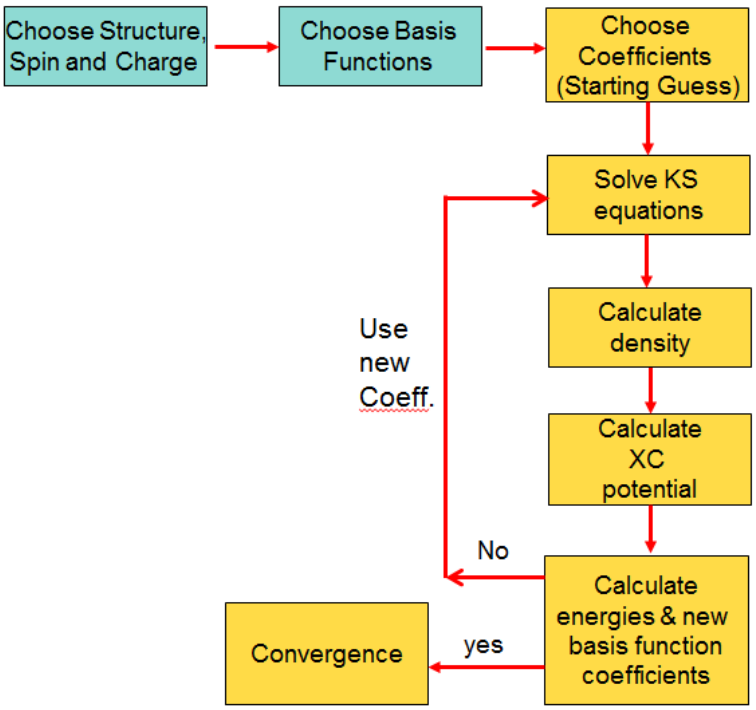

Figure 1.4. Flow chart describing the SCF calculation of KS equations.

Last we address briefly the limitation of the DFT method. While the electron density describes the ground state sufficiently, it does not give a good approximation of the excited state. Such properties as the excitation energy and band gap can be severely underestimated. Secondly, DFT calculation does not work well for materials with unfilled d or f orbitals. The bonding between next atoms is highly anisotropic due to the spatial localization of the d or f orbitals, and for the same reason the correlation between electrons is strong. The LDA approximation of the exchange-correlation term is not sufficient so more sophisticated techniques are required. This is one of the frontiers of the DFT calculation and for our purpose we will not need these further approximations.

1.4.2 Literature review of DFT study of Pt/TiO_2

In the last decade, DFT has become a more and more important tool to study complicated systems in chemistry, especially in catalysis areas. The DFT study of catalysts can provide important insights into the properties and behavior of real catalysts.

As the most important photocatalyst, quantum mechanical calculations of TiO_2 play an important role to explain the photocatalysis at the molecular level. Initially, the majority of this study deals with rutile surface, because it is the most thermally stable TiO_2 crystal phase [85-87]. For example, Shapovalow et al theoretically studied the nature of excited states of rutile TiO_2 (110) surface with adsorbed water [86]. Shu et al calculated the O_2 adsorption behavior on the rutile TiO_2 (110) surface [85]. Whereas, it is anatase which has the higher photoactivity than rutile and more widely used in catalysis and photoelectronchemistry, thus the DFT calculation of anatase structure and its photoactivity study become popular later [88-91]. For example, Belelli et al theoretically studied the H_2O dissociative adsorption and the O_2 adsorption on a photoactivated TiO_2 (0 0 1) anatase surface and they suggested that the OH· and the $O_2^{\cdot -}$ species would work as active species in a photocatalytic process [89], Aschauer et al studied the peroxide and superoxide states of adsorbed dioxide on anatase TiO_2 (101) with subsurface defects and found that O_2 adsorption is strongly enhanced at sites close to the subsurface defect [88].

Recent advances in heterogeneous photocatalysis have produced a number of interesting surface phenomena and various novel photocatalysts with improved properties compared to the standard TiO_2 photocatalyst. As discussed in section 1.3, doping Pt nanoparticles to improve the photoactivity of TiO_2 attracted significant interesting in research and industry due to its great improvement effect. Several theoretical studies involved this important topic and investigated the Pt cluster interaction with the TiO_2 surface [92, 93]. Han et al illuminated small Pt cluster

structure and electronic property on perfect anantase TiO_2 (101) surfaces and suggested the Pt cluster prefer 3D growth [93]. Gong et al calculated small Pt clusters on regular and defect sites of anatase TiO_2 (101) surfaces and indicated that steps and O-vacancies may act as nucleation sites for Pt growth [92]. However, both only calculated small Pt clusters with 1 to 3 Pt atoms; moreover, no theoretical work on the Pt role to the photoactivity of TiO_2 was reported as far as we know.

As one of the most important heterogeneous catalyst, understanding the Pt diffusion and ripening mechanism is critical for better application. Theoretical studies have been reported on the Pt diffusion behavior on different support surfaces [94, 95], such as, Deskins et al studied a single Pt atom adsorption and diffusion on γ-Al_2O_3 surfaces and indicated that the Pt sintering process is hindered at low temperature [94]; Bruix et al investigated the diffusion of Pt atoms on CeO_2 surface by periodic density functional calculations and found the energy cost required for the diffusion of Pt atoms is very slow [95]. However, no theoretical study related to Pt growth and migration on TiO_2 surfaces has been reported yet.

1.5 Statement of Purpose

Environmental pollution is a serious problem in today's fast growing society. The amount of organic pollutants in wastewater and volatile organic compounds in air has continuously increased over the last few decades. Since the discovery of the photocatalytic behavior of the TiO_2 semiconductor in the 1970's, the scientific and engineering interests in the application of TiO_2 for environmental treatment have grown exponentially. As a durable photocatalyst, TiO_2 is highly photoactive, chemically stable, low cost and non-toxic. These make

TiO_2 very popular for environmental treatment applications, such as wastewater remediation and air purification.

However, there are some limits of TiO_2 usage for environment treatment, such as, the difficult recovery of the TiO_2 nanopowders and the relatively low photocatalytic efficiency. This dissertation addresses these problems by creating modified TiO_2 photocatalyst using the ALD method. First, the nano- magnetic photocatalyst is synthesized by depositing TiO_2 films on magnetic core particles using the TiO_2 ALD method. Combining the magnetic property of the iron core with the photoactivity of the TiO_2 films, this novel material is believed to be an efficient, cost-effective and environmentally-friendly means for environmental remediation. Secondly, the TiO_2 photocatalyst is modified by Pt deposition using the ALD method. As we know, the method of Pt deposition is important as it impacts the catalytic efficiency. The ALD method is superior because it can deposit small metal particles with high level of dispersion. The ALD deposited Pt particles was found to significantly improve the photoactivity of TiO_2 and, thus, lead to high pollutants treatment performance.

Although by doping Pt nanoparticles on TiO_2 to increase the photoactivity of TiO_2 is a widely accepted method, the real role of Pt deposition on TiO_2 is incompletely understood. DFT simulation was applied in this dissertation to study the growth and migration mechanism of Pt nanoparticles on TiO_2 surface and the role of the Pt doping to the photoactivity of TiO_2. The theoretical study provides fundamental understanding to the real catalyst behavior with less complexity than experimental methods. The thoroughly understanding of the Pt growth and ripening behaviors during the early stage of ALD is significant for the Pt/TiO_2 application as a heterogeneous catalyst and also provide insights for other studies related with transition metal ALD growth and heterogeneous catalysis. The discovery of the real role of the Pt doping on the

photoactivity of TiO_2 clarifies several long-held assumptions about this process. It contributes a significant advance to this important application field, as a direct guide to maximize photocatalytic performance at an optimum situation.

1.6 References

1. Falconer, J.L.a.M.-B., KA, Photocatalytic and thermal catalytic oxidation of acetaldehyde on Pt/TiO2. Journal of Catalysis, 1998. 179: p. 171-178.

2. Herrmann, J.M., Heterogeneous photocatalysis: State of the art and present applications. Topics in Catalysis, 2005. 34(1-4): p. 49-65.

3. Hoffmann, M.R., et al., Environmental Applications of Semiconductor Photocatalysis. Chemical Reviews, 1995. 95(1): p. 69-96.

4. Herrmann, J.M., Heterogenous photocatalysis: an emerging technology for water treatment. Catalysis Today, 1993. 17: p. 7-20.

5. Herrmann, J.M., From catalysis by metals to bifunctional photocatalysis. Topics in Catalysis, 2006. 39(1-2): p. 3-10.

6. Pirkanniemi, K. and M. Sillanpaa, Heterogeneous water phase catalysis as an environmental application: a review. Chemosphere, 2002. 48(10): p. 1047-1060.

7. Zhong, H., Y. Yang, and C.X. Tian, Photocatalytic mechanisms of modified titania under visible light. Research on Chemical Intermediates, 2011. 37(1): p. 91-102.

8. Chen, X. and S.S. Mao, Titanium dioxide nanomaterials: Synthesis, properties, modifications, and applications. Chemical Reviews, 2007. 107(7): p. 2891-2959.

9. Weimer, A.W., et al., Atomic layer deposition on particles using a fluidized bed reactor with in situ mass spectrometry. Surface & Coatings Technology, 2007. 201(22-23): p. 9163-9171.

10. Payne, M.C., et al., Iterative Minimization Techniques for Abinitio Total-Energy Calculations - Molecular-Dynamics and Conjugate Gradients. Reviews of Modern Physics, 1992. 64(4): p. 1045-1097.

11. Sivalingam, G., et al., Photocatalytic degradation of various dyes by combustion synthesized nano anatase TiO2. Applied Catalysis B-Environmental, 2003. 45(1): p. 23-38.

12. Sano, T., et al., Effect of Pd-photodeposition over TiO2 on product selectivity in photocatalytic degradation of vinyl chloride monomer. Journal of Molecular Catalysis a-Chemical, 2002. 189(2): p. 263-270.

13. Blake, D., ed. Bibliography of work on photocatalytic removal of hazardous compounds from water and air 1999, national renewable energy laboratory.

14. Zhao, W., et al., Photodegradation of sulforhodamine-B dye in platinized titania dispersions under visible light irradiation: Influence of platinum as a functional co-catalyst. Journal of Physical Chemistry B, 2002. 106(19): p. 5022-5028.

15. Pore, V., et al., Atomic layer deposition of TiO2-xNx thin films for photocatalytic applications. Journal of Photochemistry and Photobiology a-Chemistry, 2006. 177(1): p. 68-75.

16. Litter, M.I. and J.A. Navio, Photocatalytic properties of iron-doped titania semiconductors. Journal of Photochemistry and Photobiology a-Chemistry, 1996. 98(3): p. 171-181.

17. Augugliaro, V., Litter,M., ect, The combination of heterogeneous photocatalysis with chemical and physical operations: A tool for improving the photoprocess performance. Journal of Photochemistry and Photobiology C: photochemistry reviews, 2006. 7: p. 127-144.

18. Hashimoto, K., H. Irie, and A. Fujishima, TiO2 photocatalysis: A historical overview and future prospects. Japanese Journal of Applied Physics Part 1-Regular Papers Brief Communications & Review Papers, 2005. 44(12): p. 8269-8285.

19. Kennedy, J.a.D., AK, Photothermal heterogeneous oxidation of ethanol over Pt/TiO2. Journal of Catalysis, 1998. 179: p. 375-389.

20. Inagaki, M., et al., Dependence of photocatalytic activity of anatase powders on their crystallinity. Chemosphere, 2006. 64(3): p. 437-445.

21. Inagaki, M., et al., Photocatalytic activity of anatase powders for oxidation of methylene blue in water and diluted NO gas. Applied Catalysis B-Environmental, 2004. 51(4): p. 247-254.

22. Inagaki, M., et al., Preparation of stable anatase-type TiO2 and its photocatalytic performance. International Journal of Inorganic Materials, 2001. 3(7): p. 809-811.

23. Toyoda, M., et al., Effect of crystallinity of anatase on photoactivity for methyleneblue decomposition in water. Applied Catalysis B-Environmental, 2004. 49(4): p. 227-232.

24. Mills, A.a.L., SK, Platinum group metals and their oxides in semiconductor photosensitisation. Platinum metals review, 2003. 47(1): p. 2-12.

25. Suntola, T., Atomic Layer Epitaxy. Acta Polytechnica Scandinavica-Electrical Engineering Series, 1989(64): p. 242-270.

26. Suntola, T., Atomic Layer Epitaxy. Thin Solid Films, 1992. 216(1): p. 84-89.

27. Suntola, T. and J. Hyvarinen, Atomic Layer Epitaxy. Annual Review of Materials Science, 1985. 15: p. 177-195.

28. Kim, H., H.B.R. Lee, and W.J. Maeng, Applications of atomic layer deposition to nanofabrication and emerging nanodevices. Thin Solid Films, 2009. 517(8): p. 2563-2580.

29. Niinisto, L., et al., Advanced electronic and optoelectronic materials by Atomic Layer Deposition: An overview with special emphasis on recent progress in processing of high-k dielectrics and other oxide materials. Physica Status Solidi a-Applied Research, 2004. 201(7): p. 1443-1452.

30. Hakim, L.F., et al., Synthesis of oxidation-resistant metal nanoparticles via atomic layer deposition. Nanotechnology, 2007. 18(34): p. -.

31. King, D.M., et al., Atomic layer deposition of UV-absorbing ZnO films on SiO(2) and TiO(2) nanoparticles using a fluidized bed reactor. Advanced Functional Materials, 2008. 18(4): p. 607-615.

32. Hakim, L.F., et al., Nanoparticle coating for advanced optical, mechanical and rheological properties. Advanced Functional Materials, 2007. 17(16): p. 3175-3181.

33. Liang, X.H., S.M. George, and A.W. Weimer, Synthesis of a novel porous Polymer/Ceramic composite material by low-temperature atomic layer deposition. Chemistry of Materials, 2007. 19(22): p. 5388-5394.

34. Christensen, S.T., et al., Nanoscale Structure and Morphology of Atomic Layer Deposition Platinum on SrTiO3 (001). Chemistry of Materials, 2009. 21(3): p. 516-521.

35. Hoover, R.R. and Y.V. Tolmachev, Electrochemical Properties of Pt Coatings on Ni Prepared by Atomic Layer Deposition. Journal of the Electrochemical Society, 2009. 156(1): p. A37-A43.

36. King, J.S., et al., Ultralow loading Pt nanocatalysts prepared by atomic layer deposition on carbon aerogels. Nano Letters, 2008. 8(8): p. 2405-2409.

37. Zhou, Y., et al., Optimal preparation of Pt/TiO2 photocatalysts using atomic layer deposition. Applied Catalysis B-Environmental, 2010. 101(1-2): p. 54-60.

38. George, S.M., Atomic Layer Deposition: An Overview. Chemical Reviews, 2010. 110(1): p. 111-131.

39. George, S.M., A.W. Ott, and J.W. Klaus, Surface chemistry for atomic layer growth. Journal of Physical Chemistry, 1996. 100(31): p. 13121-13131.

40. Puurunen, R.L., Surface chemistry of atomic layer deposition: A case study for the trimethylaluminum/water process. Journal of Applied Physics, 2005. 97(12): p. -.

41. Liang, X.H., et al., Alumina atomic layer deposition nanocoatings on primary diamond particles using a fluidized bed reactor. Diamond and Related Materials, 2008. 17(2): p. 185-189.

42. Weimer, A.W., et al., Atomic layer deposition of TiO2 films on particles in a fluidized bed reactor. Powder Technology, 2008. 183(3): p. 356-363.

43. Weimer, A.W., et al., Alumina atomic layer deposition nanocoatings on primary diamond particles using a fluidized bed reactor. Diamond and Related Materials, 2008. 17(2): p. 185-189.

44. Aarik, J., et al., Atomic layer deposition of titanium dioxide from TiCl4 and H2O: investigation of growth mechanism. Applied Surface Science, 2001. 172(1-2): p. 148-158.

45. Cheng, H.E., C.M. Hsu, and Y.C. Chen, Substrate Materials and Deposition Temperature Dependent Growth Characteristics and Photocatalytic Properties of ALD TiO2 Films. Journal of the Electrochemical Society, 2009. 156(8): p. D275-D278.

46. Pore, V., et al., Atomic layer deposition of photocatalytic TiO2 thin films from titanium tetramethoxide and water. Chemical Vapor Deposition, 2004. 10(3): p. 143-148.

47. King, D.M., et al., Atomic layer deposition of TiO2 films on particles in a fluidized bed reactor. Powder Technology, 2008. 183(3): p. 356-363.

48. King, D.M., et al., In situ synthesis of TiO2-functionalized metal nanoparticles. Industrial & Engineering Chemistry Research, 2009. 48(1): p. 352-360.

49. Kim, K.H., et al., Atomic layer deposition of insulating nitride interfacial layers for germanium metal oxide semiconductor field effect transistors with high-kappa oxide/tungsten nitride gate stacks. Applied Physics Letters, 2007. 90(21).

50. Roh, Y., et al., HfO2 gate insulator formed by atomic layer deposition for thin-film-transistors. Thin Solid Films, 2007. 515(12): p. 5109-5112.

51. George, S.M., et al., Surface chemistry and film growth during TiN atomic layer deposition using TDMAT and NH3. Thin Solid Films, 2003. 436(2): p. 145-156.

52. Puurunen, R.L., et al., Growth of aluminum nitride on porous alumina and silica through separate saturated gas-solid reactions of trimethylaluminum and ammonia. Chemistry of Materials, 2002. 14(2): p. 720-729.

53. Sauls, F.C., L.V. Interrante, and Z.P. Jiang, Me3al.Nh3 Formation and Pyrolytic Methane Loss - Thermodynamics, Kinetics, and Mechanism. Inorganic Chemistry, 1990. 29(16): p. 2989-2996.

54. Puurunen, R.L.R., A.; Sarv, P.; et al, Growth of aluminium nitride on porous silica by atomic layer chemical vapour deposition. Applied Surface Science 2000. 165: p. 193-202.

55. Bartram, M.E., et al., Nucleation and Growth of Ain - Self-Limiting Reactions and the Regeneration of Active-Sites Using Sequential Exposures of Trimethylaluminum and Ammonia on Silica at 600 K. Chemistry of Materials, 1993. 5(10): p. 1424-1430.

56. Serpone, N., et al., Subnanosecond Relaxation Dynamics in Tio2 Colloidal Sols (Particle Sizes R(P)=1.0-13.4 Nm) - Relevance to Heterogeneous Photocatalysis. Journal of Physical Chemistry, 1995. 99(45): p. 16655-16661.

57. Kryukova, G.N., et al., Structural peculiarities of TiO2 and Pt/TiO2 catalysts for the photocatalytic oxidation of aqueous solution of Acid Orange 7 Dye upon ultraviolet light. Applied Catalysis B-Environmental, 2007. 71(3-4): p. 169-176.

58. Law, S., The effect of Platinum and Silver deposits in the photocatalytic oxidation of resorcinol. Applied Catalysis B-Environmental, 2007. 72: p. 363-372.

59. Einaga, H., S. Futamura, and T. Ibusuki, Improvement of catalyst durability in benzene photooxidation by rhodium deposition on TiO2. Chemistry Letters, 2001(6): p. 582-583.

60. Sano, T., et al., Photocatalytic degradation of gaseous acetaldehyde on TiO2 with photodeposited metals and metal oxides. Journal of Photochemistry and Photobiology a-Chemistry, 2003. 160(1-2): p. 93-98.

61. Lee, S.L. and J. Scott, Gas-phase phtocatalytic degradation of volatile organic compounds using metallised titania, in Chemeca 2007. 2007: Australis.

62. Cho, K., et al, Photocatalytic performance of Pt-loaded TiO2 in the decomposition of gaseous ozone. Journal of Photochemistry and Photobiology a-Chemistry, 2004. 161: p. 155-161.

63. Kraeutler, B. and A.J. Bard, Heterogeneous Photocatalytic Synthesis of Methane from Acetic-Acid - New Kolbe Reaction Pathway. Journal of the American Chemical Society, 1978. 100(7): p. 2239-2240.

64. Lam, S., et al, The effect of Platinum and Silver deposits in the photocatalytic oxidation of resorcinol. Applied Catalysis B-Environmental, 2007. 72: p. 363-372.

65. Sano, T., et al, Degradation of toluene and acetaldehyde with Pt-loaded TiO2 catalyst and parabolic trough concentrator. Solar enengy, 2004. 77: p. 543-552.

66. Yamakata, A., T. Ishibashi, and H. Onishi, Water- and oxygen-induced decay kinetics of photogenerated electrons in TiO2 and Pt/TiO2: A time-resolved infrared absorption study. Journal of Physical Chemistry B, 2001. 105(30): p. 7258-7262.

67. Ishitani, O., et al., Photocatalytic Reduction of Carbon-Dioxide to Methane and Acetic-Acid by an Aqueous Suspension of Metal-Deposited Tio2. Journal of Photochemistry and Photobiology a-Chemistry, 1993. 72(3): p. 269-271.

68. Vorontsov, A.V., E.N. Savinov, and Z.S. Jin, Influence of the form of photodeposited platinum on titania upon its photocatalytic activity in CO and acetone oxidation. Journal of Photochemistry and Photobiology a-Chemistry, 1999. 125(1-3): p. 113-117.

69. Gratzel, M., Efficient Water Cleavage by Visible-Light in Colloidal Solutions of Bifunctional Redox Catalysts. Abstracts of Papers of the American Chemical Society, 1981. 181(Mar): p. 13-Inor.

70. Mills, A., Platinisation of Semiconductor Particles. J.Chem.Soc.,Chem.Commun., 1982: p. 367.

71. Hiehata, K., A. Sasahara, and H. Onishi, Local work function analysis of Pt/TiO2 photocatalyst by a Kelvin probe force microscope. Nanotechnology, 2007. 18(8): p. -.

72. Floro, J.A., et al., The dynamic competition between stress generation and relaxation mechanisms during coalescence of Volmer-Weber thin films. Journal of Applied Physics, 2001. 89(9): p. 4886-4897.

73. Manke, C., et al., Atomic vapor deposition of Ru and RuO2 thin film layers for electrode applications. Microelectronic Engineering, 2005. 82(3-4): p. 242-247.

74. Liu, C.W., C.C.; Kei C.C.; Hsueh, Y.C.; Perng, T.P., Atomic ayer deposition of platinum nanoparticles on carbon nanotubes for application in proton-exchange membrane fuel cells, in Fuel cells. 2009. p. No.x,1-4.

75. Aaltonen, T., et al., Atomic layer deposition of platinum thin films. Chemistry of Materials, 2003. 15(9): p. 1924-1928.

76. Aaltonen, T., et al., Reaction mechanism studies on atomic layer deposition of ruthenium and platinum. Electrochemical and Solid State Letters, 2003. 6(9): p. C130-C133.

77. Kessels, W.M.M., et al., Surface reactions during atomic layer deposition of Pt derived from gas phase infrared spectroscopy. Applied Physics Letters, 2009. 95(1).

78. Capelle, K., A bird's-eye view of density-functional theory. Brazilian Journal of Physics, 2006. 36(4A): p. 1318-1343.

79. Argaman, N. and G. Makov, Density functional theory: An introduction. American Journal of Physics, 2000. 68(1): p. 69-79.

80. Cramer, C.J., Essentials of comutational chemistry. 2004.

81. Cross, E.K.U. and R.M. Dreizler, eds. Density Functional Theory. 1995.

82. Hinchliffe, A., ed. Computational quantum chemistry. 1989.

83. Hafner, J., Materials simulations using VASP - a quantum perspective to materials science. Computer Physics Communications, 2007. 177(1-2): p. 6-13.

84. Hafner, J., Ab-initio simulations of materials using VASP: Density-functional theory and beyond. Journal of Computational Chemistry, 2008. 29(13): p. 2044-2078.

85. Shu, C., N. Sukumar, and C.P. Ursenbach, Adsorption of O-2 on TiO2(110): A theoretical study. Journal of Chemical Physics, 1999. 110(21): p. 10539-10544.

86. Truong, T.N., V. Shapovalov, and E.V. Stefanovich, Nature of the excited states of the rutile TiO2(110) surface with adsorbed water. Surface Science, 2002. 498(1-2): p. L103-L108.

87. Valdes, A., et al., Oxidation and photo-oxidation of water on TiO2 surface. Journal of Physical Chemistry C, 2008. 112(26): p. 9872-9879.

88. Aschauer, U., J. Chen, and A. Selloni, Peroxide and superoxide states of adsorbed O(2) on anatase TiO(2) (101) with subsurface defects. Physical Chemistry Chemical Physics, 2010. 12(40): p. 12956-12960.

89. Castellani, N.J., et al., Theoretical modeling of photocatalytic active species on illuminated TiO2. Applied Surface Science, 2007. 254(1): p. 32-35.

90. Gong, X.Q. and A. Selloni, Role of steps in the reactivity of the anatase TiO2(101) surface. Journal of Catalysis, 2007. 249(2): p. 134-139.

91. Cheng, H.Z. and A. Selloni, Energetics and diffusion of intrinsic surface and subsurface defects on anatase TiO(2)(101). Journal of Chemical Physics, 2009. 131(5).

92. Gong, X.Q., et al., Small au and pt clusters at the anatase TiO2(101) surface: Behavior at terraces, steps, and surface oxygen vacancies. Journal of the American Chemical Society, 2008. 130(1): p. 370-381.

93. Liu, C.J., Y. Han, and Q.F. Ge, Interaction of Pt clusters with the anatase TiO2(101) surface: A first principles study. Journal of Physical Chemistry B, 2006. 110(14): p. 7463-7472.

94. Deskins, N.A., D.H. Mei, and M. Dupuis, Adsorption and diffusion of a single Pt atom on gamma-Al(2)O(3) surfaces. Surface Science, 2009. 603(17): p. 2793-2807.

95. Neyman, K.M., A. Bruix, and F. Illas, Adsorption, Oxidation State, and Diffusion of Pt Atoms on the CeO(2)(111) Surface. Journal of Physical Chemistry C, 2010. 114(33): p. 14202-14207.

CHAPTER 2

Synthesis of Photoactive Magnetic Nanoparticles with Atomic Layer Deposition

Abstract

Iron-based magnetic nanoparticles have been produced by decomposition of iron oxalate powder. The micrometer size iron oxalate powder was first ground by use of a cryogenic milling process. A titanium dioxide (TiO_2) thin film was then deposited on the synthesized iron nanoparticles with an *in-situ* atomic layer deposition (ALD) process at 100 ^oC with $TiCl_4$ and H_2O_2 as precursors. However, due to the high surface area, the iron nanoparticles were unstable and spontaneously oxidized when exposed to H_2O_2 during the TiO_2 ALD process, thus reducing the magnetic moment of the core particles. As an improvement in the process, prior to the TiO_2 deposition, an aluminum nitride (AlN) film was deposited *in-situ* to coat and passivate the iron core particles. The AlN ALD was performed at 250 ^oC with trimethylaluminium (TMA) and ammonia (NH_3) as precursors. This passivation provided a significant decrease in the iron oxidation as determined by X-ray diffraction and magnetization measurements. Photoactivity of the TiO_2 film was demonstrated by decomposition of methylene blue solution under ultraviolet irradiation.

2.1 Introduction

Photocatalysis has recently received widespread interest and commercialization as a passive means of purification. At present, titanium dioxide (TiO_2) is one of the few photoactive materials suitable for industrial use due to its chemical stability, low cost, non-toxic nature and

high photoactivity [1, 2]. TiO_2 is already widely used in many commercial products such as pigments, sunscreens, paints, ointments and toothpastes [3]. Since the discovery of the photocatalytic property of TiO_2 in the 1970's, the scientific and engineering interest in the applications of TiO_2 materials has grown exponentially. Enormous effort has been devoted to research that utilizes TiO_2 for water-splitting, solar cells, sensors and electrochemical devices [2, 3].

More significantly, its application to pollutant clean-up has been reported extensively, making TiO_2 promising for environmental treatment [4-7]. As a durable photocatalyst, TiO_2 has been shown to be efficient for the destruction of a broad range of pollutants, including organic and inorganic chemicals and even bacteria [4]. This makes TiO_2 very popular for applications involving environmental treatment, such as wastewater remediation and air purification.

A variety of photochemical reactors has been designed for environmental remediation [8]. A fixed-bed reactor with immobilized TiO_2 particles coated on reactor walls or other solid supports is employed in many applications. However, this type of reactor has several drawbacks, such as low surface area and inefficiencies caused by absorption and scattering of light by the reaction medium [2, 4]. Slurry reactors can achieve large surface areas with nanosized TiO_2 powders dispersed in the reactor. However, separation of photocatalyst particles from the bulk phase is challenging [5]. The benefits of surface photocatalysts can be integrated with known magnetic separation techniques by creating photoactive magnetic particles. High surface area magnetic photocatalyst particles created by coating TiO_2 films on iron nanoparticles is a promising method to overcome this difficulty.

Magnetic separation via magnetic fields is widely used in many applications, ranging from ore refinement to biotechnology. The high selectivity, high efficiency, and fast rates

offered by magnetic separation are much more appealing than traditional separation techniques such as centrifugation or filtration. Most studies have focused on the use of iron oxides as the magnetic separation component [9, 10]. However, the magnetic moment of iron oxide is low (84 A m^2/kg, bulk Fe_3O_4 value)[11]. Other magnetic materials such as cobalt and nickel attracted little interest for separation applications due to their toxicity [12]. Iron, however, has a higher specific magnetization (220 A m^2/kg, bulk Fe value) than its oxide [11] and is safe for the environment. Therefore, an iron-based magnetic separation process should be more efficient and makes separation with weaker magnetic fields possible.

Iron nanoparticles can be synthesized by thermal decomposition of cryogenically milled iron oxalate powders. This is a simple method to produce ultrafine metal particles and is easily scalable [13]. Due to their high surface area, however, iron nanoparticles are unstable and highly sensitive to oxidation. *In-situ* coating of passivating films after the iron synthesis provides an excellent method to prevent oxidation, as long as the deposited films are non-porous. By preventing the exposure of the iron core particles to the oxidizing environment, a higher magnetization can be retained.

TiO_2 films can be coated via the atomic layer deposition (ALD) technique. TiO_2 ALD has been well-studied, and has been deposited by means of many different precursors [14-16]. $TiCl_4$ and H_2O_2 were selected as precursors in this study as they have been proven to be favorable for TiO_2 ALD [14, 17, 18]. An interesting conundrum arises when attempting to functionalize iron nanoparticle surfaces by TiO_2 films. There is a general desire to minimize the deposition temperature of the ALD film, in order to decrease the propensity for the iron nanoparticles to sinter together. Though the reaction kinetics decreases with temperature, which means a stronger oxidizer typically becomes beneficial, stronger oxidizers can become detrimental for

this system however, from the critical need to prevent the iron from oxidizing. A strategy demonstrated in the work described here to avoid this scenario is the deposition of an oxygen-free barrier film, specifically a nitride layer that can be deposited at a relatively low temperature.

In order to study the effects of the core powder in the presence of an oxygen-free film, aluminum nitride (AlN) was also deposited on particle surfaces with ALD. Trimethylaluminium (TMA) and ammonia (NH_3) were chosen as precursors for AlN ALD. The ALD of AlN can be performed as low as 250 ℃, which is one of the lowest temperature with which nitride layers have been deposited using ALD techniques [19].

The goal of this study is to develop methods to produce photocatalytically active magnetic nanocomposite materials with ALD on iron particles. The particle size of iron oxalate powders is reduced by use of cryogenic milling techniques, and iron powders are produced via standard thermal decomposition processes. Photoactive TiO_2 films are deposited on the surfaces of primary particles, and AlN interlayers are tested as an option to prevent the iron surfaces from being exposed to oxygen-containing precursors used in TiO_2 ALD. The magnetic moment of the composite particles is measured, and the photoactivity of the TiO_2 surfaces is studied. In this fashion, a recoverable and reusable magnetic photocatalyst can be synthesized. By combining the benefits of surface photocatalysts with a high magnetic separation effect, this novel magnetic photocatalyst is believed to be an efficient, cost-effective and environmentally-friendly means for environmental remediation.

2.2 Experimental Methods

2.2.1 Synthesis of iron nanoparticles

Iron nanoparticles were produced from thermal decomposition of iron oxalate dihydrate ($FeC_2O_4 \cdot 2H_2O$, Sigma Aldrich), which was purchased in powder form, having a surface area of 0.56 m^2/g and particle density of 2.28 g/cm^3. The decomposition behavior was first studied with a thermo-gravimetric analyzer (TGA, Theta Industries) in order to help understand the decomposition mechanism and to explore the optimum operating conditions.

In order to obtain nano-scale iron particles with desirable surface areas, iron oxalate powders were cryogenically milled to reduce the starting particle size. The cryomilling apparatus included a high energy attritor (01-HD, Union Process) that was modified to allow for the continuous flow of liquid nitrogen into the mill. The addition of liquid N_2 created a low temperature milling environment, which increased the brittleness of the oxalate particles. Witkin et al showed that mechanical grinding in liquid N_2 allows for much shorter milling time to reach the finest particle sizes and smaller recrystallized grain sizes when compared to grinding performed in air [20]. The milling mixture was a slurry consisting of flowing liquid nitrogen, iron oxalate powder and MgO stabilized ZrO_2 milling media. The size of the ZrO_2 media was 2 mm. The incorporation of ethanol was also studied during the milling process. When ethanol was added to the milling mixture, the volume ratio of the oxalate powder to ethanol was 2:1. The attrition times ranged from 3 to 15 hrs in order to study the optimum milling time. A 15 hr standard room-temperature ball milling experiment was also performed for comparison. Except for the temperature and the nitrogen, other components of the milling mixture were the same as those used during the cryogenic milling.

After the milling process was completed, iron oxalate powder was placed in a fluidized bed reactor (FBR) to produce iron nanoparticles. Water and carbon dioxide were removed at elevated temperatures of 180 ℃ and 430 ℃, for dehydration and decomposition, respectively.

The FBR system consisted of a reactor column, a vibration generation system, a gas flow control system, an *in-situ* mass spectrometer, and a rotary vane vacuum pump. This reactor configuration has been described in more detail elsewhere [21]. A fluidized bed system is desirable for this application in order to prevent sintering due to prolonged contact of the newly produced iron nanoparticle surfaces. The main advantages of the FBR include excellent gas/solid mixing, thermal efficiency, and stable operating conditions. It was operated at reduced pressures and under mechanical vibration to assist fluidization. For a typical run, the minimum fluidization velocity of the iron oxalate powder was about 0.5 cm/s, which can be determined by recording the pressure drop across the bed versus the N_2 superficial gas velocity, as shown in Figure 2.1. The pressure inside the reactor created by this gas flow rate was approximately 8 Torr. In order to produce a reductive atmosphere to assist the decomposition reaction, a 30% H_2 in N_2 mixture was used. The flow rates of the precursors were manually adjusted to the fluidization pressure drop at the beginning of each run.

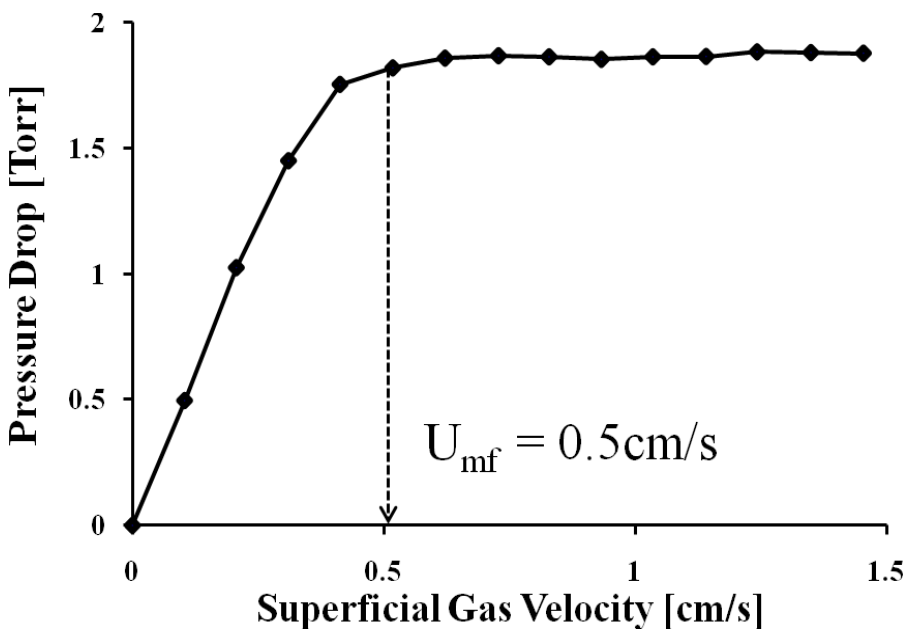

Figure 2.1 Fluidization curve for a typical iron oxalate powder decomposition process.

2.2.2 TiO_2 and AlN ALD

After the decomposition process, the synthesized iron nanoparticles were coated by ALD thin films in the same FBR. The *in-situ* process can help to prevent the iron particles from being exposed to air, thus avoiding oxidization before the coating process. The TiO_2 ALD process was operated at 100 ℃, with $TiCl_4$ and H_2O_2 used as precursors. Due to the strong oxidizing activity of H_2O_2, this deposition temperature is lower than the reported TiO_2 ALD temperature when H_2O is used, which is typically around 300 ℃. The deposition temperature of AlN ALD was 250 ℃. This temperature was carefully chosen so that chemisorption takes place, instead of physisorption or decomposition. Above 327 ℃, the thermal decomposition of TMA will occur [22, 23]. Moreover, since this reaction is exothermic, the local temperature around the particles is likely to be higher than the overall reactor temperature. Although a lower deposition temperature can prevent the thermal decomposition of TMA, if the ALD temperature is too low, the overall reaction kinetics during the NH_3 step will be too slow [22-25].

During each ALD reaction, two precursors were alternately dosed into the reactor separated by a N_2 purge step, which was critical to remove by-products and remaining precursors. Liquid precursors of TMA, $TiCl_4$ and H_2O_2 were fed into the reactor with their room-temperature vapor pressure maintained as the driving force. The flow rates of these precursors were adjusted with needle valves used to provide a pressure drop across the particle bed sufficient to promote and maintain the fluidized state of the iron substrate particles. For the purge N_2 gas, the flow rate was controlled by a mass flow controller (MKS Instruments).

A mass spectrometer (QMS200, Stanford Research Systems) was attached to the outlet of the reactor to monitor the progression of ALD half-reactions by analyzing a side-stream of gas exiting the reactor. The pressure signal of the reactants, products, and their fragmentation species

were recorded over time. With the *in-situ* mass spectrometer signal, the reaction behavior of each cycle was clearly visible and the dosing times could be optimized by observing reaction product evolution and subsequent unreacted precursor breakthrough. Due to the corrosive HCl by-product, special precautions were taken during the TiO_2 ALD. We deliberately used a longer purge times than typically required. In order to protect the vacuum pump, two traps filled with sodium bicarbonate powder were placed upstream of the pump to neutralize the strongly acidic gaseous byproduct.

2.2.3 Analytical techniques

A particle size analyzer (Mastersizer 2000, Malvern) was used to measure the size distribution information of the oxalate powders both before and after the milling processes. The particle size distributions (PSD) were determined by collecting light scattering data on an array of detectors and then calculating the particle size by means of Mie theory. Wet dispersion was used for the analysis with water as the dispersant. The specific surface area of each powder type was measured with a BET Surface Area Analyzer (Gemini V, Micromeritics) that used N_2 as the adsorbate species. High resolution transmission electron microscopy (HRTEM) and scanning transmission electron microscopy (STEM) images were obtained with a JEOL 2010F 200 kV Schottky field emission transmission electron microscope equipped with an Oxford detector unit for elemental analysis while imaging. The crystallinity of the nanostructures was characterized by powder X-ray diffraction (XRD, PAD5, Scintag, Inc.). The XRD pattern was recorded from 25 °to 70 °at a rate of 2 °/min. Inductively coupled plasma atomic emission spectroscopy (ICP-AES) was used to measure the deposited Ti and Al content of the films. During the measurement, the particles were first digested in H_2SO_4 solution with periodic agitation for a time sufficient to

ensure complete dissolution. The dissolved Al and Ti content, in parts per million, was then measured with an Applied Research Laboratories ICP-AES 3410+. The oxygen content was measured with a LECO oxygen analyzer (TC600, LECO) to study the amount of oxidation of iron core particles from the oxidative precursors. During this test, the oxygen released from the sample combines with the carbon provided to form CO and a small amount of CO_2. By infrared detection of CO and CO_2 in an IR cell, the oxygen content can be determined. A magnetometer based on a superconducting quantum interference device (SQUID) (MPMS-7, Quantum Design, San Diego, California) was used to measure the magnetic properties of the particles.

2.2.4 Photoactivity testing

The photoactivity of the TiO_2 ALD films was evaluated by studying the decomposition kinetics of a methylene blue (MB, Sigma Aldrich) solution. The concentration of the MB aqueous solution was 10 ppm. After a certain amount of sample powder, typically 0.1 grams, was dispersed in 100 ml MB solution, the mixture was kept in the dark until a steady-state was detected. After the adsorption/desorption equilibration was achieved, a 100 W UV lamp (Mineralogical Research Co.) having a wavelength of 360 nm was positioned at a distance of 10 cm above the solution. The strength of the UV light at the surface of the solution was measured to be ~12 mW/cm^2 by a radiometer/photometer (IL1400A, International Light). The solution was continuously stirred throughout the entire test process because particle dispersion improves the reaction kinetics. Samples of constant volume (2.5 mL) were removed from the solution at regular time intervals, typically 30 minutes. The concentration of each MB sample was determined by the absorbance at a wavelength of 664 nm with a UV/Vis spectrophotometer

(Lambda 35, Perkin Elmer). From the decrease in MB concentration with UV irradiation time, the photocatalytic activity of the test particles can be evaluated.

2.3 Results and Discussion

2.3.1. Size reduction of the oxalate feed powder

Prior to the decomposition process, several iron oxalate size reduction experiments were performed in order to determine an optimal procedure. First, the milling process was performed with and without ethanol. Surface area results, shown in Figure 2.2a, suggest that the addition of ethanol increases the milling efficiency. For example, the surface area of the oxalate powder, after cryomilling for 15 hrs, was 28.3 m^2/g with ethanol added and 15.2 m^2/g for the process without ethanol. This observation is in accordance with the theory that solvent-based grinding changes the attrition mechanism from collision to friction, which has been demonstrated to be more effective in milling ultrafine powders [13]. Second, the 15 hr ball milling run was performed for comparison in order to demonstrate the advantages of cryomilling. The particle surface area was only 4.1 m^2/g after 15 hrs of ball milling. Even after three hours of cryomilling, the powder surface area (12.9 m^2/g) was more than triple that of the sample that was ball milled for 15 hours. This also suggests that the added process cost of milling under cryogenic conditions may be economically competitive to ball milling from a process time savings perspective.

The effect of cryogenic milling time was studied by varying the extent of milling for 0, 3, 6, 9 and 15 hrs. All of these milling processes were performed using the solvent-based method by adding ethanol as a solvent into the mixture to make the slurry viscous. It is clear that as the cryomilling time was increased, the surface area of the feed powder increased, but the increase

trend diminished with time. The cumulative particle size distributions of the cryomilled powders are shown in Figure 2.2b. This figure clearly shows that the particle sizes uniformly shifted toward smaller size regions with the increase of milling time. This uniform shift indicated that the breakage was more dominant than reaggregation, which is generally believed to be unavoidable during the milling process. The efficiency of the first three hours of milling is apparent significant, as the median particle size decreased from 15 μm to approximately 2 μm. After 15 hrs milling, the majority of the particle sizes fell below 1 μm, while the efficiency of the subsequent 12 hrs was obviously lower than the first 3 hrs. This declining size reduction rate can be explained by the homogeneous primary particles becoming stronger and more difficult to break as the size decreases.

Figure 2.2c shows the volume distributions of the unmilled, ball milled and cryomilled powders, for milling times of 15 hrs. The ball milling technique does an adequate job of reducing the size of the coarse particles to a median size less than 10 microns, but it also does reduce the size of the fine particles less than 1 micron in size. The cryogenic milling technique significantly reduces the size of both the coarse and fine particles, to the extent that a true bimodal distribution is created. The median particle size of the larger particles falls below 1 micron, to approximately 900 nm, and maximum size appears to be less than 10 microns. The median size of the fine particles produced from the 15 hr cryomilling process was approximately 200 nm. The area under the smaller curve of the bimodal distribution is even more significant because this is a plot of the volume fraction, and the volume of a 200 nm particle is four orders of magnitude smaller than the volume of a 5 micron particle.

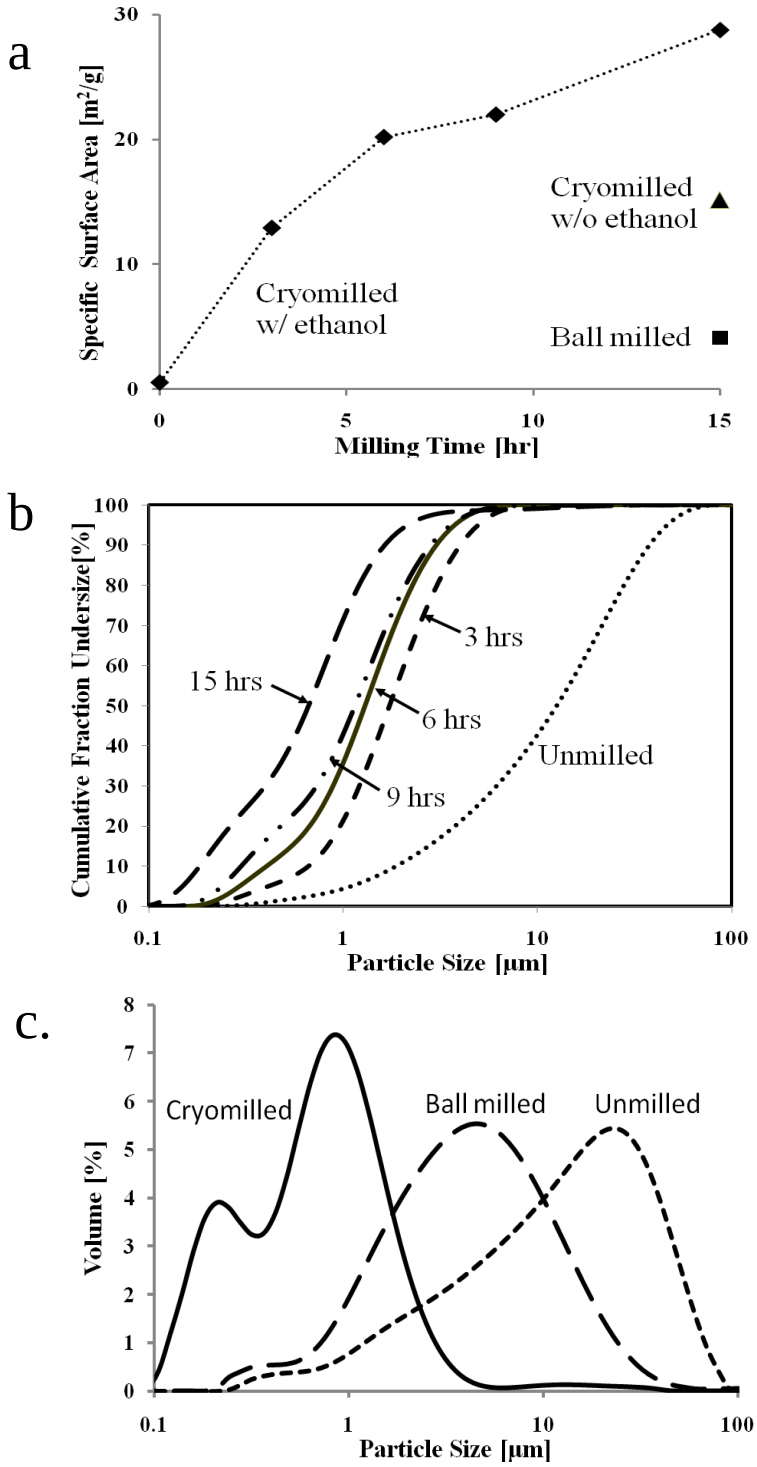

Figure 2.2 (a) Surface area results of the oxalate powder after different milling processes; (b) Cumulative size distributions of the unmilled and cryomilled oxalate powders after different time periods. (c). Volume distributions of the unmilled oxalate powder, and after 15 hrs of ball milling and 15 hrs of cryogenic cryomilling.

Iron nanoparticles were produced by the thermal decomposition of cyromilled iron oxalate powders. The decomposition behavior was studied in advance by heating a small quantity of oxalate powder in a TGA. A representative TGA plot is shown in Figure 3.3. First, the iron oxalate dihydrate powder released water molecules, resulting in a mass loss of approximately 20%. This step occurred at 180 ℃. Then the $Fe(CO_2)_2$ decomposed to Fe_3O_4, which is further reduced to the final product, Fe. The overall mass loss was approximately 69%. The decomposition step initiated when the temperature reached about 430 ℃. When carrying out the decomposition of a metal salt in a fluidized bed reactor, obtaining pure iron powder can be very difficult, and doing so without exposing it to air can be even more difficult. The slow reduction kinetics of the Fe_3O_4 to Fe reaction can be seen in Figure 3.3. The long tail of mass loss occurred over more than an hour under constant, high-temperature processing. Since there is not an *in-situ* instrument to measure mass loss in the fluidized bed reactor, care must be taken to fully understand the equipment and process. The benefit of the FBR, however, is that decomposed powder does remain in powder form and the particle size can be further reduced by natural breakage during the decomposition process. Whereas in the TGA, stagnant metal powders with reduced surface areas typically result in a porous sintered pellet. After the cryomilling of the feed iron oxalate powders combined with the attrition during the following decomposition process in the FBR, the final particle size of the produced particles was 50-80 nm in primary size.

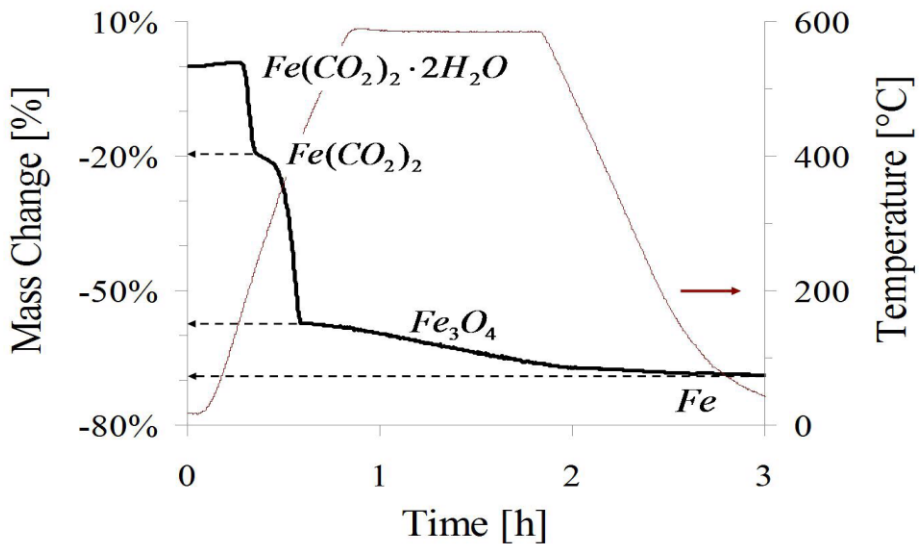

Figure 2.3 Mass loss curve with temperature during the dehydration and decomposition of a small quantity of iron oxalate powder in a TGA.

2.3.2. Magnetic photocatalysts produced via TiO_2 ALD

After the decomposition process, the synthesized iron nanoparticles were coated with TiO_2 films to produce the magnetic photocatalyst. 150 ALD cycles of TiO_2 were deposited with $TiCl_4$ and H_2O_2 used as precursors. The coating process was studied by means of an *in situ* mass spectrometer, which demonstrated that this ALD reaction was self-limiting and self-terminating. After this magnetic photocatalyst was produced, the ICP-AES analysis revealed that the Ti content was 11.0 wt%. This elemental analysis suggested that the TiO_2 film concentration was approximately 18.3 wt% based on a stoichiometic calculation. In order to closely observe the film characteristics, the coated particles were analyzed by HRTEM and EDS. A TEM image and EDS spectrum of the TiO_2 coated iron particles are shown in Figure 2.4. The images clearly show that the deposited film was uniform and conformal over the surface of the individual iron nanoparticle. The EDS spectra confirm the presence of only Ti in the film area and both Ti and Fe when probing the center of the particle (as the beam passes through the thin TiO_2 shell as

well). The copper peaks were caused by the TEM grid used to support the particles during the analysis, and the carbon peaks are from the background surface carbon. From visual inspection, the TiO_2 film growth rate for this process was approximately 0.3 Å/cycle. This was lower than reported values for these precursors at the deposition temperature used here, but the precursors were specifically dosed at sub-saturating exposure levels.

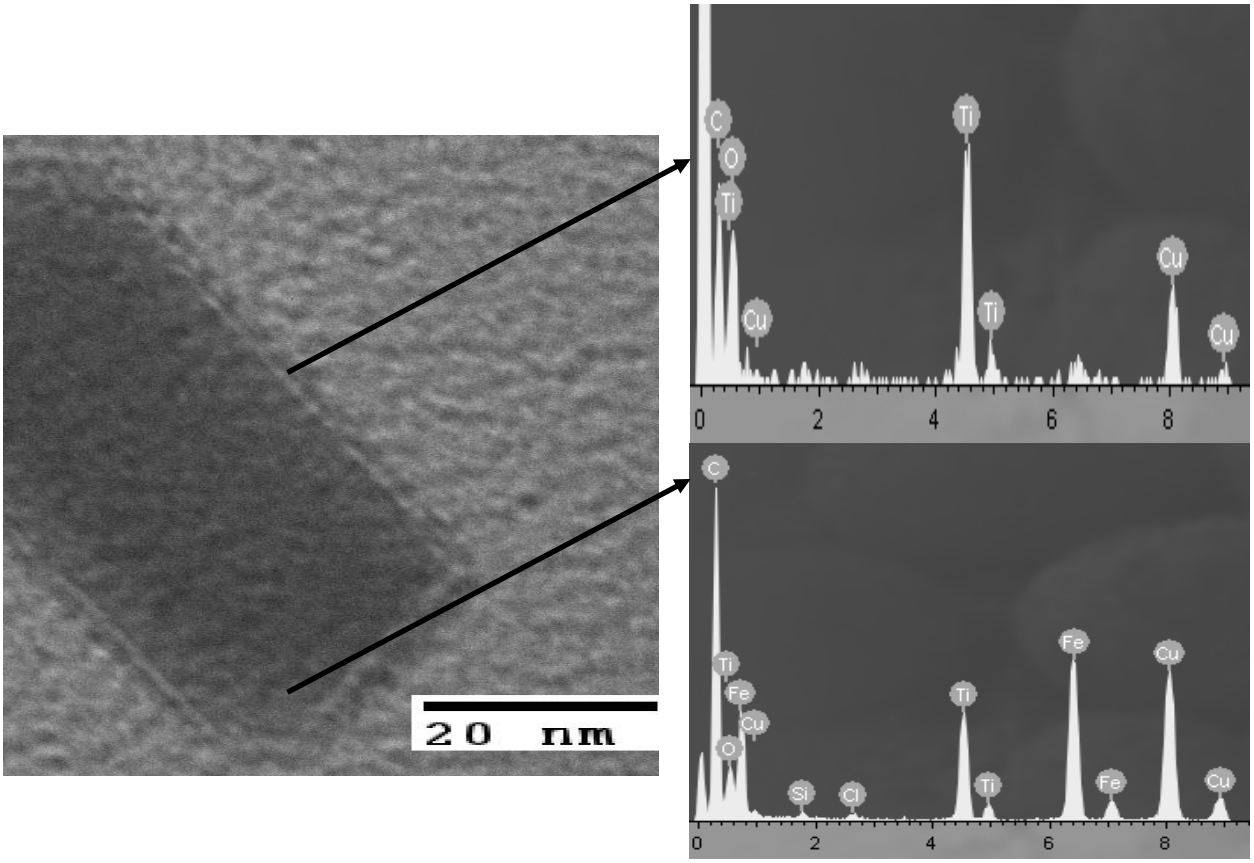

Figure 2.4 HRTEM and EDS spectrum of TiO_2 coated iron particles.

The photoactive property of the TiO_2 coated iron particles was studied by evaluating the decomposition behavior of methylene blue (MB) solution under UV illumination. For comparison, the photoactivity measurement was also carried out for uncoated iron particles as well as the commercial TiO_2 P-25 photocatalyst. The result is shown in Figure 2.5, where the relative concentration of MB, $\ln(C/C_0)$, is plotted logarithmically against the UV light irradiation

time. Typically, the MB photocatalytic decomposition on the TiO_2 surface follows pseudo-first-order kinetics, dC/dt = kC, where k is the pseudo-first-order rate constant. After integration [$\ln(C/C_0) = kt$], k is obtained from the slope of a linear fit of experimental data. As the figure shows, the uncoated particles indicate no photocatalytic activity. On the other hand, when TiO_2 coated particles were dispersed in the MB solution, the graph exhibits the MB degradation with UV irradiation time and the rate constant is 0.01/min. For the commercial TiO_2 P-25 photocatalyst, the rate constant was only four times that of this TiO_2 ALD produced magnetic photocatalyst. These results clearly demonstrate the functional property of TiO_2 films to provide photocatalytic activity to the core particles.

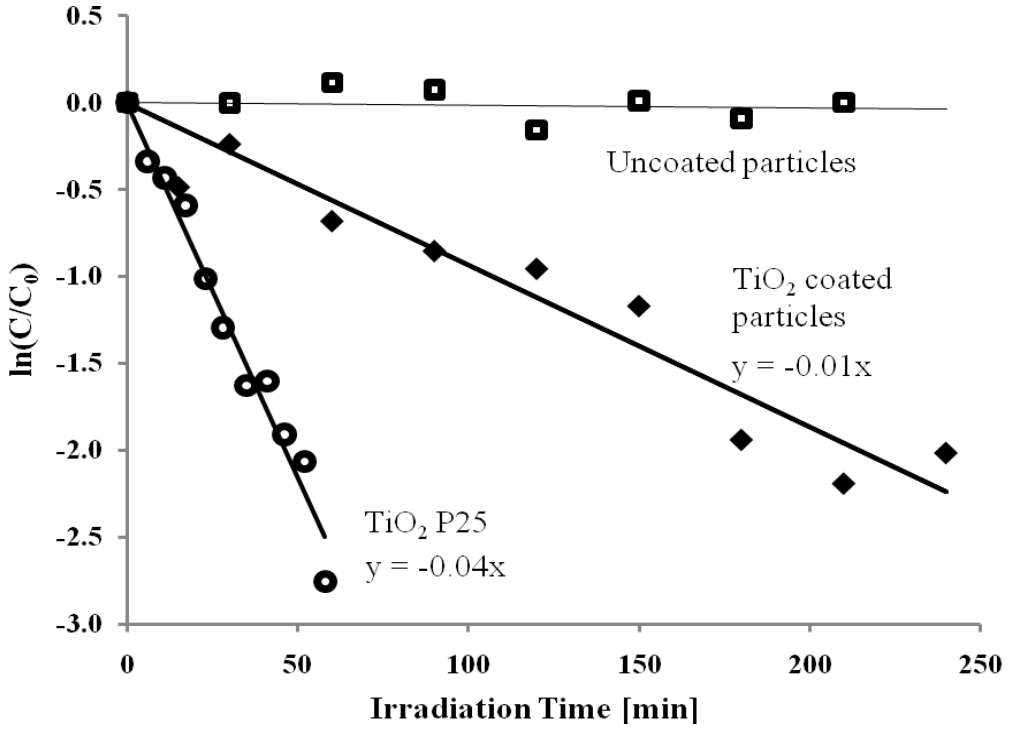

Figure 2.5 Relative concentration of MB vs. irradiation time for uncoated and TiO_2 coated iron particles as well as the commercial TiO_2 P-25 photocatalyst.

The oxygen content of the TiO_2 coated samples was measured with a LECO oxygen analyzer. The oxygen content of the coated particles was 26.3 wt%. However, the theoretical oxygen content calculated from the TiO_2 film contribution only amounts to 7.3 wt%. The higher experimental oxygen content than the theoretical value is due to the partial oxidation of the iron core particles. Instead of pure iron particles, the synthesized iron was partially oxidized during the TiO_2 ALD process. Based on the growth rate of TiO_2 ALD, it can take more than 10 cycles to yield one full monolayer, or continuous film of the metal oxide. Until that point, the oxidizing precursor has an opportunity to react with the bare iron surfaces of the particles. Even after the TiO_2 layer is growing in a continuous fashion, oxygen transport to the iron core may not be fully inhibited until a sufficient number of cycles has been applied.

The XRD spectra confirm the presence of iron oxide and indentified that it was in the form of Fe_3O_4, as shown in Figure 2.6. The TiO_2 crystal structure was not detected here because it should be amorphous at the deposition temperature used in this study. Even if it was crystalline however, the film thickness is still below the detectable limit of the powder XRD machine. Since bulk Fe possesses a higher saturation magnetization level than that of bulk Fe_3O_4, the oxidation of Fe should reduce the magnetic moment of the magnetic photocatalyst. In this case, a higher magnetic field would be required in the environmental remediation process and, therefore, potentially increase the treatment cost.

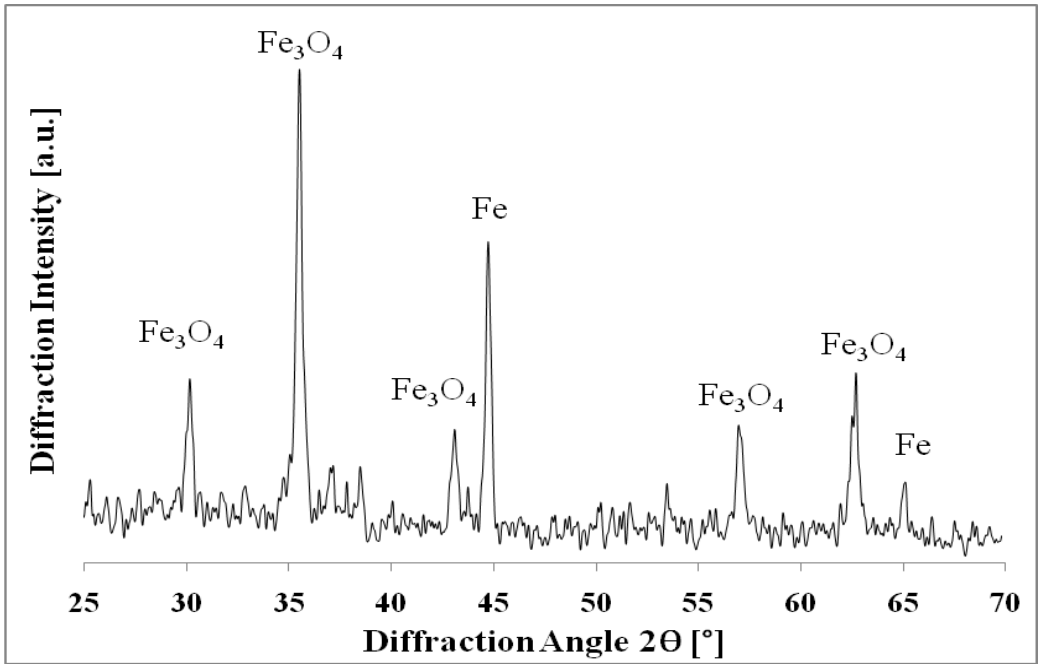

Figure 2.6 XRD spectra of TiO_2 coated particles.

2.3.3. Magnetic photocatalysts produced with AlN interlayer

In order to avoid oxidation, the core iron particles were pre-coated with an oxygen-free film, specifically aluminum nitride. Aluminum nitride was selected due to its ability to be applied at a relatively low deposition temperature. One hundred ALD cycles were deposited after the iron oxalate decomposition process was completed, but prior to the TiO_2 ALD process. The AlN films served as effective oxygen barriers to reduce the oxidation of the iron core particles caused by the TiO_2 oxygen-containing precursor. During the ALD reaction, *in-situ* mass spectrometry was used to monitor all gas phase reactants and products throughout each ALD cycle. A representative mass spectrometry plot for the AlN ALD is shown in Figure 2.7. It represents the m/z responses during the TMA dose period, with the pressure intensity of product on the primary y-axis and that of the reactant on the secondary y-axis.

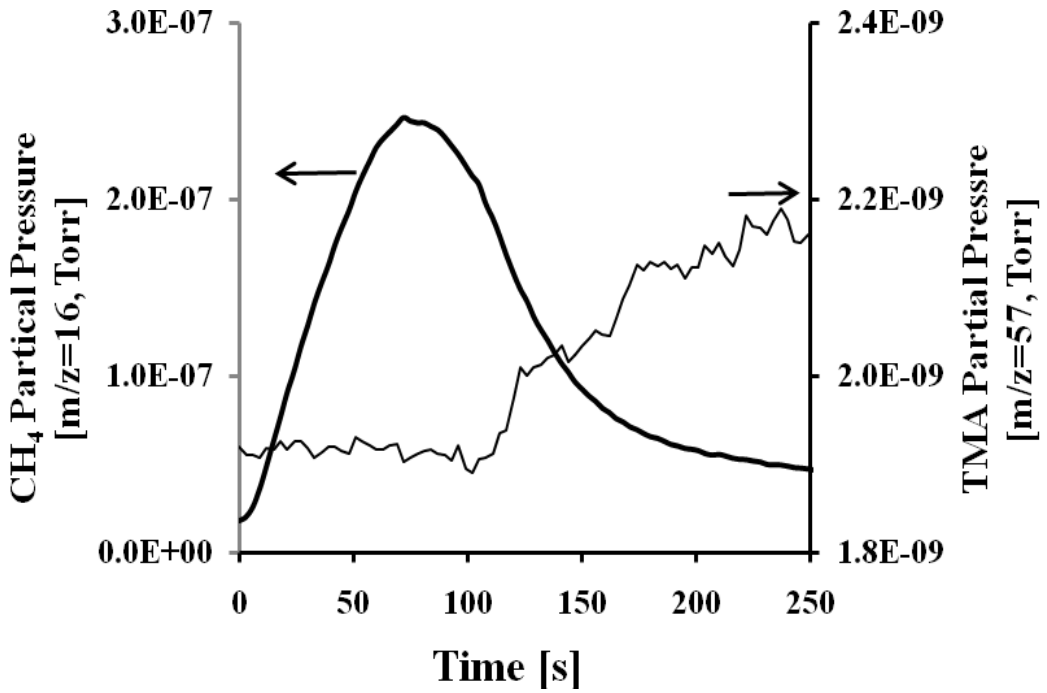

Figure 2.7 A mass spectrometry plot for an AlN half reaction during TMA dosing period.

As the figure shows, when TMA was dosed into the reactor, an instantaneous increase of the CH_4 byproduct was observed. As the dose proceeded, the partial pressure of CH_4 decreased and the TMA signal increased, indicating unreacted TMA breakthrough. It can be seen that before the breakthrough time, all the TMA entering the reactor was completely utilized until the reaction was complete. These data also demonstrate that the reaction was self-limiting, since the reaction products increased and then decreased while the reactants were still being dosed. If these reactions were not self-limiting, the products would continue to be generated as long as the reactant dose proceeded. This demonstrates that particle ALD in a fluidized bed can be operated in a manner such that no precursor is wasted. Therefore, the dose step was generally stopped after the reaction was over in order to reduce unnecessary precursor waste. Following the N_2 purge step that removed any residual TMA precursor and byproducts, the NH_3 precursor was dosed into the reactor. In this step, similar self-limiting behavior was again observed with *in-situ*

mass spectrometry. Underdosing the NH_3 is not critical from a process perspective, and in fact overdosing could be desirable, as NH_3 can be used as a surface reducing agent. Though it is unknown whether overexposure of NH_3 during this nitride ALD process would react with the bare metal surfaces to form an iron nitride outerlayer.

After 100 cycles of AlN ALD, 150 cycles of TiO_2 ALD were deposited on the iron nanoparticles in a similar fashion as before. TEM analysis was performed on the resulting nanocomposite powder. The image of the composite magnetic photocatalyst is shown in Figure 8. The image clearly shows that the bilayer film is both conformal and uniform. From visual observation, the thickness of each layer is approximately 5 nm, corresponding to the AlN growth rate of 0.5 Å/cycle. ICP analysis for aluminum content and LECO nitrogen content analyses were also performed. The weight percentages of aluminum and elemental nitrogen were approximately 5.9 wt% and 3.0 wt%, respectively, which correspond to an Al:N atomic ratio very close to 1:1. The above results provide strong evidence that layer-by-layer growth of AlN on iron particles can be achieved by means of sequential exposure of TMA and NH_3 at 250 ℃. The deposition temperature for AlN ALD was above 325 ℃ in previous reports[26-28]. This low growth temperature makes AlN ALD significantly more practical for applications where temperature is a critical factor. In this case, the low deposition temperature is desirable in order to prevent the synthesized iron nanoparticles from sintering during the ALD process.

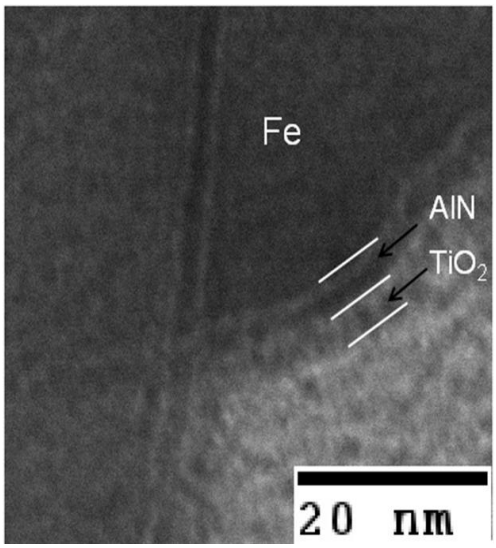

Figure 2.8 TEM image of AlN and TiO_2 bilayer film coated particles.

The oxygen content of the composite particles was also measured with a LECO oxygen analyzer. The analysis revealed that the oxygen content was 10.6 wt%. This value was still higher than the theoretical value of 7.5 wt%, calculated from the TiO_2 film contribution based on the titanium content measurement obtained with ICP-AES. However, the oxygen quantity reduction is significant when compared with that from the particles that were coated only with TiO_2, at 26.3% oxygen. The XRD spectra shown in Figure 2.9 confirm the difference between the TiO_2 coated particles and the ones modified by an AlN interlayer. With the AlN film modification, the ratio of the Fe crystal peak intensities relative to those of the Fe_3O_4 became stronger, indicating higher iron content. Though it is clear that Fe_3O_4 was not eliminated, the result provides strong evidence that the AlN film played a critical role in protecting the core iron particles from oxidation by the TiO_2 precursors. The Fe_3O_4 formation may be due to insufficient AlN film thickness. The relatively thin AlN film did not serve as a good enough diffusion barrier to the oxygen-containing precursor in this case, which allowed some amount of H_2O_2 to

diffuse into the bare iron surface. Future studies should be performed to optimize the thickness of nitride layers deposited on metal nanoparticle surfaces. In addition, milder oxygen-containing precursors could be employed for TiO_2 ALD once a nitride layer of adequate thickness to passivate the iron surface is present. Any ALD process that would follow would not be operated at a high enough temperature for nitride particles to sinter to one another. The reason for selecting the stronger oxidant for the first part of the study was to deposit at a lower operating temperature, which would effectively reduce the probability for particles to sinter.

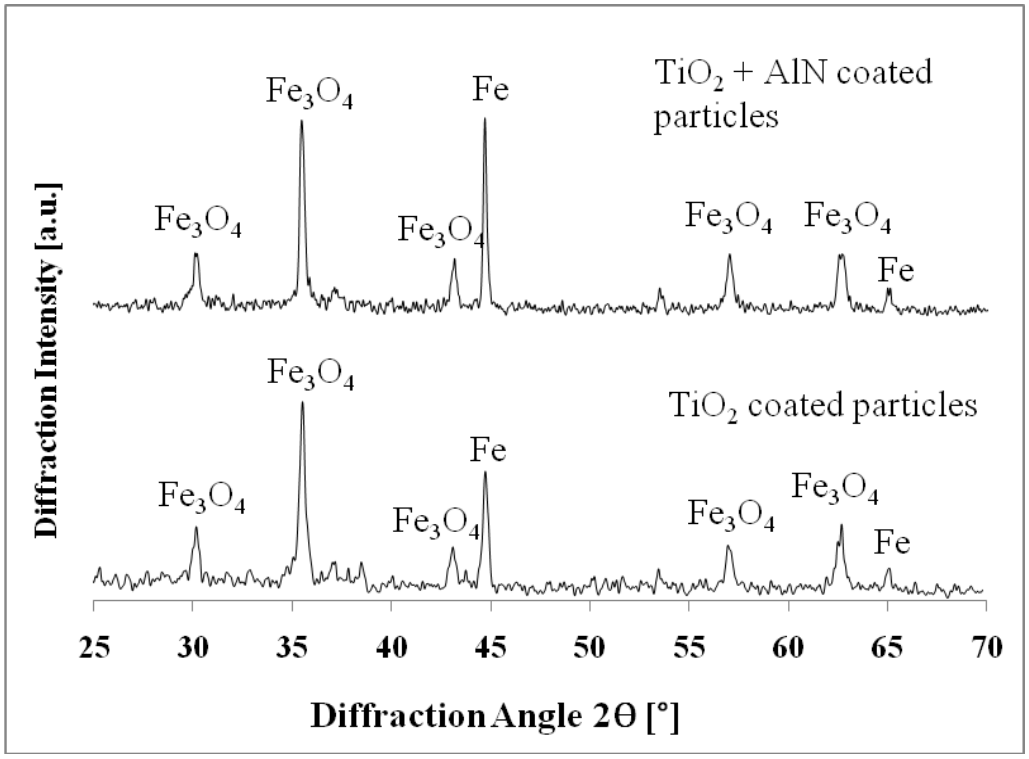

Figure 2.9 XRD spectra of AlN and TiO_2 bilayer films coated particles.

Figure 2.10 shows the magnetization versus field curves of the coated and uncoated particles. The three curves correspond to samples of uncoated particles derived from iron oxalate powder, the particles after 150 ALD cycles of TiO_2 deposition, and the particles after 100 AlN cycles plus 150 TiO_2 cycles coating. As the figure shows, the saturation magnetization of the

uncoated particles is higher than that of the other samples. For the TiO_2 coated powders, the reduction in saturation magnetization was significant, with the value down from 68.1 to 47.5 A m^2/kg because much more iron was oxidized to iron oxide in this sample. The measured magnetization was higher when the nitride interlayer film was used, relative to the TiO_2:Fe composite, up to 63.3 A m^2/kg. Theoretically, the thin films should not influence the magnetization of the core particles, other than requiring an adjustment to the sample mass. The fact that the TiO_2:AlN:Fe nanocomposite magnetization fell between the uncoated and the TiO_2 coated samples reflects a reduction in Fe_3O_4 thanks to the nitride layer. A thicker coating might provide more protection against oxidation.

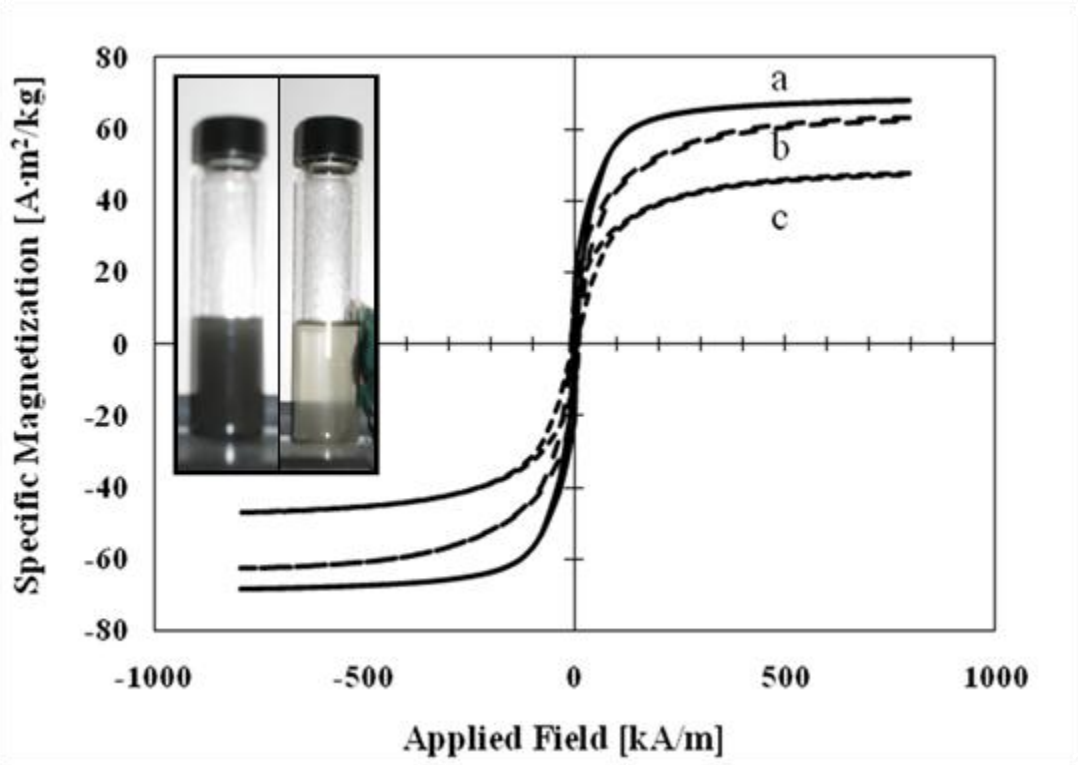

Figure 2.10 Specific magnetization curves, calculated as magnetic moment per unit mass of particles' core, of (a) uncoated particles, (b) AlN+TiO_2 coated particles, and (c) TiO_2 coated particles. The insert images were taken with (b) AlN+TiO_2 coated particles suspended in ethanol solution before and 2 minutes after a magnet was in close proximity.

The saturation magnetization of all these samples is lower than that of bulk iron and bulk magnetite. The uncoated particles likely contain an amount of Fe_3O_4 due to direct exposure to air between removing it from the reactor and measuring the magnetization. In addition, iron grain size can affect the magnetization of the powder. In general, the specific magnetic moment of nanoparticles is smaller than that of the bulk material and increases with increasing grain size [29]. Magnetic hysteresis is present, with coercive forces of 5 kA/m (60 Oe) for curve (a) and 10 kA/m (130 Oe) for curves (b) and (c). This indicates that the particles are ferromagnetic. Comparing to superparamagnetic particles, ferromagnetic particles have larger magnetic moments, multiple magnetic domains, and some cohesively, and may be superior for applications that require high saturation magnetization at low field levels.

In order to verify the actual separation effect of the magnetic photocatalyst, a qualitative demonstration was carried out. The TiO_2:AlN:Fe nanoparticles were evenly suspended in an ethanol solution in a glass vial, as shown in the left inset image in Figure 2.10. A magnet was put into close proximity of the vial. After two minutes, the solution became clear, as nearly all of the particles were separated from the bulk solution, which can be seen in the right inset image in Figure 2.10. Though qualitative, this demonstration validated the notion that the synthesized magnetic photocatalyst particles could be effectively removed from a bulk mixture under a magnetic field.

These current results confirm the assisted passivation effect the AlN film provided and demonstrate that the film itself hardly influences the magnetization of the composite particles. A more in depth study of nitride coatings on metal nanopowders could optimize this magnetic photocatalyst system. For general environmental applications, higher saturation magnetization is desirable due to the lower magnetic field required for recovery and consequently lower costs.

The photoactive property of the magnetic photocatalyst coated with the bilayer film was also investigated by decomposition of MB solution. The MB decomposition behavior was similar to that shown in Figure 2.5, suggesting that the internal AlN film does not change the photocatalytic activity of the composite particles. This is understandable since the photoactivity is attributed to the TiO_2 film, and the number of TiO_2 ALD cycles was the same for these two samples. Therefore, the functional magnetic photocatalyst can be synthesized from iron oxalate thermal decomposition followed by *in situ* TiO_2 ALD processing. In order to maintain the high magnetic moment, a protective thin film such as AlN, or other films without an oxidizing precursor, may be added prior to the TiO_2 ALD process. For the AlN passivation film, more than 100 ALD cycles are appropriate to protect the underlying iron from oxidation by the H_2O_2 precursor but 100 cycles appeared to be adequate here. If the same TiO_2 ALD precursors are used and higher magnetization is required, more cycles of AlN ALD would be required.

2.4 Conclusions

The synthesis of nanosized magnetic photocatalyst particles was presented here through the use of the particle ALD method. The overall method to produce passivated and functionalized magnetic photocatalyst particles included four steps. First, the particle size of the original feed iron oxalate particles was decreased by a milling process. It was repeatedly demonstrated in this paper that solvent-based cryogenic milling was highly efficient at breaking down powders and achieving small particle size distributions. Second, iron nanoparticles were synthesized by decomposing the milled iron oxalate powder at high temperature in a reducing gas environment. The subsequent step was to passivate the iron particles via an *in-situ* ALD method in the same FBR. By depositing a thin, oxygen-free protective film, such as AlN, iron

oxidation was significantly reduced. The final step involved the TiO_2 ALD films that provided the particles with the photocatalytic property. The photoactivity of these resulting particles was demonstrated by decomposing an MB solution. The specific magnetic property was verified with a magnetometer. Since the ALD technique is becoming more commercially mature, the overall magnetic photocatalyst synthesis method demonstrated in this work can potentially be applied to fabrication in industry. Furthermore, the application of this nanocomposite material for environmental treatment is promising.

2.5 References

1. Herrmann, J.M., Heterogeneous photocatalysis: State of the art and present applications. Topics in Catalysis, 2005. 34(1-4): p. 49-65.

2. Hashimoto, K., H. Irie, and A. Fujishima, TiO2 photocatalysis: A historical overview and future prospects. Japanese Journal of Applied Physics Part 1-Regular Papers Brief Communications & Review Papers, 2005. 44(12): p. 8269-8285.

3. Chen, X.B. and S.S. Mao, Synthesis of titanium dioxide (TiO2) nanomaterials. Journal of Nanoscience and Nanotechnology, 2006. 6(4): p. 906-925.

4. Hoffmann, M.R., et al., Environmental Applications of Semiconductor Photocatalysis. Chemical Reviews, 1995. 95(1): p. 69-96.

5. Ren, M.M., R. Ravikrishna, and K.T. Valsaraj, Photocatalytic degradation of gaseous organic species on photonic band-gap titania. Environmental Science & Technology, 2006. 40(22): p. 7029-7033.

6. Herrmann, J.M., Heterogenous photocatalysis: an emerging technology for water treatment. Catalysis Today, 1993. 17: p. 7-20.

7. Zhao, J. and X.D. Yang, Photocatalytic oxidation for indoor air purification: a literature review. Building and Environment, 2003. 38(5): p. 645-654.

8. Serrano, B. and H. deLasa, Photocatalytic degradation of water organic pollutants. Kinetic modeling and energy efficiency. Industrial & Engineering Chemistry Research, 1997. 36(11): p. 4705-4711.

9. Ngomsik, A.F., et al., Magnetic nano- and microparticles for metal removal and environmental applications: a review. Comptes Rendus Chimie, 2005. 8(6-7): p. 963-970.

10. Tsouris, C., et al., Surfactant effects on the mechanism of particle capture in high-gradient magnetic filtration. Separation and Purification Technology, 2006. 51(2): p. 201-209.

11. Farrell, D., S.A. Majetich, and J.P. Wilcoxon, Preparation and characterization of monodisperse Fe nanoparticles. Journal of Physical Chemistry B, 2003. 107(40): p. 11022-11030.

12. Tartaj, P., et al., The preparation of magnetic nanoparticles for applications in biomedicine. Journal of Physics D-Applied Physics, 2003. 36(13): p. R182-R197.

13. Hakim, L.F., et al., Synthesis of oxidation-resistant metal nanoparticles via atomic layer deposition. Nanotechnology, 2007. 18(34): p. -.

14. Aarik, J., et al., Atomic layer deposition of titanium dioxide from TiCl4 and H2O: investigation of growth mechanism. Applied Surface Science, 2001. 172(1-2): p. 148-158.

15. Cheng, H.E., C.M. Hsu, and Y.C. Chen, Substrate Materials and Deposition Temperature Dependent Growth Characteristics and Photocatalytic Properties of ALD TiO2 Films. Journal of the Electrochemical Society, 2009. 156(8): p. D275-D278.

16. Pore, V., et al., Atomic layer deposition of photocatalytic TiO2 thin films from titanium tetramethoxide and water. Chemical Vapor Deposition, 2004. 10(3): p. 143-148.

17. King, D.M., et al., Atomic layer deposition of TiO2 films on particles in a fluidized bed reactor. Powder Technology, 2008. 183(3): p. 356-363.

18. King, D.M., et al., In situ synthesis of TiO2-functionalized metal nanoparticles. Industrial & Engineering Chemistry Research, 2009. 48(1): p. 352-360.

19. Puurunen, R.L., Surface chemistry of atomic layer deposition: A case study for the trimethylaluminum/water process. Journal of Applied Physics, 2005. 97(12): p. -.

20. Witkin, D.B. and E.J. Lavernia, Synthesis and mechanical behavior of nanostructured materials via cryomilling. Progress in Materials Science, 2006. 51(1): p. 1-60.

21. Liang, X.H., et al., Alumina atomic layer deposition nanocoatings on primary diamond particles using a fluidized bed reactor. Diamond and Related Materials, 2008. 17(2): p. 185-189.

22. Puurunen, R.L., et al., Successive reactions of gaseous trimethylaluminium and ammonia on porous alumina. Physical Chemistry Chemical Physics, 2001. 3(6): p. 1093-1102.

23. Mayer, T.M., J.W. Rogers, and T.A. Michalske, Mechanism of Nucleation and Atomic Layer Growth of Aln on Si. Chemistry of Materials, 1991. 3(4): p. 641-646.

24. Bertolet, D.C. and J.W. Rogers, Mechanistics of Early Stage Growth of Aln on Alumina - Tmal and Nh3. Chemistry of Materials, 1993. 5(3): p. 391-395.

25. Puurunen, R.L.R., A.; Sarv, P.; et al, Growth of aluminium nitride on porous silica by atomic layer chemical vapour deposition. Applied Surface Science 2000. 165: p. 193-202.

26. Badylevich, M., et al., Electronic structure of the interface of aluminum nitride with Si(100). Journal of Applied Physics, 2008. 104(9):

27. Bartram, M.E., et al., Nucleation and Growth of Ain - Self-Limiting Reactions and the Regeneration of Active-Sites Using Sequential Exposures of Trimethylaluminum and Ammonia on Silica at 600 K. Chemistry of Materials, 1993. 5(10): p. 1424-1430.

28. Puurunen, R.L., et al., Growth of aluminum nitride on porous alumina and silica through separate saturated gas-solid reactions of trimethylaluminum and ammonia. Chemistry of Materials, 2002. 14(2): p. 720-729.

29. Qiang, Y., et al., Iron/iron oxide core-shell nanoclusters for biomedical applications. Journal of Nanoparticle Research, 2006. 8(3-4): p. 489-496.

CHAPTER 3

Optimal Preparation of Pt/TiO_2 Photocatalysts using Atomic Layer Deposition

Abstract

Platinum (Pt) was deposited on TiO_2 photocatalyst nanoparticles using atomic layer deposition (ALD) to increase the photocatalytic activity of TiO_2. Methylcyclopentadienyl-(trimethyl) Platinum(IV) ($MeCpPtMe_3$) and oxygen were used as precursors over a deposition temperature range of 150 - 400 ℃. The Pt ALD reaction mechanism was studied using an *in situ* mass spectrometer. The effect of operating temperature on Pt deposition was explored, and the resulting effect on TiO_2 photoactivity was measured. The lower temperature limit for Pt ALD was found to be approximately 200 ℃. Although the $MeCpPtMe_3$ chemisorption step occurred on the particle surfaces at 150 ℃, the ligand removal efficiency from the adsorbed Pt precursor was extremely low for O_2 dosing steps at temperatures below 200 ℃. Pt deposition via ALD resulted in a significant improvement in TiO_2 photoactivity. It was determined that one Pt ALD cycle carried out at 320°C was optimal to maximize Pt surface dispersion and increased the photoactivity of TiO_2 nanoparticles threefold.

3.1 Introduction

Although TiO_2 photocatalyst is extensively used for many environmental applications, the treatment efficiency is still not high enough for it to be used at a big scale. So the improvement of the TiO_2 photoactivity has emerged as a research subject of considerable

mportance and urgency. Surface modification by use of platinum is an effective method to increase the photoactivity of TiO_2 in the purification of contaminants from water [1-3].

Studies focusing on the methods to deposit Pt are important as they yield varying degrees of surface modification and subsequent catalytic efficiency. Traditional methods for depositing Pt include photo-deposition [4, 5], impregnation [6], vapor deposition [7] and chemical reduction of Pt salts [8]. However, these methods cannot accurately control the Pt deposition, especially when it is desirable to uniformly modify surfaces with small, highly dispersed Pt islands or clusters.

Atomic layer deposition (ALD) is a thin film growth technology providing precision control over both thickness and composition by sequential self-limiting surface reations. It is known the ALD technique cannot only deposit films but also islands when only early stages of ALD growth are applied [9-11]. Moreover, different deposition temperatures will lead to different island densities. Therefore, the loading and dispersion of Pt can be controlled by varying the number of ALD cycles and the deposition temperature. These powerful characteristics make ALD an attractive technology to produce both high-quality films and nanoparticles on the surfaces of flat or particulate substrates.

In this study, Pt was deposited on TiO_2 via the ALD technique using alternating exposures of Methylcyclopentadienyl-(trimethyl) Platinum(IV) ($MeCpPtMe_3$) and oxygen. This method was first reported by Aaltonen *et al*. in 2003 [12]. The growth mechanism of Pt ALD on particles is further investigated here using a mass spectrometer. Due to the high surface area of nanoparticle substrates, it is easier to achieve clear mass spectrometry data than when the ALD reaction is carried out on flat surfaces, as reported by Aaltonen *et al* [12]. This characteristic facilitates the ALD mechanism study. The influence of operating temperature during Pt ALD and

the low temperature limit for Pt coating are also explored. The number of ALD cycles and operating temperature are optimized in order to reduce the overall loading of this costly noble metal, while retaining the large improvement to the substrate photoactivity. First, the Pt ALD process is studied with respect to number of cycles on TiO_2 nanopowders at 400 ℃ and the resulting photoactivity is investigated. The photoactivity is also studied using a single cycle of Pt ALD over a range of deposition temperatures to understand the influence of ALD temperature on the photoactivity of TiO_2. A key objective of the research is to develop an efficient Pt/TiO_2 photocatalyst using ALD to minimize the Pt loading, yet maximize the Pt surface dispersion.

3.2 Experimental

3.2.1 Materials

Aeroxide P-25 titanium dioxide (Evonik), which is a well-known nanoparticle photocatalyst, was used as the substrate for the ALD experiments. The surface area of P-25 TiO_2 nanopowder is ~50 m^2 g^{-1} and is composed of sintered chains of ~20 nm primary particles. The crystal structure is about 70 % anatase and 30 % rutile. Methylene Blue (MB, $C_{16}H_{18}N_3S$) was purchased from Alfa Aesar and the Pt ALD precursor, $MeCpPtMe_3$, was purchased from Sigma-Aldrich.

3.2.2 Pt atomic layer deposition

The Pt nanoparticles were deposited on the surfaces of primary TiO_2 nanoparticles by ALD in a fluidized bed reactor (FBR). The FBR system consists of a reactor column, a vibration generation system, a gas flow control system, a mass spectrometer, and a rotary vane vacuum pump. Mechanical vibration was imparted to the reactor system in order to assist nanoparticle fluidization. The details of similar reactor configurations are described before [13, 14]. It has

been shown previously that nanoparticles fluidize as soft micron-sized agglomerates, and require the delivery of shear forces to break apart these dynamic clusters in order to expose the entire particle surface area to the ALD precursors [15]. A mass spectrometer (QMS200, Stanford Research Systems) was attached to the outlet of the reactor to monitor the progression of ALD half-reactions *in situ*.

During the Pt ALD process, the precursors $MeCpPtMe_3$ and O_2 were fed into the reactor sequentially, separated by critical purging steps. Since $MeCpPtMe_3$ is a solid precursor, an inert carrier gas (here, N_2) was used to carry the sublimed vapor into the reactor. The $MeCpPtMe_3$ precursor container and all of the lines leading into the reactor were maintained at 80 ℃ (using heating tape) in order to assist the sublimation of the solid $MeCpPtMe_3$ precursor and to prevent the precursor vapor from subsequently condensing before entering the reactor. For a typical run, 2.0 grams of TiO_2 substrate were loaded into the reactor. Gas flow velocities of around 0.8 cm/s were selected based on fluidization curves that characterized the pressure drop across the bed at various flow rates. This flow rate provided for an ALD operating pressure of about 6 Torr. After each precursor dose period, the reactor was purged with N_2 to remove residual unreacted precursors and/or reaction byproducts. The ALD reaction temperature ranged from 150 ℃ to 400 ℃. A set of screening experiments was performed over a range of ALD cycles at a deposition temperature of 400 ℃ to ensure that linear growth was attainable at the upper temperature. The dose and purge times were 200 sec/1200 sec and 600 sec/1500 sec for $MeCpPtMe_3$ and O_2, respectively. The ALD dose/purge sequencing, step transitions and data acquisition were automatically controlled using LabView® software (National Instruments, Austin, TX).

3.2.3 Catalyst Characterization

High resolution transmission electron microscopy (HRTEM) and scanning transmission electron microscopy (STEM) images were obtained using a JEOL 2010F 200 kV Schottky field emission TEM equipped with an Oxford detector unit for elemental analysis while imaging. The specific surface area of each powder type was measured using a BET surface area analyzer (Gemini V, Micromeritics) with N_2 as the adsorbate species. Inductively coupled plasma atomic emission spectroscopy (ICP-AES) was used to measure the deposited Pt content. The particles were digested in aqua regia solution with periodic agitation for ~24 hours to ensure complete dissolution. The dissolved Pt content, in parts per million, was measured using an Applied Research Laboratories ICP-AES 3410+. After the Pt ALD process, the carbon impurity levels were tested using a LECO carbon analyzer (C200, LECO) and the residual functional groups were analyzed using an FTIR spectrometer (750 Series II, Nicolet).

3.2.4 Photoactivity Testing

The decomposition kinetics of a methylene blue (MB) solution were used to evaluate the photoactivity of the TiO_2 nanopowder and the Pt-modified TiO_2. A UV/Vis spectrophotometer (Lambda 35, Perkin Elmer) was utilized to detect the absorbance at a wavelength of 664 nm, and to calculate the MB concentration after given time intervals using Beers Law. After the sample powders, typically 0.1 grams, were dispersed in MB solution, the solution was kept in the dark until a steady-state absorbance was measured. After this equilibration time, a 100W UV lamp (Mineralogical Research Co.) having a wavelength of 360 nm was positioned at a distance of 10 cm above the solution. The radiant flux of the UV light at the surface of the solution was measured to be 12 mW cm^{-2} using a Radiometer/Photometer (IL1400A, International Light).

Because the quality of dispersion of the particles in solution plays an important role in the MB decomposition process, the solution was stirred continuously throughout the entire test period. 2.5 mL samples were taken from the solution at 5 minutes intervals, using a syringe equipped with a polymer filter to remove the particles from the sample liquid. The photocatalytic activity of the test particles was evaluated based on the decrease in MB concentration with UV irradiation time.

3.3 Results and Discussion

3.3.1 Photoactivity test of different ALD cycles of Pt deposited on TiO_2 at 400 ℃

In order to study the effect that the amount of Pt has on TiO_2 photoactivity, the photocatalytic activity for different numbers of Pt ALD cycles (deposited on the TiO_2 photocatalyst) was investigated through the decomposition of an MB solution. Typically, the MB photocatalytic decomposition on the TiO_2 surface follows pseudo-first-order kinetics, $dC/dt = kC$, where k is the pseudo-first-order rate constant. After integration [$\ln(C/C_0) = kt$], k is obtained from the slope of a linear fit of experimental data, as shown in Figure 3.1a. The relative concentration of MB is plotted against the irradiation time of UV light, as shown in Figure 3.1. All of the samples shown in Figure 3.1 are TiO_2 P-25 powder coated with different cycles of Pt deposited at an operating temperature of 400 ℃. Uncoated TiO_2 powders were also tested as a reference. In Figure 3.1b, the MB conversion is plotted against Pt ALD cycles after 30 min of irradiation. The MB decomposition rate was inversely parabolic with respect to the number of cycles, and occured most rapidly using three ALD cycles. Beyond three cycles, corresponding to 1.6 wt% Pt, the rate decreased with a further increase in the number of Pt ALD cycles. This trend continued to the extent that the performance fell below that of the uncoated TiO_2 powder beyond

light Pt ALD cycles. The mechanism of this photoactivity increasing at begining and then reducing with the Pt loading will be discussed in chapter 5.

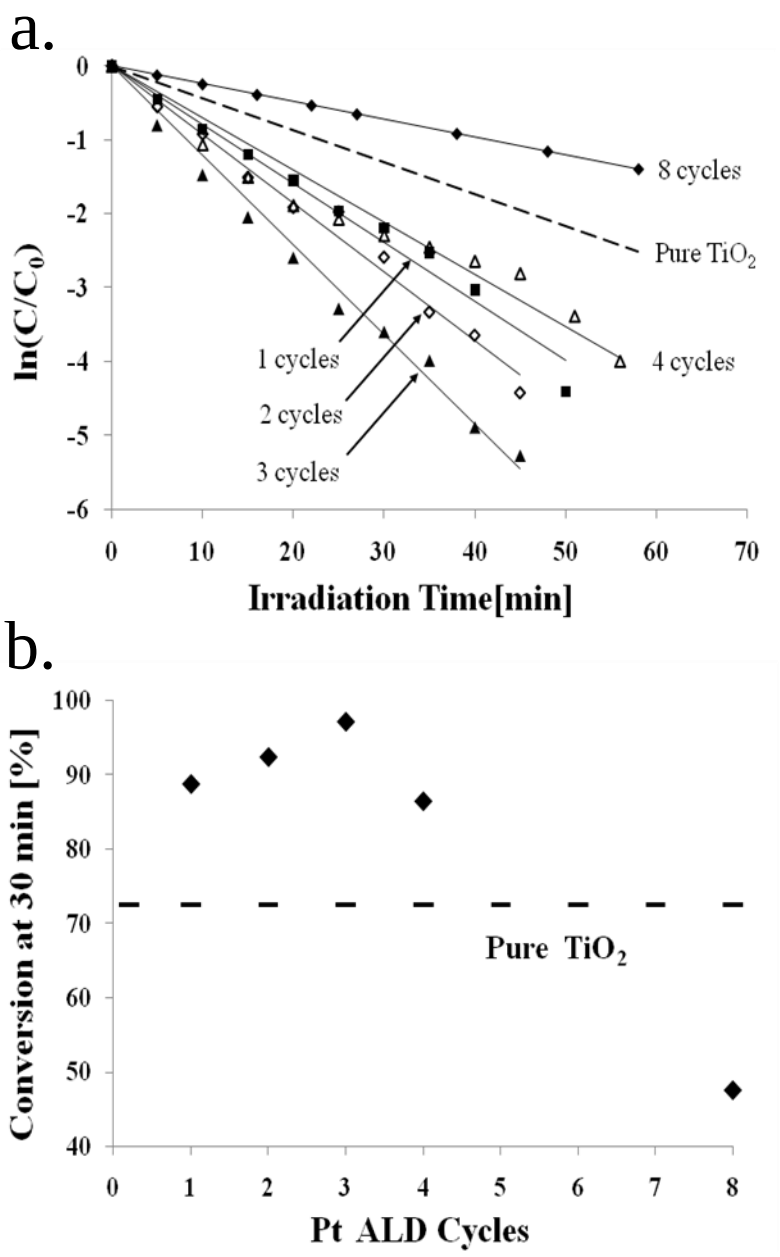

Figure 3.1 a) Relative concentration of MB vs. irradiation time for the samples of pure TiO_2 and different ALD cycles Pt doped TiO_2 at 400 ℃. b) MB conversion after 30 min irradiation vs. Pt ALD cycles for the samples of Pt doped TiO_2 at 400 ℃

The increase in the MB decomposition rate constant k from one to three cycles of Pt deposition can be explained by the increase in Pt content. ICP-AES analysis (Figure 3.2) shows that the Pt content measured increased linearly with the number of ALD coating cycles. Thermal decomposition of the metal-containing precursor can be problematic when coating high surface area particles due to the extended dose times required to saturate the surface area of powder in the fluidized bed. Thermal decomposition provides another route to surface deposition, but disrupts the self-limiting behavior inherent to ALD processes [16]. One method of detecting whether thermal decomposition occurs at a given operating temperature is to compare the deposited metal content after sub-saturating, saturating and super-saturating exposures of the precursor. An increase in metal content has been directly observed using *ex situ* techniques for the ZnO ALD process operated at or above the decomposition onset temperature of diethylzinc [17]. An *in situ*, yet somewhat qualitative, technique for detecting this phenomenon is to monitor the content of the effluent stream during a precursor dose. The decomposition byproducts can be observed after the ALD reaction product generation is complete for cases in which significant decomposition occurs. This was not observed during the Pt ALD process, although a small degree of thermal decomposition cannot be completely excluded. The dosing time was not varied at the higher temperature as this was not the primary purpose of this study. Of greater scientific interest is the prevention of Pt island coalescence, which is known to occur at higher temperatures. As such, lower-temperature studies using a single ALD cycle were the focus here. Maximizing surface dispersion of Pt via the ALD process is beneficial for all Pt-based catalysis reactions. The simplest method of maximizing the surface dispersion of a series of cycles is to maximize the surface dispersion of each individual cycle via deposition temperature. This is the first step to minimize the amount of Pt required to achieve a certain goal.

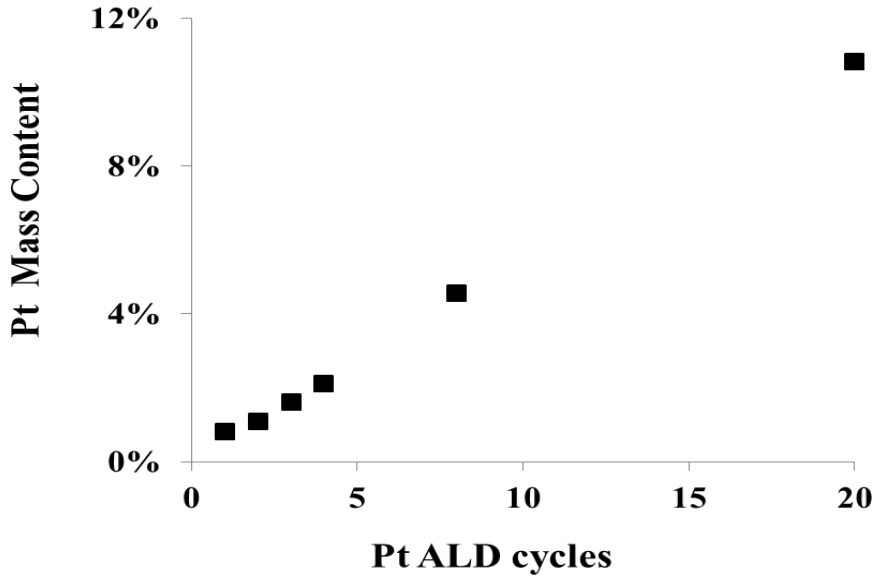

Figure 3.2 ICP-AES Pt content measured as a function of the number of coating cycles at deposition temperature 400 ℃

3.3.2 Reaction Chemistry of Pt ALD

Pt islands, or nanoclusters, were deposited on P-25 TiO_2 nanopowders using the ALD method in this study. The TEM and STEM images of Pt-coated TiO_2 powders are shown in Figure 3.3. The Pt islands shown in Figure 3a were deposited on TiO_2 using a single ALD cycle at a deposition temperature of 320 ℃. Images depicting a 20 cycle process at the same operating conditions are shown in Figures 3.3b and 3.3c. These images clearly show that Pt ALD follows the island nucleation mechanism during early-stage growth, even after 20 cycles. The Pt nanoclusters were evenly dispersed on the TiO_2 substrate powder, with the Pt partice size less then 1 nm after a single cycle and about 2-3 nm for the 20 cycle process. The Pt mass content for the samples in Figure 3.3a and Figure 3.3b was 0.64% and 10.08%, respectively. The BET surface area was also measured. For the samples in Figure 3.3a and Figure 3.3b, the surface area was 49.1 ±0.3 $m^2 g^{-1}$ and 51.7 ±0.2 $m^2 g^{-1}$, which is similar to that of uncoated TiO_2.

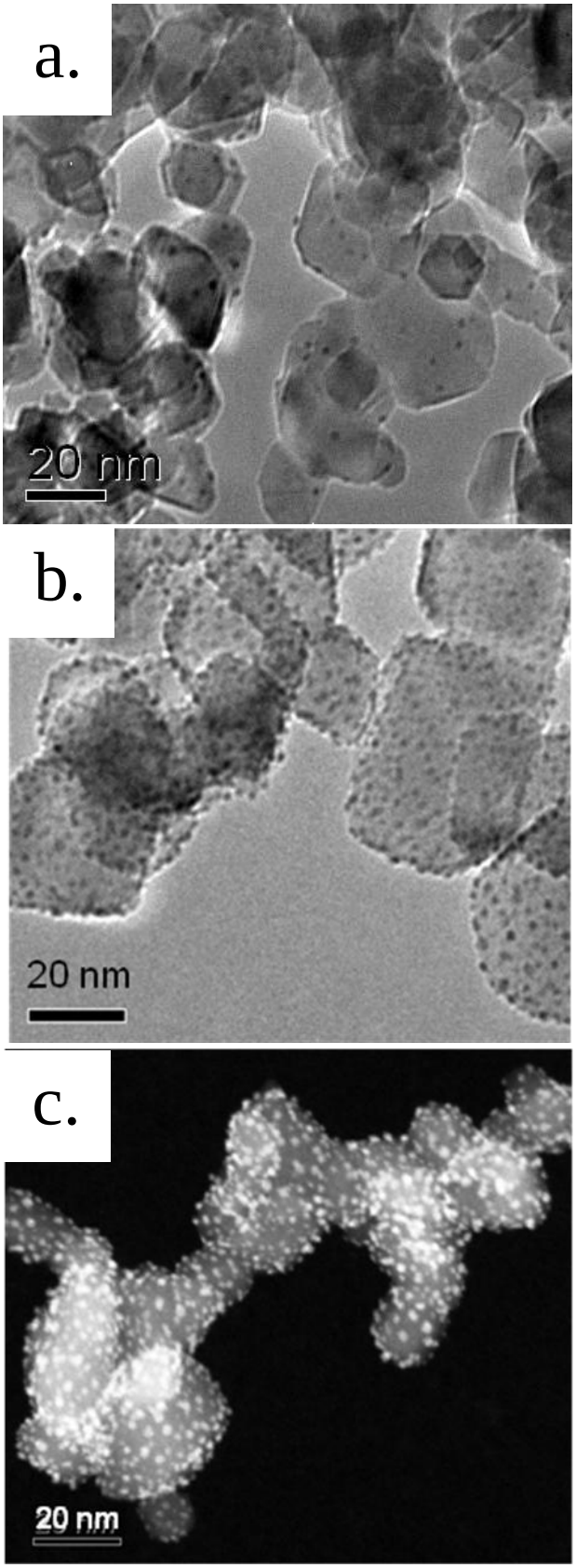

Figure 3.3 HRTEM images of Pt deposited TiO_2 powders at 320 ℃ after a) 1 cycle , b) 20 cycles ALD process, and c) STEM image of the same sample as b).

A range of Pt ALD temperatures from 150 ℃ to 400 ℃ was studied to understand the influence of temperature on the deposition and the resulting photoactivity of the Pt/TiO_2 composite powder. A mass spectrometer was used to observe the progression and termination of each ALD half reaction by analyzing a slip-stream of gas exiting the reactor. The mass spectrometry response for one representative ALD cycle at 320 ℃ is shown in Figure 3.4. The beginning and end of each half reaction was clearly observed, which indicated that the chemistry of Pt ALD was indeed self-limiting. During the Pt dose half reaction, as shown in Figure 3.4a, an instantaneous increase in the signal of CO_2 byproduct was observed. When the reaction was completed, the partial pressure of CO_2 decreased and the breakthrough of unreacted $MeCpPtMe_3$, represented by the 'A' reactant as shown in Figure 3.4a. We can conclude that the reaction was self-limiting, based on the observation that the reaction products first increased and then decreased while the reactants were still being dosed. If these reactions had not been self-limiting, the products would continue to be generated as long as the reactant dose was carried out. These measurements demonstrate that particle ALD in a fluidized bed can be operated in such a manner that no Pt precursor is wasted. This is an extremely beneficial attribute considering the high cost of Pt and other noble metal precursors. Therefore, the dosing step can be stopped after the reaction is completed in order to guarantee that no precursor is wasted. Additional precursor was administered here solely for experimentation purposes.

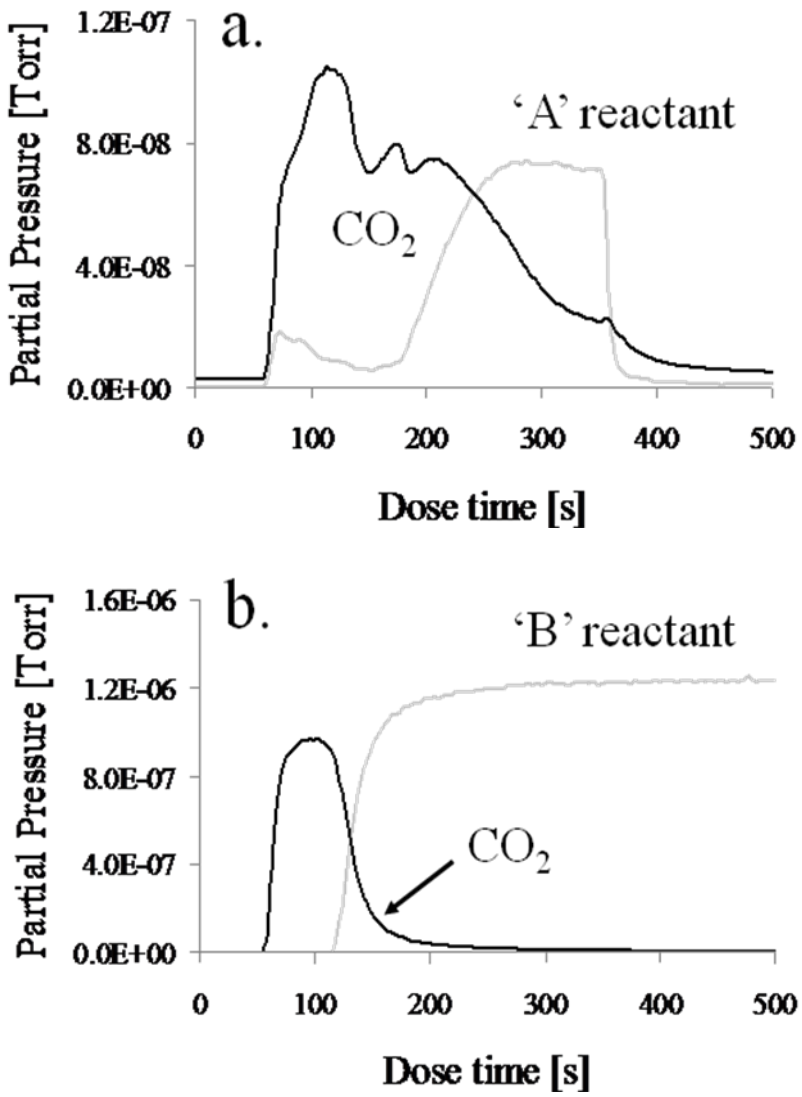

Figure 3.4 *In situ* mass spectrometry data of one Pt ALD cycle at 320 ℃, consisting of precursors $MeCpPtMe_3$ and O_2.

After the N_2 flush step to remove any remaining Pt precursors and byproducts, O_2 was dosed into the reactor. In this step, the same self-limiting behavior was observed. The partial pressure of byproduct CO_2 increased immediately as soon as the O_2 dose began. During the O_2 dose step, represented by the 'B' reactant in Figure 3.4b, oxygen was not observed until after a

lag time, indicating the complete uptake of the precursor. After the substrate surface was saturated, the CO_2 pressure decreased and the breakthrough of unreacted O_2 occurred, suggesting the reaction was nearly complete. For academic purposes, the oxygen was also overdosed. The concentration of CO_2 decreased despite the addition of extra O_2 in the reactor, confirming that the reaction was completed. In this half reaction, O_2 reacted with the remaining Pt precursor ligands to release CO_2 and other byproducts. Since the generated amount of CO_2 is large in comparison to that produced during the first half reaction, it is clear that the O_2 chemisorption is not the only reaction occuring during this period, as is suggested via equation (2). Instead, the reaction between $MeCpPtMe_3$ ligands and O_2 appears to take place during both dose periods.

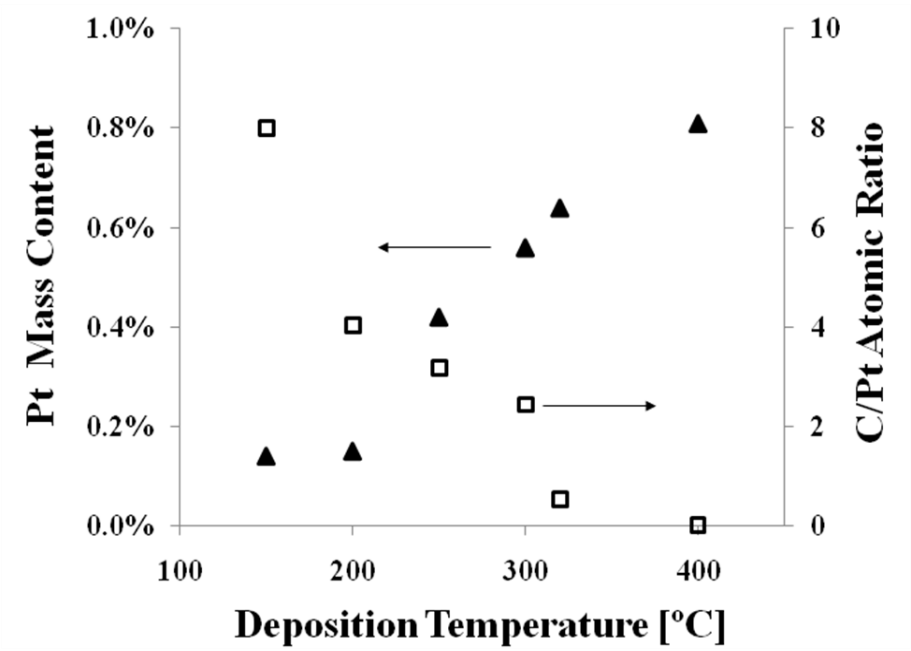

Figure 3.5 Pt content and carbon impurity on 1 cycle Pt coated TiO_2 nanoparticles measured as a function of the number of coating cycles

The mass spectrometry response for the Pt ALD reaction at other temperatures is similar to that at 320 ℃, except for the reaction at temperatures below 200 ℃. During the 150 ℃

deposition process, the O_2 pressure signal increased as soon as the dose step started. This signified that the O_2 was not reacted or not completely reacted at this low reaction temperature. On the other hand, at deposition temperatures at or above 200 ℃, the O_2 breakthrough was similar to that shown in Figure 3.4, although the breakthrough onset time was different for equivalent bed masses. At a lower deposition temperature, a shorter breakthrough time was observed. This behavior suggested that 200 ℃ is the low temperature limit for Pt ALD using $MeCpPtMe_3$ and O_2. This observation is in agreement with the report by Aaltonen et al [18]. Above 200 ℃ the growth rate increased with increasing temperature.

In order to verify the dependence of growth rate with temperature discussed above, the Pt content and carbon impurity on coated TiO_2 powders were measured after one cycle of Pt ALD at different coating temperatures (Figure 3.5). The Pt content was measured by ICP-AES. The analysis showed that the amount of deposited Pt increased with increasing temperature. It is consistent with the results observed from the mass spectrometer. At 200 ℃, the growth rate was much lower than that at 400 ℃, although some effect of thermal decomposition of $MeCpPtMe_3$ could not be completely excluded at 400 ℃. The weight percentage of Pt deposited at 150 ℃ was close to that deposited at 200 ℃, which seemed to indicate that the growth rates were similar at these two temperatures. However, the similar Pt content between these two only compares the chemisorption efficiency between the Pt precursor doses, and does not correspond to the reaction efficiency during the oxygen dose. The similar Pt content implies that the same number of ligands were present on the surfaces after each Pt dose. Based on the mass spectrometry data obtained for the 150 ℃ process, it was hypothesized that the oxygen was not efficiently removing the ligands at operating temperatures below 200 ℃.

To test this hypothesis, the carbon impurity was measured for each of the single cycle processes over the entire temperature range. Carbon content measured using a LECO carbon analyzer is expressed as the C/Pt atomic ratio as shown in Figure 3.5. The stoichiometric ratio of carbon to Pt in the full precursor, $CH_3C_5H_4Pt(CH_3)_3$ is C/Pt = 9, and the chemisorbed precursor can retain at most eight carbon atoms. The degree of carbon impurity was lower for the Pt/TiO_2 powder that was coated at higher temperatures. At 400 ℃, almost all of the carbon from the ligands was reacted away during the oxygen dose step. As the temperature was decreased, however, more unreacted carbon was left on the surface of substrate powders. When the temperature decreased from 200 ℃ to 150 ℃, the carbon impurity increased significantly, changing from 4 to 8 carbon atoms per deposited Pt atom. This implies that the ligands of the chemisorbed Pt precursors were essentially not oxidized during the oxygen dose at a deposition temperature of 150 ℃. Therefore, 200 ℃ was the low temperature limit for Pt ALD in this study.

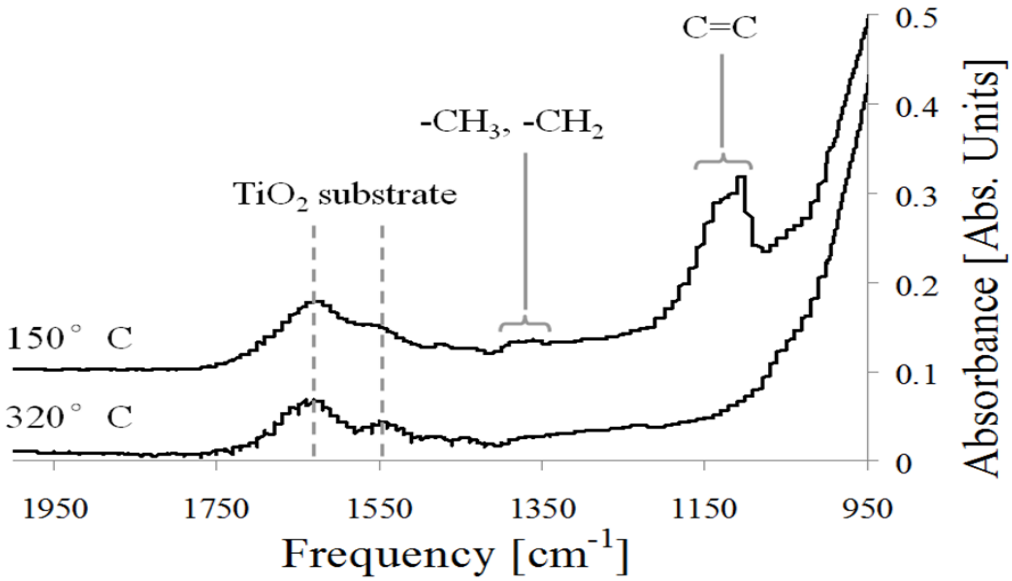

Figure 3.6 FTIR spectra of 1 cycle Pt coated TiO_2 nanoparticles at a) 150 ℃ and b) 320 ℃

the presence and composition of the residual precursor ligands. The FTIR difference spectra of the surfaces of TiO_2 nanoparticles after one cycle of Pt ALD at 150 ℃ and 320 ℃ is shown in Figure 3.6. The spectra have been shifted for visibility. A large absorbance is observed at 1100 cm^{-1} on the Pt/TiO_2 at 150 ℃ while not on the powder coated at 320 ℃. This is the expected range for double-bonded carbon stretching vibrations and is attributed to the cyclopentadienyl portion of the precursor ligand. In addition, the vibration feature at 1350-1400 cm^{-1} is likely due to the combination of $-CH_3$ and $-CH_2$ stretching vibrations from the ligands, which also only appeared on the Pt/TiO_2 powder deposited at 150 ℃. These differences are the direct confirmation for the presence of unreacted Pt precursors and carbon related ligands on the TiO_2 surfaces after one cycle Pt deposition at 150 ℃. For both samples, there are vibration features that appeared at the frequency centered around 1600 cm^{-1} and 1550 cm^{-1}, which are attributed to the TiO_2 substrate itself.

3.3.3 Photoactivity test of a single Pt ALD cycle deposited at different temperatures

In order to study the influence of deposition temperature on loading, surface dispersion and photoactivity of the Pt/TiO_2 photocatalyst, a single Pt ALD cycle was performed at various temperatures. The typical profile of the MB degradation behavior is shown in Figure 3.7. Similar to previous results, the data in Figure 3.7a suggest that an improved photoactivity effect was obtained when the Pt was deposited at or above 200 ℃. For the Pt/TiO_2 sample deposited at 150 ℃, however, the MB photodecomposition behavior was significantly different (Figure 3.7a). No continuous photocatalytic activity was observed beyond five minutes of irradiation.

Based on the hypothesis that the oxygen could not react away the precursor ligands at a temperature of 150 ℃, the remaining organic ligands absorbed on the Pt nanoclusters are the

most likely reason why the MB decomposition reaction shut off. The FTIR spectra shown in Figure 3.6 support this notion, as a much larger organic composition was observed on the Pt/TiO_2 deposited at 150 ℃ than that at 320 ℃. In order to verify this hypothesis, only the first half-cycle of Pt ALD on TiO_2 was performed at 200 ℃. In other words, only the Pt precursor was dosed and the O_2 dose was not performed. The comparison of the MB decomposition behavior for one full cycle and half cycle Pt deposited TiO_2 at 200 ℃ is shown in Figure 3.8. For the half cycle of Pt deposited at 200 ℃, the same behavior was observed as for the full cycle of Pt deposited at 150 ℃. After five minutes of irradiation, no further MB decomposition was observed. This was not the case for the sample of full Pt ALD cycle deposited on TiO_2 at 200 ℃, as shown in Figure 3.8b. This result clearly demonstrated that the unreacted Pt precursor ligands on the particle surface were the cause for the apparent photocatalyst deactivation in the low temperature case.

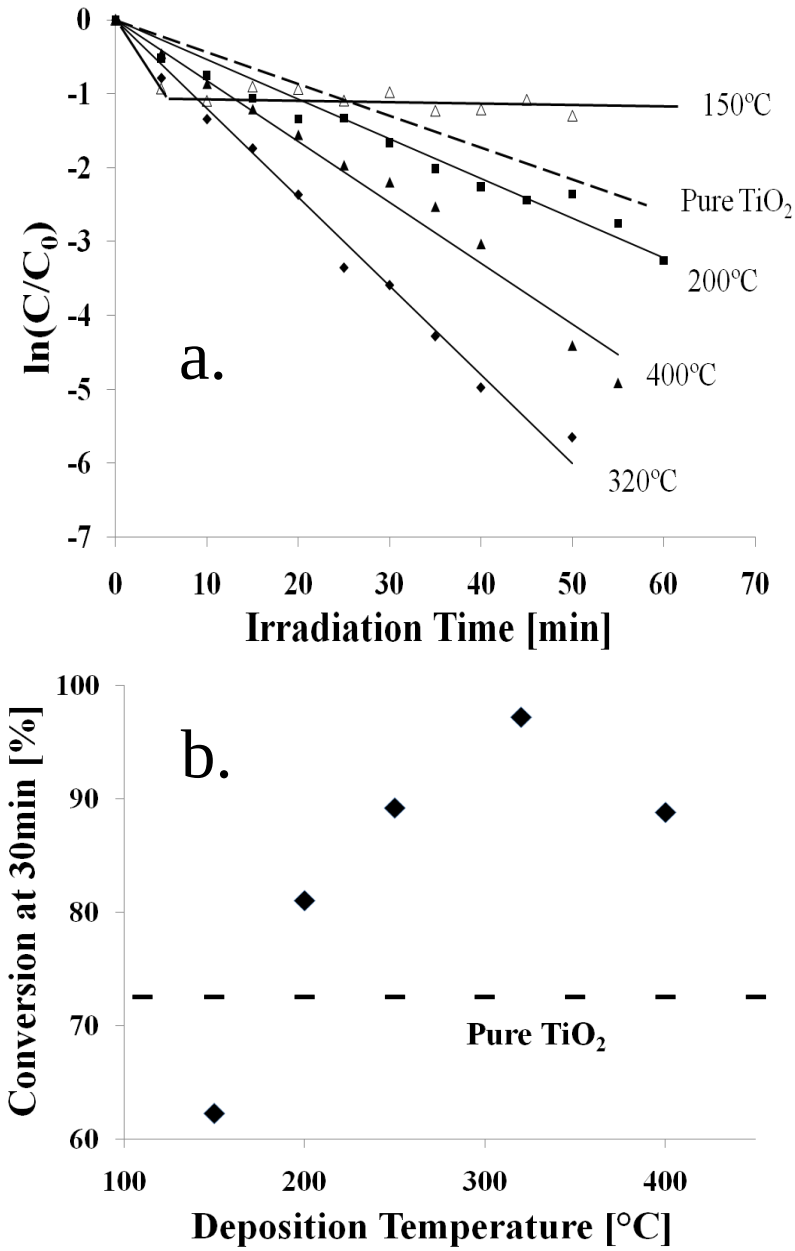

Figure 3.7 a) Relative concentration of MB vs. irradiation time for the samples of pure TiO_2 and Pt doped TiO_2 at different temperatures. b) MB conversion after 30 min irradiation vs. Pt deposition temperatures for the samples of Pt doped TiO_2.

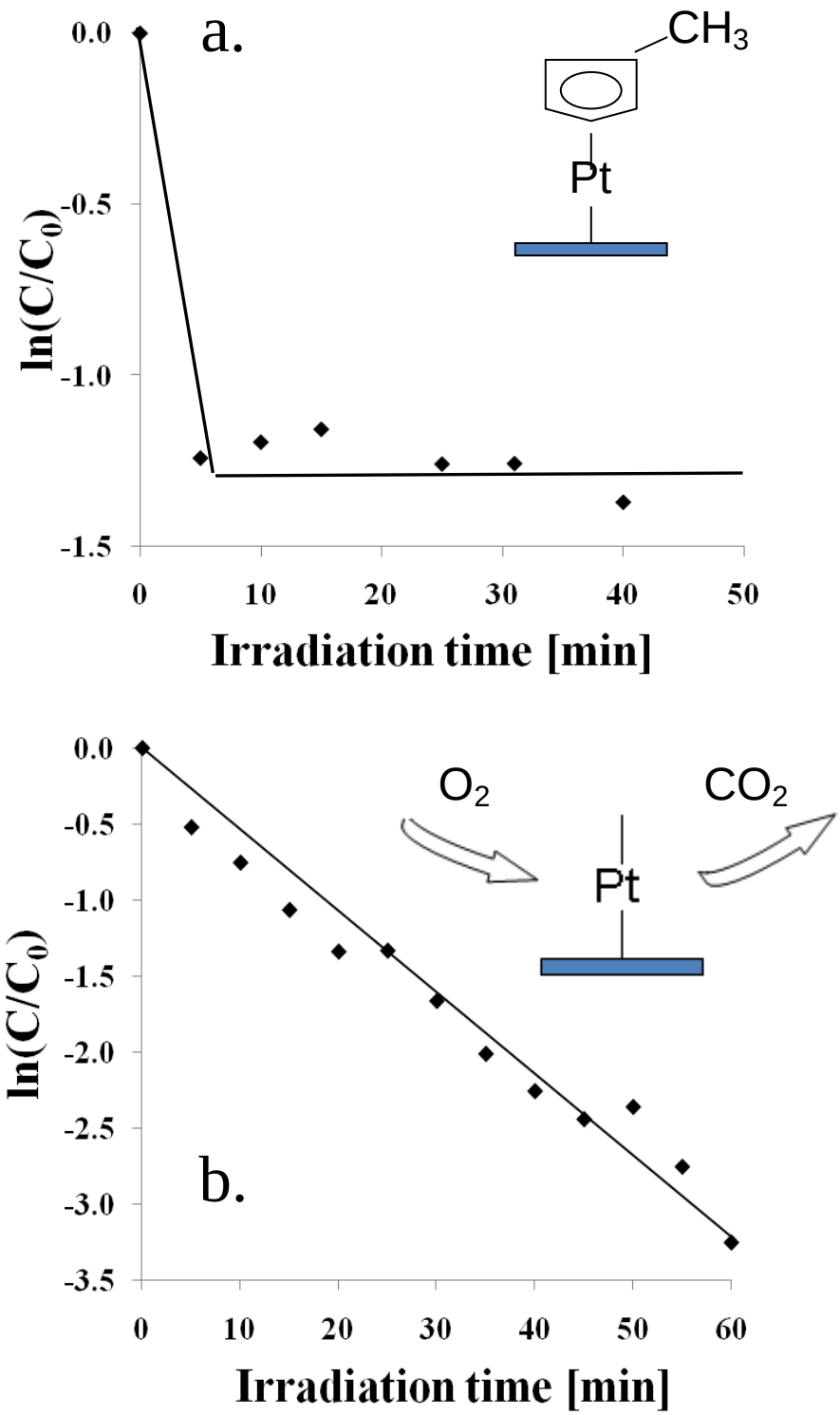

Figure 3.8 Relative concentration of MB vs. irradiation time for the samples a) half cycle and b) 1 full cycle Pt doped TiO_2 at 200 ℃

As represented by the slope of the linear relation (k value) in Figure 3.7a, when the Pt deposition temperature was above 200 ℃, the MB photodecomposition rates proceeded faster than that of pure uncoated TiO_2 and increased with increasing deposition temperature. At 320 ℃, the maximum decomposition rate was achieved, which then decreased for the Pt deposited at 400 ℃. In Figure 3.7b, the MB conversion after 30 min irradiation is plotted against Pt deposition temperature for one cycle of Pt coated TiO_2 samples. Based on the maximum in the photocatalytic activity curve, this suggests that 320 ℃ is the optimal deposition temperature to achieve the greatest improvement to the photoactivity of TiO_2 powders using the Pt ALD process.

The lower photocatalytic activity for coating temperatures below 320 ℃ is possibly due to lower Pt coverage and incomplete ALD reaction, as shown in Figure 3.5. For coating temperatures at 400 ℃, the ALD reactions were complete with even more Pt produced. However, the photoactivity test indicated that when the Pt was deposited using the ALD technique at 320 ℃, the activity exceeded that of the 400 ℃ sample. This is most likely caused by the formation of small and evenly dispersed Pt particles at 320 ℃, which may coalesce and form larger particles with a wider size distribution at 400 ℃. As shown in Figure 3.9, the Pt deposition carried out at 320 ℃ yielded a better dispersion and with smaller particle size than when Pt was deposited at 400 ℃. Because of higher mobility at higher temperature, the Pt dynamic coalescence is enhanced and therefore the probability for small islands to be incorporated into larger islands increases.

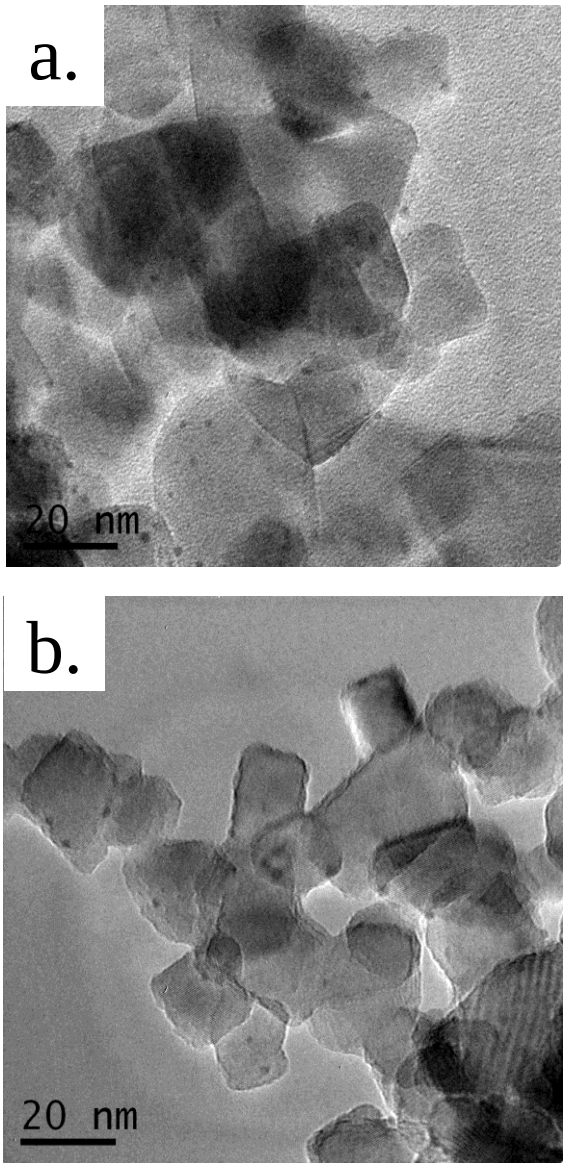

Figure 3.9 HRTEM images of 1 ALD cycle Pt deposited TiO_2 powders at a) 320 ℃ and b) 400 ℃

Figure 3.1 showed that when the ALD operating temprature was 400 ℃, three cycles of Pt ALD provided the best TiO_2 photocatalytic activity. Comparing the photoactivity of the single-cycle Pt/TiO_2 deposited at 320 ℃, which possessed the maximum photocatalytic activtity

for all of the single-cycle Pt/TiO_2 deposited at different temperatures, the photoactivity of these two samples is indentical, as shown in Figure 3.10. Both samples improved the photoactivity of pure TiO_2 threefold, as shown by the rate constant k. However, the Pt content for one cycle at 320 ℃ was 0.64 wt% , whereas three Pt cycles at 400 ℃ resulted in a Pt loading of 1.62 wt%. For equivalent activity, the deposition temperature optimization processes studied here provides for a 60% reduction in Pt loading, which translates directly into a 60% reduction in catalyst cost. Therefore, the strategy of coating one cycle of Pt ALD at 320 ℃ is the most efficient and economical method to improve the photocatalytic perfomance of TiO_2.

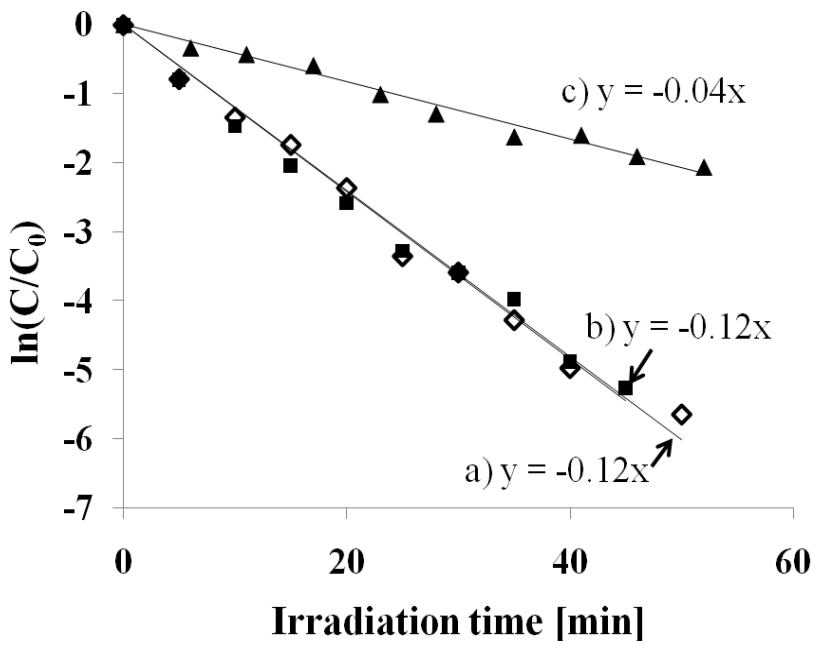

Figure 3.10 Photoactivity comparison of samples a) 1 cycle Pt/TiO_2 deposited at 320 ℃, b) 3 cycles Pt/TiO_2 deposited at 400 ℃ and c) Pure TiO_2 nanopowders

3.4 Conclusions

The work reported here indicates that ALD is an excellent method to deposit Pt nanoclusters on the surfaces of primary nanopowders. The Pt islands were nanosized and retained a high level of dispersion. The island growth mechanism of Pt ALD provides the possibility for efficient control of Pt loading. The effect of operating temperature was investigated by studying ALD precursor surface reaction efficiency, Pt deposition rate, and the resulting carbon impurity levels, along with the variation in photocatalytic activity. When the temperature was below 200 ℃, the low temperature limit for Pt ALD, the $MeCpPtMe_3$ precursor ligands were not removed by the subsequent O_2 dosing. The result was that no MB decomposition was observed beyond five minutes of UV light irradiation. When the deposition temperature was at or above 200 ℃, however, all of the single-cycle Pt/TiO_2 samples exhibited significantly higher photoactivity than that of uncoated TiO_2. The highest methylene blue decomposition rate was achieved at 320 ℃. This study also showed that the sample consisting of a single cycle of Pt deposited at 320 ℃, improved the TiO_2 photocatalytic activity more efficiently per unit mass than when three cycles of Pt were deposited at 400 ℃. This efficiency corresponded to a 60% reduction in Pt content for equivalent photoactivity. The Pt ALD method demonstrated in this work can be potentially used for the facile fabrication of TiO_2 photocatalyst particles loaded with highly dispersed islands of Pt, resulting in a threefold improvement in photoactivity under optimized deposition conditions.

3.5 References

1. Cho, K.C., et al., Photocatalytic performance of Pt-loaded TiO2 in the decomposition of gaseous ozone. Journal of Photochemistry and Photobiology a-Chemistry, 2004. 161(2-3): p. 155-161.

2. Sano, T., et al., Photocatalytic degradation of gaseous acetaldehyde on TiO2 with photodeposited metals and metal oxides. Journal of Photochemistry and Photobiology a-Chemistry, 2003. 160(1-2): p. 93-98.

3. Sivalingam, G., et al., Photocatalytic degradation of various dyes by combustion synthesized nano anatase TiO2. Applied Catalysis B-Environmental, 2003. 45(1): p. 23-38.

4. Ishitani, O., et al., Photocatalytic Reduction of Carbon-Dioxide to Methane and Acetic-Acid by an Aqueous Suspension of Metal-Deposited Tio2. Journal of Photochemistry and Photobiology a-Chemistry, 1993. 72(3): p. 269-271.

5. Yamakata, A., T. Ishibashi, and H. Onishi, Water- and oxygen-induced decay kinetics of photogenerated electrons in TiO2 and Pt/TiO2: A time-resolved infrared absorption study. Journal of Physical Chemistry B, 2001. 105(30): p. 7258-7262.

6. Kryukova, G.N., et al., Structural peculiarities of TiO2 and Pt/TiO2 catalysts for the photocatalytic oxidation of aqueous solution of Acid Orange 7 Dye upon ultraviolet light. Applied Catalysis B-Environmental, 2007. 71(3-4): p. 169-176.

7. Hiehata, K., A. Sasahara, and H. Onishi, Local work function analysis of Pt/TiO2 photocatalyst by a Kelvin probe force microscope. Nanotechnology, 2007. 18(8): p. -.

8. Mills, A.a.L., SK, Platinum group metals and their oxides in semiconductor photosensitisation. Platinum metals review, 2003. 47(1): p. 2-12.

9. Christensen, S.T., et al., Nanoscale Structure and Morphology of Atomic Layer Deposition Platinum on SrTiO3 (001). Chemistry of Materials, 2009. 21(3): p. 516-521.

10. Hoover, R.R. and Y.V. Tolmachev, Electrochemical Properties of Pt Coatings on Ni Prepared by Atomic Layer Deposition. Journal of the Electrochemical Society, 2009. 156(1): p. A37-A43.

11. King, J.S., et al., Ultralow loading Pt nanocatalysts prepared by atomic layer deposition on carbon aerogels. Nano Letters, 2008. 8(8): p. 2405-2409.

12. Aaltonen, T., et al., Atomic layer deposition of platinum thin films. Chemistry of Materials, 2003. 15(9): p. 1924-1928.

13. King, D.M., et al., Atomic layer deposition on particles using a fluidized bed reactor with in situ mass spectrometry. Surface & Coatings Technology, 2007. 201(22-23): p. 9163-9171.

14. Liang, X.H., et al., Novel processing to produce polymer/ceramic nanocomposites by atomic layer deposition. Journal of the American Ceramic Society, 2007. 90(1): p. 57-63.

15. Hakim, L.F., et al., Aggregation behavior of nanoparticles in fluidized beds. Powder Technology, 2005. 160(3): p. 149-160.

16. King, D.M., et al., Low-temperature atomic layer deposition of ZnO films on particles in a fluidized bed reactor. Thin Solid Films, 2008. 516(23): p. 8517-8523.

17. King, D.M., et al., Atomic layer deposition of UV-absorbing ZnO films on SiO2 and TiO2 nanoparticles using a fluidized bed reactor. Advanced Functional Materials, 2008. 18(4): p. 607-615.

18. Aaltonen, T., et al., Atomic layer deposition of noble metals: Exploration of the low limit of the deposition temperature. Journal of Materials Research, 2004. 19(11): p. 3353-3358.

CHAPTER 4

First-principles Study of the Pt Particle Growth on the Anatase TiO_2 (101) Surface

Abstract

The absorption properties of Pt_n (n is up to 37) clusters on defect free TiO_2 anatase (101) surfaces have been studied using *ab initio* pseudopotential calculations based on density functional theory. Several different initial configurations were relaxed and the most stable structures were established. All final optimized structures are three-dimensional, suggesting that Pt energetically prefers the formation of island-like particles rather than planar monolayers, which was verified by experimental Pt atomic layer deposition (ALD). Large size Pt particles are thermodynamically favorable for Pt growth as indicated by the clustering energy upon the adsorption decreasing with increasing Pt particle size. When the particle size approaches infinity, the clustering energy approaches a limit of the cohesive energy of bulk Pt (-6.03 eV). The diffusion of a single Pt adatom was investigated using the CI-NEB method to understand the Pt mobility over the TiO_2 surface. Migration pathways along the [010] and $[10\bar{1}]$ directions were calculated and the activation barriers are 0.86 eV and 1.41 eV respectively. The large barriers suggest the Pt atoms can be trapped at certain surface sites and the sintering process is slow at room temperature. Among the two directions, the diffusion barrier along the [010] direction is lower than that of the $[10\bar{1}]$ direction, indicating that the migration along the surface bridge oxygen row ([101] direction) is the prevalent migration direction during the Pt growth and ripening process at elevated temperature. The adsorption/desorption energy barrier for a Pt atom

attaching/detaching from a Pt cluster was also calculated and the desorption barrier was found to be very large (2.12 eV) suggesting the Pt Ostwald ripening process is interface transfer limited. The high desorption barrier would be responsible for the presence of a large number of small particles during the Pt ALD growth.

4.1 Introduction

Heterogeneous catalysis is a highly intensive research area because of its impact and widespread applications in chemical manufacturing, power generation, pollution control, and green chemistry [1-5]. Nanostructured metallic particles supported on metal oxide substrates are of great interest due to their importance in heterogeneous catalysis. The nature of the metal particle's structure, interactions with oxide support and the metal sintering behavior are critical to its catalytic activity. Understanding the properties of metal growth and diffusion is therefore important so as to tailor the oxide-metal particle system to achieve desired reactivity performance.

Of various heterogeneous catalysts, Pt receives significant attention. For example, Pt is a major component in current automobile three-way catalysts to oxidize CO and residual hydrocarbons [6, 7]; Pt is the most important catalyst used for the hydrogenation of ethylene and hydrogenolysis of ethane [8, 9]; Pt is one of the best catalysts for the oxidation and reduction reactions in fuel cells [10, 11], and for many other uses. One of the keys to optimize the effectiveness of Pt is to control the size and dispersion of Pt particles. Atomic layer deposition (ALD) is a method that has attracted a great deal of interest recently to deposit Pt nanoparticles with small size and high dispersion [12-17]. King et al demonstrated that Pt nanocatalysts prepared by the ALD method on carbon aerogel exhibit high catalytic activity for the oxidation

of CO [14]. Zhou et al revealed that only 1 ALD cycle of Pt nanoparticles deposited on TiO_2 powders increased the photoactivity of TiO_2 by threefold for the photo-decomposition of methylene blue [15]. In general, ALD is a thin film deposition method which deposits uniform, conformal and pinhole-free films with angstrom thickness control by an ABAB reaction pattern. However, unlike typical ALD processes, Pt ALD produces a dispersion of Pt nanoparticles, instead of thin films, even after tens or hundreds of cycles [18, 19]. Although Pt ALD has been successfully used to deposit Pt particles for various applications [11, 14, 15, 17], the cause of the different growth mechanism of Pt ALD remains unclear.

The relative complexity of experimental characterization of Pt nanoparticle growth renders the experimental study difficult. Theoretical study becomes an important tool for the interpretation of experimental results and to furnish new insights for experiments. This approach allows one to fundamentally study properties of interest directly. Therefore the Pt cluster growth and diffusion behavior were investigated in this study by quantum chemical simulation based on the density functional theory (DFT) method.

TiO_2 was selected as the substrate support here as it is one of most widespread supports in heterogeneous catalysis, such as, TiO_2 supported Au catalyst for CO oxidation [20] and TiO_2 supported Pt catalyst in direct methanol fuel cells for methanol electro-oxidation [21]. In addition, TiO_2 itself is a good photocatalyst which can degrade a wide range of pollutants in solution or air and the Pt deposition has been demonstrated to improve the photoactivity of TiO_2 [15, 22, 23]. The Pt/TiO_2 has also been reported to be effective for water splitting [24] and cancer cell treatment [25]. TiO_2 crystallizes in three different phases: rutile, anatase, and brooktie. Rutile is the most thermodynamically stable bulk phase but anatase is technologically more important than rutile. It is well known that the anatase surface has the highest photocatalytic activity among

the three crystal phases [26, 27]. Fujimoto et al also revealed high-speed resistive change in a resistance-switching random access memory (ReRAM) cell with an anatase monolayer[28]. So the anatase phase was the support structure here and the anatase (101) face was selected as it is the most stable and abundant anatase surface [29, 30].

Several researchers have investigated the interaction of Pt particles with TiO_2 anatase surfaces [30, 31], however, they only studied the Pt monomer, dimer and trimer on the TiO_2 surface. In this study, several different Pt_n particles with n up to 37 atoms were optimized and the most stable configurations were identified. Calculations have also been carried out to estimate the energy barrier corresponding to the diffusion of Pt atoms over the anatase surface, leading to an understanding of the mechanism of Pt particle growth and ripening. The diffusion behavior of single Pt adatom has been studied on different oxide surfaces, such as γ-Al_2O_3 surfaces[32] and CeO2 surface [33] , however, no reports related to Pt diffusion studies on TiO_2 surfaces have been published. This present study explores the Pt metal growth and diffusion behaviors on TiO_2, which are essential for understanding the Pt growth and the applications of Pt/TiO_2 composite material, and provides insights for other studies related to transition metal ALD growth and heterogeneous catalysis.

4.2 Computational and Experimental Methods

4.2.1 Computational Details

All calculations employed the plane wave approach to periodic boundary condition DFT simulations using the Vienna Ab initio Simulation Program (VASP) [34, 35]. DFT calculations were performed using the Perdew-Burke-Ernzerhof (PBE) generalized gradient approximation (GGA) exchange-correlation functional [36] coupled with the projector augmented wave (PAW)

pseudopotentials[37, 38]. PAWs treat O 2s and 2p; Ti 3p, 4s and 3d; and Pt 6s and 5d electrons explicitly. A cut off energy study was conducted in the range of 200 to 500 eV and a cutoff energy of 400 eV was determined to be sufficient. Consequently, all calculations utilize a cut off energy of 400 eV. Calculations were confined to the Γ point in all calculations as the Γ point accurately spans the k-space for large unit cells. Increasing the k-point grid to 2x2x2 had no appreciable effect on our results, confirming that the Γ point was sufficient for the relatively large unit cells employed in this study.

A 4×2 supercell slab consisting of 144 atoms was utilized in this study to represent the anatase TiO_2 (101) surface. The perfect anatase TiO_2 (101) slab was first relaxed and the structures are shown in Figure 4.1a and 4.1b. The (101) anatase surface has a stepped structure with coordinatively unsaturated ions. The surface consists of Ti atoms with two different coordinations: a 5-fold-coordinated Ti (5f-Ti) located further into the vacuum; and a 6-fold (fully) coordinated Ti (6f-Ti) located just below the surface; and three different O atoms: a 2-fold-coordinated bridging position O (2f -O) located furthest into the vacuum, and two different 3-fold coordinated ions, 3f-O, and 3f'-O, which differ mainly in the extent to which they extend into the vacuum. This relaxation pattern is in agreement with previous report [30, 31]

All slabs used were two Ti-O double layers deep to ensure the cell size that is computationally tractable. Slabs up to 5 double layers of TiO_2 were constructed and the slab with two double layers was found to give similar Pt and TiO_2 characteristics, both electronic and geometric, as that of the slab of 5 double layers; therefore, a two double layer slab was chosen to diminish computational costs. All cells had at least 15 Å of vacuum between the adsorbed species and the backside of the periodic image. The active side of the slab was allowed to relax,

while the atoms of the bottom layer for all cells were frozen in their bulk positions to mimic bulk-like properties. Geometry relaxations were carried out using the quasi-Newton-Raphson method to at least 1 X 10^{-3} eV. Bader charge analysis was conducted using software from the Henkelman group [39, 40].

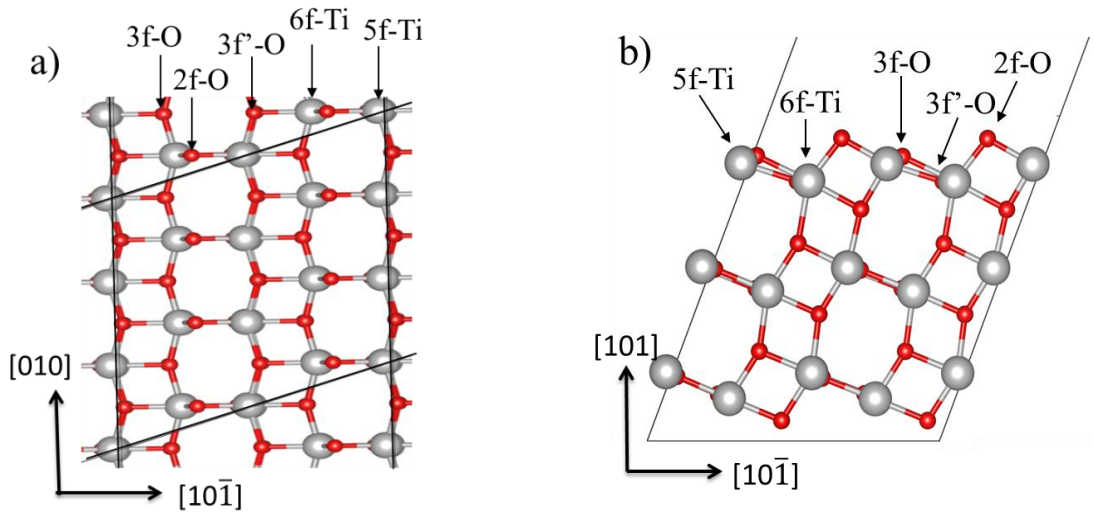

Figure 4.1 a) Top view of the perfect TiO_2 surface b) side view of the perfect TiO_2 surface. Large gray atoms are Ti, medium red atoms are oxygen. If viewing in black and white, large light atoms and small dark atoms represent Ti and O, respectively.

The Climbing Image Nudged Elastic Band method (CI-NEB) [41] was utilized to calculate activation barriers for the diffusion of a single Pt adatom. CI-NEB is developed from the Nudged Elastic Band method (NEB) [42]. NEB finds the activation barrier by taking several images along a path that connect an initial state to a final state and allows the geometries of the images to relax perpendicular to the tangent of the line that connects one image to the next. Additionally, springs are added between the images to keep the images evenly spaced. CI-NEB utilizes the same idea and method, but disconnects the image with the highest energy from the springs. This image is then pushed up hill in energy parallel to the tangent connecting the highest

energy image with the previous and the subsequent image. In this manner, the saddle point is more accurately found. In this study, at least 7 images (including the initial and final images) were calculated for each hop step from initial site to final or metastable site. The CI-NEB method code is from the Henkelman group.

The average cohesive energy for Pt_n cluster in gas was estimated from the following equation:

$$E_{Pt_n}^{coh} = E_{Pt_n} / n - E_{Pt} \qquad (1)$$

where E_{Pt_n} is the total energy of the Pt_n cluster in the gas phase, and E_{Pt} is the total energy of a single Pt atom. Similarly, clustering energy of the adsorbed Pt_n cluster on a TiO_2 surface was defined as:

$$E_{Pt_n/TiO_2}^{clu} = (E_{Pt_n/TiO_2} - E_{TiO_2} - nE_{Pt}) / n \qquad (2)$$

where E_{Pt_n/TiO_2} is the total energy of the Pt_n cluster on TiO_2 surface and E_{TiO_2} is the total energy of the bare TiO_2 slab.

4.2.2 Experimental methods

Pt clusters were deposited on the surfaces of TiO_2 P25 nanoparticles by ALD in a fluidized bed reactor. Methylcyclopentadienyl-(trimethyl) Platinum(IV) ($MeCpPtMe_3$) and oxygen were used as the precursors. One cycle of the ALD process is comprised of four steps: (1) dosing $MeCpPtMe_3$ precursor into the reactor, (2) purging or evacuating the chamber using an N_2 sweep gas to remove extra unreacted precursor and gaseous by-products, (3) dosing O_2 to remove the organic ligands of the Pt precursors and leaving Pt on the TiO_2 surface, (4) purging the chamber using N_2 to remove extra unreacted precursor O_2 and gaseous by-products. After

the deposition, a high resolution transmission electronic microscope (HRTEM) was utilized to study the surface geometry of different numbers of ALD cycles of Pt deposited on TiO_2 particles.

4.3 Results and Discussion

4.3.1 Pt_n clusters on TiO_2

Pt_n clusters supported on an anatase (101) TiO_2 surface were optimized, with n equal to 1, 2, 7, 10 and 37. For the Pt_1, Pt_7, and Pt_{10} clusters, several different initial configurations and starting locations on the surface were relaxed to discover the most stable geometry with the lowest total energy. Table 4.1 summarizes these total energies of different optimized structures. Three different adsorption sites were calculated for Pt_1 monomer: a bridge site between the two 2f-Oxygen, Pt(OO); a OTi site between the 2f-O and 5f-Ti atoms, Pt(OTi); and an OTiO site involving 2f-O, 6f-Ti and 3f-O atoms, Pt(OTiO). The three sites are selected according to Han et al [31], of which the Pt(OO) configuration was calculated to have the lowest energy, in agreement with this study. In this bridge Pt (OO) position, the bond lengths of the Pt atom with the neighboring atoms (two 2f-O, two 5f-Ti and two 6f-Ti, as seen in Figure 4.3a) are, on average, 2.02 Å and 2.76 Å with the O and Ti respectively. The Pt adsorption energy is 2.63 eV (Table 4.2), slightly lower than Han's calculated adsorption energy of 2.84 eV. This difference might be caused by the use of different pseudopotentials and exchange-correlation functional. The PAW pseudopotentials that we used is capable to provide more efficiency and reliability than the ultrasoft pseudopotentials that Han et al used [38]. And the PBE GGA that we utilized is improved from the PW91 GGA, the method that Han et al employed, by containing the correct fetchers of LDA that the PW91 ignores [36]. The bridge site Pt is 0.02 eV thermodynamically favorable to the OTiO position, and 0.87 eV favorable to the OTi position. Based on the canonical ensemble theory, the three Pt monomer sites were found to exist with the probability

ratio of Pt(OO): Pt (OTiO) = 2:1, and Pt(OO): Pt(OTi) = 9.53 x 10^{14} : 1 at room temperature. Although the energy difference between the Pt(OO) and Pt(OTiO) is too small to represent the real difference in realistic system, we still chose the Pt_1 bridge position as the main starting and final positions for a single Pt adatom diffusion study, as we will discuss in detail later. Figure 4.3 shows the most stable Pt_n clusters that were calculated in this study (n=1, 2, 7, 10, 35). The most stable configurations of Pt_1 and Pt_2 clusters are the same as found by Han et al, who calculated Pt_n clusters with n between 1 and 3.

In order to understand the adsorption geometry of a Pt_7 cluster on TiO_2, three different initial positions of the Pt_7 cluster were relaxed and the optimized structures are shown in Figure 4.2. All of the initial configurations are composed of a one layer, 2D circular structure with the (111) crystal facet, as shown in Figure 4.2a and 4.2b. The centers of the three initial configurations were chosen as the three optimized Pt_1 sites discussed above. Although the initial configurations are a 2-D layer, all of the relaxed structures are of a 3-D, island shape. This is due to the large cohesive energy of Pt. By forming a 3-D shape, the energy decreases stemming from more Pt-Pt bonds compared to Pt-TiO_2 surfaces bonds. The most stable Pt_7 cluster, shown in Figure 4.2c and 4.2d, has 4 Pt atoms directly interacting with the anatase surface while 3 Pt atoms are stacked on top of the bottom layer and have no connection with the TiO_2 surface. This Pt_7 structure is similar to a coupled tetragonal pyramid (CPT), the lowest energy geometry of Pt_7 reported in vacuum [43, 44]. Ge et al [44] demonstrated that the quintet state CPT is the most stable state with the 4 unpaired electrons mainly distributing on the 6 outermost Pt atoms, which correspond to the Pt atoms labeled as Pt1 to Pt6 in our surface studies (refer to Figure 4.2c and 4.2d). On the anatase surface, however, the CPT Pt_7 cluster was found to be a triplet. Upon

adsorption to the TiO_2 surface, the Pt-O and Pt-Ti bonds result in the unpaired electrons of Pt3 and Pt4 pairing up and leaving the two unpaired electrons localized on atom Pt1, Pt2, Pt5 and Pt6.

Table 4.1 Relative total energies of different Pt cluster configurations on TiO_2 for Pt_1, Pt_7 and Pt_{10} clusters, with respect to that of the structure with the lowest energy

Pt_n	configuration	ΔE (eV)
Pt_1	OO	0
	OTiO	0.02
	OTi	0.87
Pt_7	OTiO	0
	OTi	0.26
	OO	0.70
Pt_{10}	monlayer-1	1.17
	monolayer-2	1.33
	Dual layers-1	0
	Dual layers-2	0.32
	Dual layers-3	0.56
	Dual layers-4	1.09
	Dual layers-5	1.75

Seven different initial configurations of Pt_{10} were relaxed, two of which were 2D layers aligned along different directions of the TiO_2 surface and five of which were dual layers with different numbers of Pt atoms (1, 2 or 3) removed from the bottom layer and reassigned on the top layer. We name the seven configurations based on the nature of the initial position is a monolayer or a dual layer. Figure 4.2e and 4.2f give an example showing the initial structure of Pt_{10} (monolayer-1) and its optimized final geometry. As can be seen, the Pt_{10} cluster prefers a 3-

D rather than 2-D structure. Indeed, all of the optimized structures are island-like independent of whether the initial structure was a mono- or double-layer, and no matter where the initial configurations were localized on the TiO_2 surface. The most stable Pt_{10} configuration with the lowest total energy has 5 Pt atoms directly contacting the TiO_2 surface and the other 5 atoms connected to the bottom Pt layer, as shown in Figure 4.3d.

The above results demonstrate that the Pt growth thermodynamicly favors a 3-D structure, which is responsible for the island growth observed in Pt ALD, as the TEM images in Figure 4.5 show. Figure 4.5d clearly shows the Pt nanoparticle grows along the (111) face of its FCC crystal structure and that the particle size is around 2nm. With this in mind, a Pt_{37} cluster was constructed which has three atomic layers, with 19 atoms in the hexagonal shaped bottom layer, 12 atoms in the middle layer, and 6 atoms in the top layer. The cluster has an FCC structure with each layer composed of a (111) plane, consistent with the experimental observation. Since the footprint of the Pt_{37} cluster is large enough to cover many TiO_2 sites (see Figure 4.3e and Figure 4.7a), the total energy difference would be small if the Pt_{37} cluster changes location on the TiO_2 surface. So, the optimization calculation for different initial positions of the Pt_{37} cluster is not necessary. In addition, this 37 Pt atoms cluster structure corresponds to a hemispherical fragment of the 55 atom magic number FCC Pt nanoparticle. This hemispherical structure is believed to be the most stable state and, thus, no different initial configurations were tested. The behavior of the 37 hemispherical magic number is different from the 10 Pt atoms cluster, although 10 Pt atoms corresponds to the truncate of the 13 atom magic number of FCC Pt nanoparticles, the halving of the magic number structure greatly changes the behavior of the 10 Pt atoms cluster. Without the 3 Pt atoms of the bottom layer of the 13 Pt atom cluster, the symmetry of the cluster is broken and the bottom atoms have a reduced number of Pt-Pt bonds

and additionally the small number of Pt atoms in the system reduce its rigidity allowing the cluster to deform and create many more Pt-Pt bonds. In the larger 37 Pt atom cluster, though the symmetry is still broken, the system size provides a large number of Pt-Pt bonds and structural rigidity allowing the cluster's geometery to remain similar to that of a half magic number sphere.

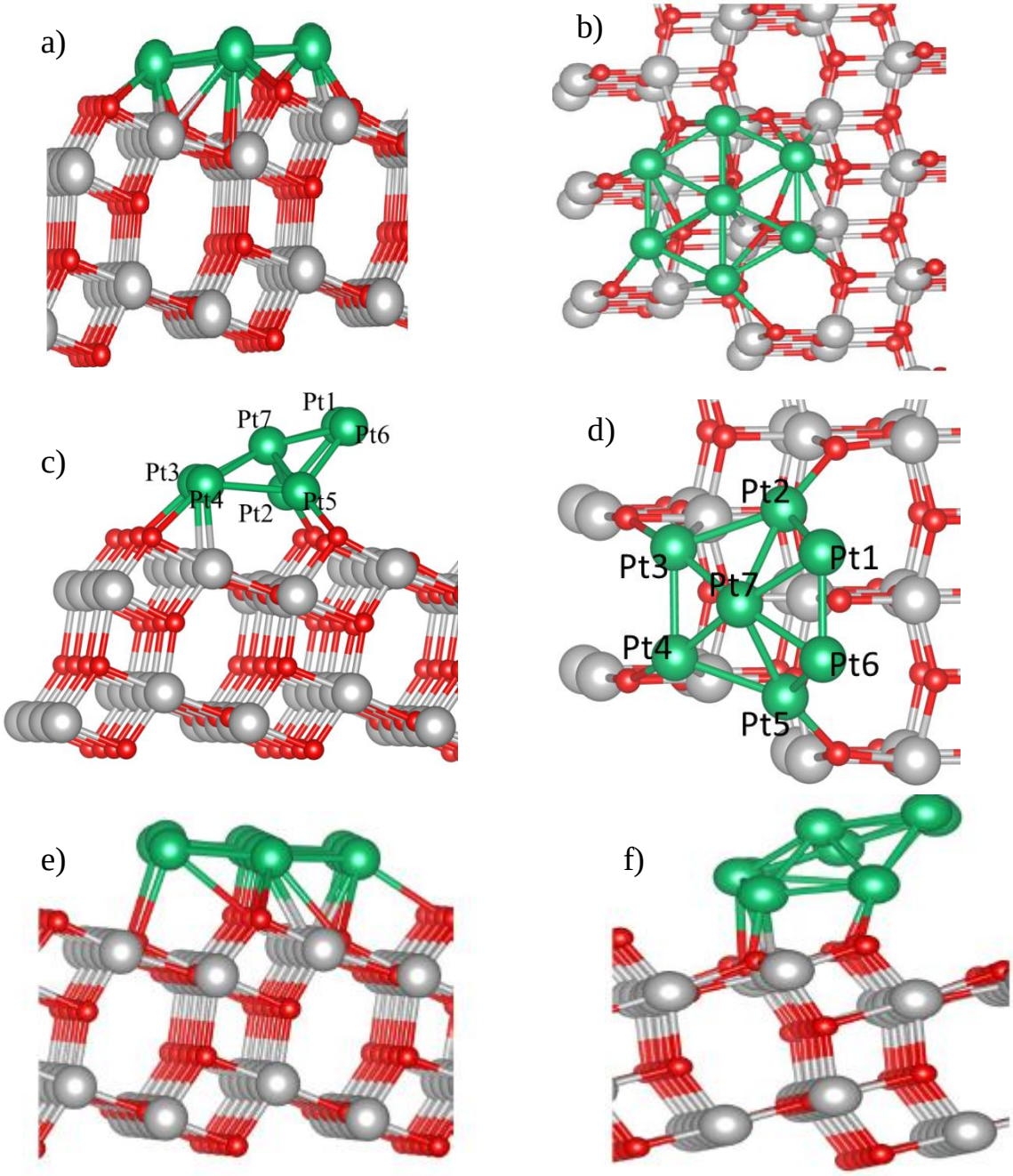

Figure 4.2 Configurations of Pt_7 and Pt_{10} clusters. a) side view of initial configuration of Pt_7 (OTiO), b) top view of initial configuration of Pt_7 (OTiO), c) side view of final configuration of Pt_7 (OTiO), d) top view of final configuration of Pt_7 (OTiO), e) initial configuration of Pt_{10} (monolayer-1). f) final configuration of Pt_{10} (monolayer-1). Large gray atoms are Ti, medium red atoms are oxygen and large green are Pt. If viewing in black and white, large light atoms, small dark atoms and large dark atoms represent Ti, O and Pt, respectively.

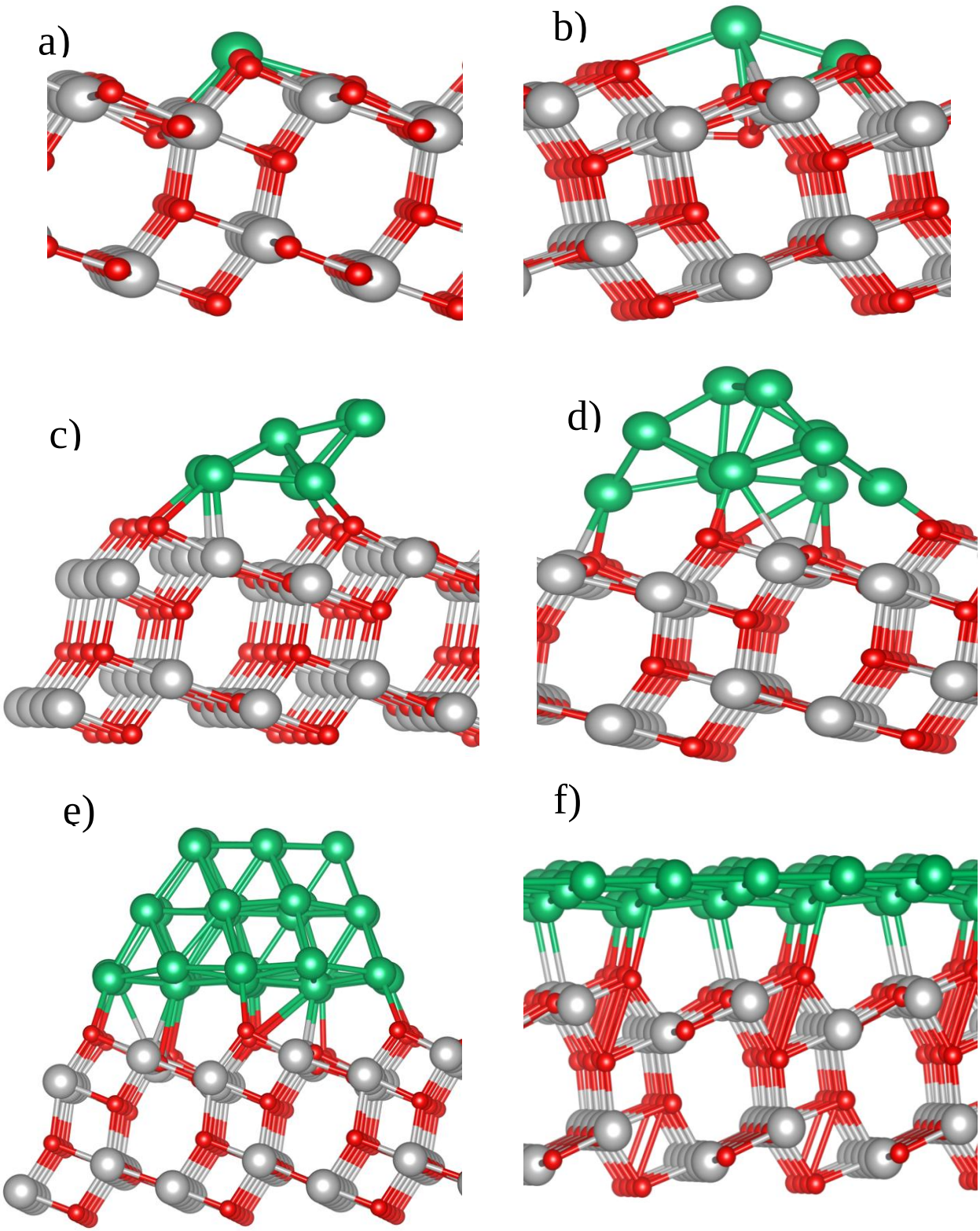

Figure 4.3 The most stable configurations of Pt_n cluster on TiO_2 a) Pt_1 b) Pt_2 c) Pt_7 d) Pt_{10} e) Pt_{37} f) Pt monolayer on TiO_2. Large gray atoms are Ti, medium red atoms are oxygen and large green are Pt. If viewing in black and white, large light atoms, small dark atoms and large dark atoms represent Ti, O and Pt, respectively.

4.3.2 The clustering energy of Pt particles

Table 4.2 summarizes the average cohesive energy of the Pt_n clusters in vacuum ($E^{coh}_{Pt_n}$) and the clustering energy on the TiO_2 surface ($E^{clu}_{Pt_n/TiO_2}$), and their difference. The Pt_n clusters in vacuum were relaxed from the most stable final configurations of the corresponding Pt_n clusters on the TiO_2 surface. The energies are also plotted with respect to the cluster size as shown in Figure 4.4. As Figure 4.4 shows, the clustering energy per Pt atom decreases with the Pt particle size, indicating that larger Pt particles are thermodynamically favored over smaller particles. This is because large particles have less interfacial area than a large number of small particles with the same volume; as a result, increasing the particle size decreases the high energy state associated with the interfaces. In the physics of solids, an interfacial surface is intrinsically less energetically favorable than bulk material; otherwise the bulk material will always be removed to create surfaces [45]. Therefore, a dispersion of solid particles has high overall energy due to large interfacial area and consequently high interfacial energy. Figure 4.4 shows that the clustering energy of the Pt_n cluster on the surface is lower than that of the same size cluster in vacuum, this is because the cluster energy contains two major components; one is the Pt-Pt interaction energy, which is accounted for in vacuum, and the other is the Pt-TiO_2 interaction, which is not. We can think of energy difference between the cohesive energy in the gas phase and the corresponding clustering energy on the TiO_2 surface as arising from the Pt-TiO_2 interaction. It is clear that the Pt-Pt interaction energy is much larger than the Pt-TiO_2 interaction energy, and can be seen in the fact that for a given state, the portion of the clustering energy that comes from placing the cluster on the surface is small. This high Pt-Pt bond energy is the reason for the formation of the island structure, because with the island structure more Pt-Pt bonds form and, as a result, lead to an overall lower system energy. Although the Pt-TiO_2

interactions are not as favorable as Pt-Pt interactions, they do allow for more bonding than that occurs when the Pt cluster is alone in vacuum, reducing the overall energy of the system. As the particle size grows, the energy difference becomes less. This is due to the lower proportion of the Pt atoms interacting with TiO_2 surface, resulting in less contribution from the Pt-TiO_2 interactions to the clustering energy. Therefore, with the particle size increasing, the Pt-Pt interactions play a more and more important role in reducing the system energy and it is reasonable to assume that all of the contributions of the clustering energy are from Pt-Pt interactions as the Pt particle size n approaching infinity. Consequently, the clustering energy decreases rapidly with particle size in the small size region and then the decrease slows with the particle increasing, and eventually approaches the Pt cohesive energy in bulk when the particle size approaches infinity, as shown in Figure 4.4. The bulk cohesive energy was calculated to be 6.03 eV, which is almost identical as Wang et al calculated with GGA-DFT (6.04 eV) [46], and close to the experimental value of 5.85 eV [47]. The large energy difference between the small and large clusters (the left region of the Figure 4.4) suggests that the small clusters are unstable and tend to shrink and subsequently adsorb into the large particles. This process is often referred to as Ostwald ripening, which involves atoms detaching from small particles and then migrating and reattaching to large particles. When both particles are large (the right hand region in the Figure 4.4), the insignificant energy difference indicates the driving force for the atoms to move from the smaller particles to the larger particle is low.

Table 4.2 The cohesive energy and clustering energy per Pt atom of Pt_n cluster in vacuum and on the TiO_2 surface

Pt_n	$E^{coh}_{Pt_n}$ (eV)	$E^{clu}_{Pt_n/TiO_2}$ (eV)	Difference (eV)
1		-2.63	-2.63
2	-1.76	-2.87	-1.10
7	-3.19	-3.57	-0.38
10	-3.40	-3.85	-0.44
37	-4.29	-4.37	-0.08
full monolayer		-4.58	-
monolayer with 1 / 6 defect		-4.09	-
Bulk		-6.03	-

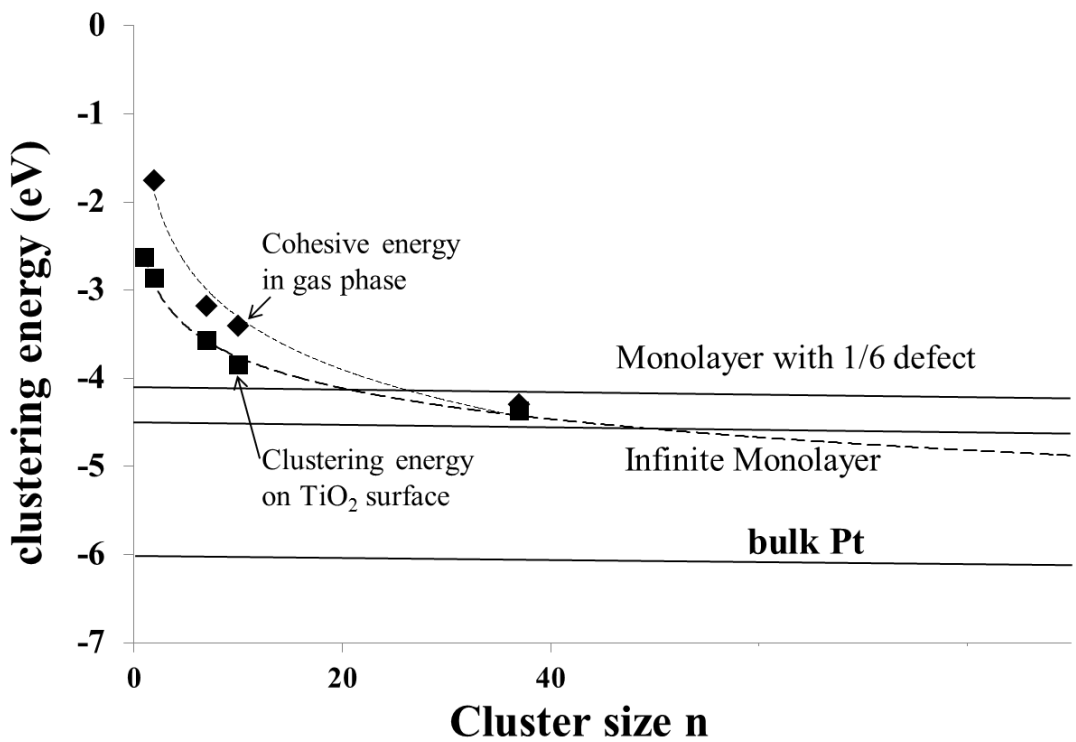

Figure 4.4 Plot of the clustering energy per Pt atom for adsorption on the TiO_2 surface versus the Pt particle size

Figure 4.3f shows a full monolayer Pt film on the TiO_2 surface. The clustering energy per Pt atom in this infinite monolayer is -4.57ev, below that of the largest Pt cluster calculated in this study (Pt_{37}), while higher than that for a Pt cluster with larger cluster size, e.g. 50 Pt atoms, calculated by extrapolating the data points (see the dash line in Figure 4.4). However, for a Pt monolayer with defects, i.e. some Pt atoms missing from the perfect monolayer, the clustering energy increases from that of the perfect monolayer. For example, we calculated a planer layer of Pt with 1/6 of the Pt atoms removed from the perfect monolayer and found the clustering energy to be -4.09 ev, less favorable than that of the Pt_{37} cluster. Therefore, if a monolayer has defects, which must be the case as a monolayer is assembled, the Pt planer structure is even less thermodynamically favorable than perfect monolayer. When more defects are present, for instance only small number of Pt atoms on the surface, the total energy of a Pt planer structure on the TiO_2 surface should be higher than that of the corresponding size island structure, and thus result in the formation of islands rather than a planer configuration, as we discussed above. This demonstrates again that Pt growth does not favor a monolayer, but, rather an island structure, in agreement with experimental observation. Our Pt ALD experiments provide evidence for the island growth of Pt, as the TEM images, seen in Figure 4.5, for different numbers of cycles of Pt ALD deposited on TiO_2 particles (Pt/TiO_2) shows.

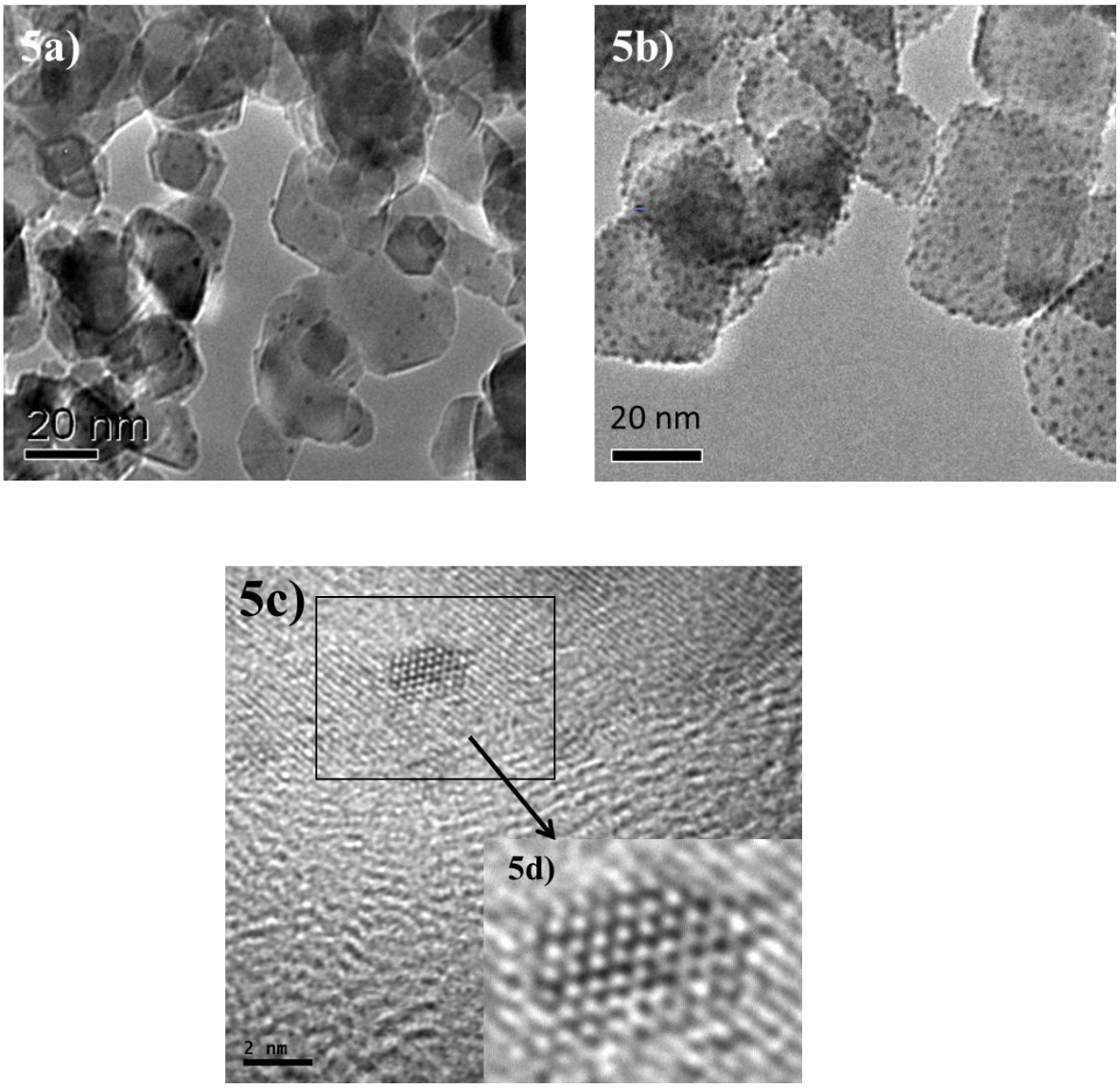

Figure 4.5 TEM images of Pt deposited TiO_2 nanoparticles by ALD. a) 1 cycle of Pt ALD deposited sample, b) 20 cycles of Pt ALD deposited sample, c) high resolution TEM image of sample b) , d) zoom into the crystal structure of the Pt nanoparticle in image c).

4.3.3 Pt diffusion on TiO_2 surface

Although large Pt particles are thermodynamically favorable, new nucleation and growth occurs to form more particles after each ALD cycle, as observed in the TEMs. As we know, the

formation of new particles is related to nucleation and diffusion kinetics. Nucleation involves random statistical probability and can be understood from canonical ensemble theory and attempt frequency. Diffusion kinetics controls Pt migration from small particles to large ones. Among these two factors, the kinetic limitation is believed to be more important for the number and size of the Pt particles for an extended time perspective, so we focus on the study of Pt diffusion on TiO_2 surface.

A simple hopping model based on the CI-NEB method was utilized here to study the activation barrier for the diffusion of single Pt adatom. Two hop directions were calculated, one is along the surface bridge oxygen rows, the [010] direction, and the other one is a crossing from one the bridge oxygen row to another, the $[10\bar{1}]$ direction (see Figure 4.6).

Along the [010] direction two different hopping paths were found. In the first path as shown in Figure 4.6a, the Pt adatom hops directly from one bridge site to the next bridge site, through a metastable position at the OTi site. The energy barrier for this migration path is 1.07 eV, associated with the hop from bridge site 1 to the metastable site, as the rough estimation of the overall diffusion activation energy contains the hopping from the lowest to the highest energy sites on the potential energy surface. Once in the metastable position a 0.23 ev barrier is required for movement to the second bridge site, or hopping back to the original bridge site due to the random walk behavior. The second path, shown in Figure 4.6b, is a migration path of bridge site 1– OTiO site – bridge site 2. Along this migration path from the bridge site 1 to OTiO position, there is an activation barrier of 0.86 eV to move from the bridge site 1 to a metastable TiOO position. When a Pt sits in the TiOO metastable position, the Pt is more likely to continue forward to the OTiO, as the activation barrier of 0.34 eV for the Pt forward, is much lower than the barrier of 0.55 eV to go backwards. This is different from the direct bridge site – bridge site

path discussed above, where the Pt is equally likely to leave metastable position and travel backwards as it is to move forward. Once in the OTiO position, a reverse set of processes lead to either further Pt forward movement or movement back to its original bridge site 1 position equally, with both activation barriers of 0.78 eV, though the Pt atom is likely to get trapped at the OTiO site far longer than it gets stuck at the TiOO. The migration of Pt from a bridge site to a OTiO site and continuing to a bridge site has a lower activation barrier (0.86 eV) than the direct bridge site to bridge site path (1.07 eV), suggesting the bridge site – OTiO – bridge site fashion is the more likely path for Pt moving in the [010] direction. However, the high energy barrier for the direct bridge site path, and the relatively large barrier for movement along the OTiO path indicate that Pt atom movement along the [010] direction, will be slow at room temperature resulting in limited sintering process.

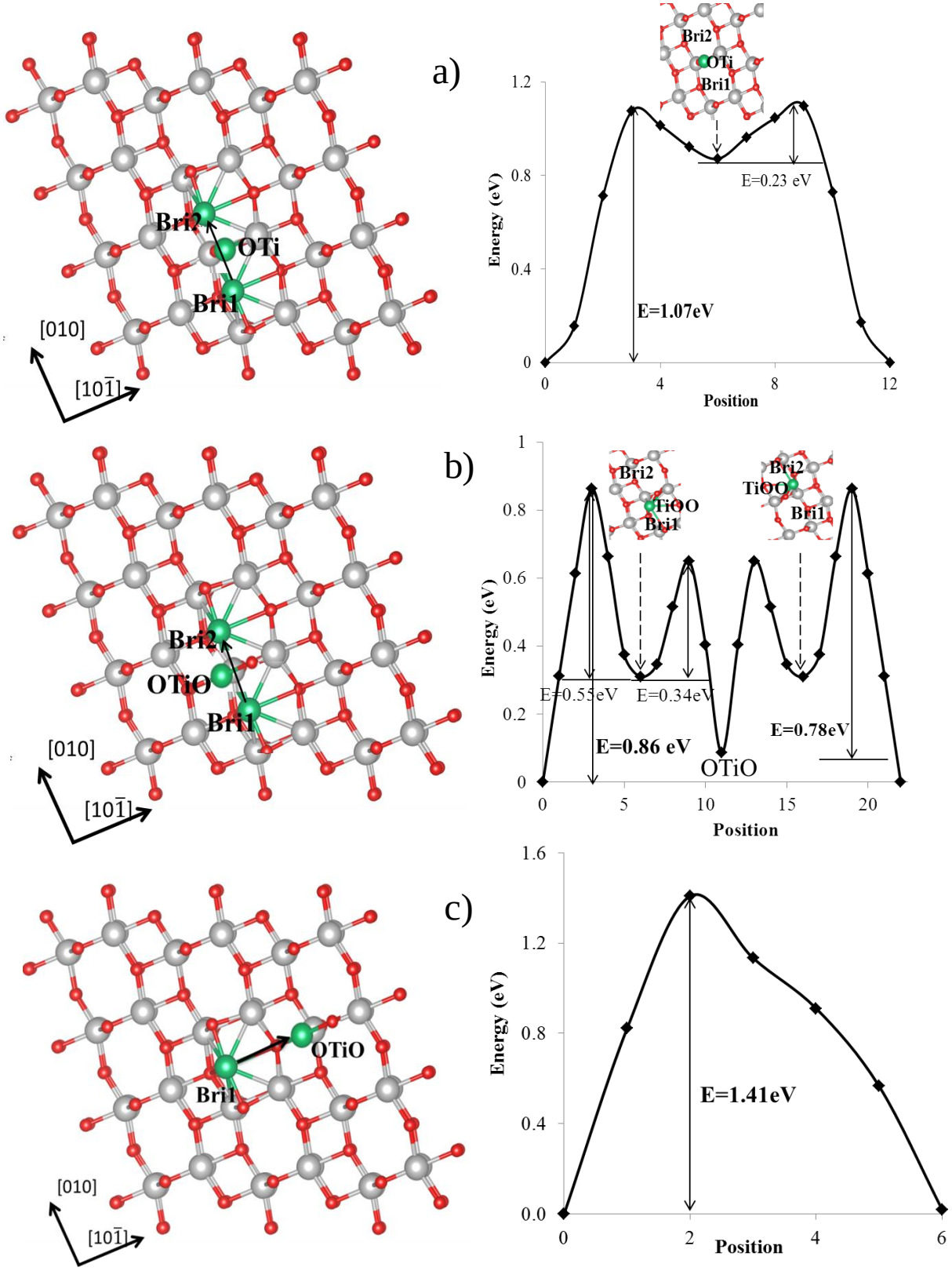

Figure 4.6 The diffusion of single Pt adatom and the activation energy for a) Pt diffusion along [010] direction from bridge site 1 to bridge site 2 through OTi position, b) Pt diffusion along [010] direction from bridge site 1 to bridge site 2 through OTiO position, c) Pt diffusion along [$10\bar{1}$] direction from bridge site 1 to OTiO position.

When a Pt adatom diffuses along the $[10\bar{1}]$ direction, that is, moving across one row of bridging O to another, the Pt adatom hops starting from the bridge site 1 to the almost equally stable OTiO site, as Figure 4.6c shows. A direct bridge site to bridge site path from one bridge O row to another was attempted and we found that the path broke up into the initial bridge site to OTiO $[10\bar{1}]$ path coupled with the OTiO to the destination bridge site [010] path, the latter is exactly the same as discussed above. The activation barrier along the $[10\bar{1}]$ direction is 1.41 eV. This barrier is larger than the low energy barrier along the [010] direction path by 0.56 eV, as a result of the less dense TiO_2 surface atom arrangement along the $[10\bar{1}]$ direction, which in turn leads to less coordination of the migrating Pt along this path compared to the hop along the [010] direction. The higher energy barrier indicates the extremely low mobility of Pt along the $[10\bar{1}]$ direction.

The hopping rate, that is, the mean number of hoping events per second between two sites, is given by the following equation:

$$\eta = \upsilon \exp(-E_a / kT) \qquad (4)$$

where E_a is the energy barrier between the sites as calculated above, ν is oscillation frequency and is typically chosen as v= $1x10^{13}$, and k is Boltzmann's constant (8.617×10^{-5} eV/K). At room temperature, the hopping rate is 2.57×10^{-5} s^{-1} along the direct bridge site to bridge site [010] direction, 0.03 s^{-1} along the OTiO [010] path and 9.64×10^{-12} s^{-1} along the $[10\bar{1}]$ direction. The energy activation barrier difference between the two [010] paths lead to the OTiO path occurring 99.99% of the time. The difference is more exaggerated for the comparisons of rates along the two different directions, with the [010] path being 2.97×10^{10} faster than along the $[10\bar{1}]$ direction. Even though the diffusion along the [010] direction is more favorable than

along $[10\bar{1}]$ direction, its activation barrier is still relatively high leading to low hopping rate, suggesting that Pt migration is slow at room temperature. Deskins et al studied a single Pt adatom diffusion on γ-Al_2O_3 surfaces and indicated that the Pt sintering process is hindered at temperature below 500K [32]. At elevated temperature, the hopping rates increase significantly. For instance, at 300 ^{o}C, the typical Pt ALD temperature, the hopping rate along the favorable [010] direction is 2.73 x 10^5 s^{-1}, and 3.2 s^{-1} along the $[10\bar{1}]$ direction. These higher hopping rates indicate that Pt atom diffusion over the TiO_2 surface becomes more likely at high temperature especially along the [010] direction which, at 300 ^{o}C is now ~85000 times faster than that hops along the $[10\bar{1}]$ direction. Diffusion of Pt along the [010] direction is, therefore, the prevalent path during the Pt growth and sintering process.

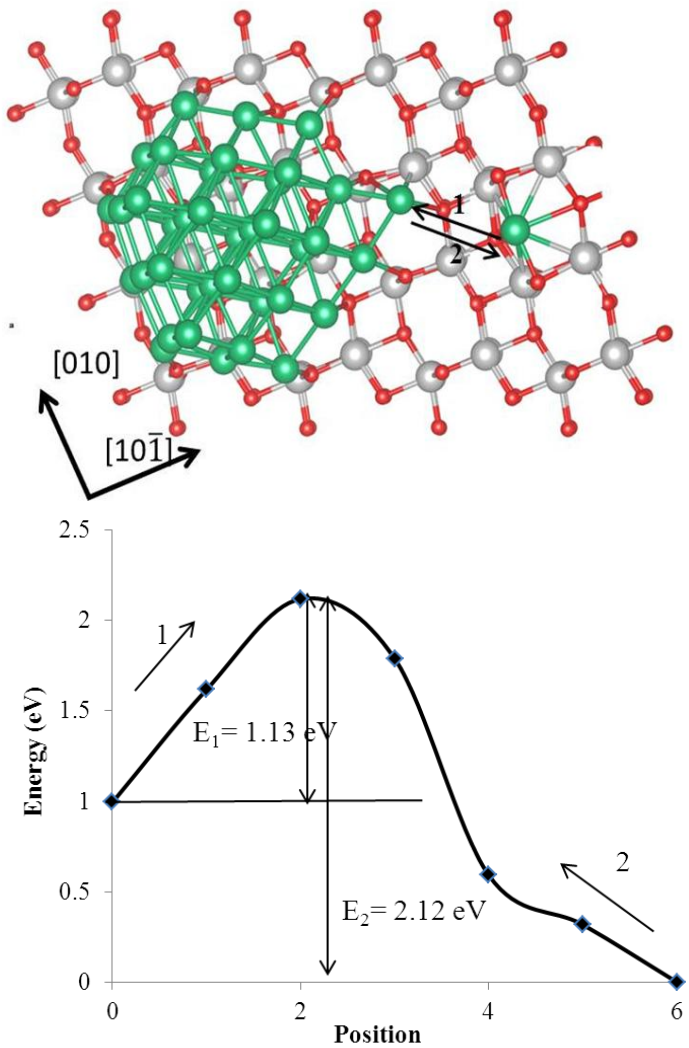

Figure 4.7 The adsorption and desorption energy of Pt atom to the Pt_{37}/Pt_{38} cluster

In addition to the single Pt adatom diffusion across the TiO_2 surface, the diffusional process involved in ripening is also important for Pt particle growth during the Pt deposition. When a new Pt atom reaches the TiO_2 surface in an ALD cycle, the Pt adatom may randomly move over the support surface and attach to a neighboring particle, while this attached atom may or may not be stable depending on the size of the particle. If the particle is small, the adsorbed

atom may escape from the particle, diffuse across the support and attach to a large particle then become trapped there, since large particles are more energetically favorable than small particles. The driving force for the atoms movement to large particles comes from the higher chemical potential of the metal atoms in small particles as a consequence of the small radius of curvature. As a result, large particles grow at the expense of small ones during Ostwald ripening. In order to understand the ripening behavior of Pt/TiO_2 system, we calculated the adsorption of a Pt atom to a Pt_{37} cluster and the reversible process, that is, the desorption of a Pt atom from a Pt_{38} cluster. As Figure 4.7 shows, the adsorption energy barrier is 1.13 eV, between the two barriers for the Pt diffusion over the TiO_2 surface along the [101] direction and the $[10\bar{1}]$ direction, as discussed above. The desorption energy barrier is significantly larger than the adsorption energy by around 1 eV. This large desorption barrier results in Pt atoms detaching from particles a rare event, and hence slows the Ostwald ripening process. After a new cluster nucleates and then newly arrived Pt atoms attach, the high desorption barrier inhibits the Pt detaching from the small particles, even though it is thermodynamically favorable for Pt atoms to be released from a small cluster and reattach to a large particle. This slow ripening limited by the interface transfer is the main reason for the existence of a large number of relatively small nanoparticles, rather than small numbers of large particles, after Pt ALD process, as we observed in the TEM images (Figure 4.5).

4.4 Conclusions

The Pt particle growth and diffusion behavior were studied using first principle DFT calculations and demonstrated with Pt ALD on TiO_2. Pt_n clusters with n up to 37 atoms were calculated and the most stable configurations among the calculated structures were identified. Due to the large cohesive energy, Pt prefers to form 3-D structures rather than 2-D structures or

monolayers on the TiO_2 surface. The clustering energy of Pt on TiO_2 decreases with Pt particle size increasing and approaches the cohesive energy of bulk Pt when the size approaches infinity. The monotonic decrease trend in the clustering energy with the Pt size indicates that large particles are always thermodynamically favored. A model monolayer was found to be relatively stable, and is estimated to be more thermodynamically favorable than islands containing 50 atoms, but once defects are incorporated into the monolayer it become much less stable, favoring island formation. In order to evaluate whether Pt atoms diffuse easily over the perfect anatase TiO_2 (111) surface or are essentially immobile, the diffusion behavior of a single Pt adatom along [010] and $[10\bar{1}]$ directions was investigated by a CI-NEB calculations. Pt migration along the [010] direction was found to take place through a bridge site – OTiO – bridge site path rather than a direct bridge site – bridge site path. The activation barrier for a Pt adatom hopping along the [010] direction was found to be lower by 0.56 eV than that for hopping along the $[10\bar{1}]$ direction. This lower barrier corresponds to a hopping rate along the [010] direction 10^{10} times larger than that along the $[10\bar{1}]$ direction at room temperature and more than 85000 times faster at 300°C, the typical Pt ALD temperature. So the hopping along the surface bridge oxygen row ([010] direction) should be the prevalent path for Pt diffusion over the anatase (101) surface. However, the overall low diffusion rate suggests the sintering is slow, especially at room temperature. The energy barrier of Pt removal from a Pt cluster was calculated to be large （2.12 eV）which suggests extremely rare occurrences of Pt atom detaching from Pt particles. This interface transfer limited ripening process should be responsible for the large number of small nanoparticles after the Pt ALD process. Overall, this theoretical study explores Pt particle growth and diffusion characteristics, which are significant for the Pt/TiO_2 application.

4.5 References

1. Climent, M.J., A. Corma, and S. Iborra, Converting carbohydrates to bulk chemicals and fine chemicals over heterogeneous catalysts. Green Chemistry, 2011. 13(3): p. 520-540.

2. Farnood, R. and P. Azadi, Review of heterogeneous catalysts for sub- and supercritical water gasification of biomass and wastes. International Journal of Hydrogen Energy, 2011. 36(16): p. 9529-9541.

3. Hara, M., Environmentally Benign Production of Biodiesel Using Heterogeneous Catalysts. Chemsuschem, 2009. 2(2): p. 129-135.

4. Yin, S.F., et al., The direct transformation of carbon dioxide to organic carbonates over heterogeneous catalysts. Applied Catalysis a-General, 2009. 366(1): p. 2-12.

5. Wang, S.B., Application of solid ash based catalysts in heterogeneous catalysis. Environmental Science & Technology, 2008. 42(19): p. 7055-7063.

6. Galan, M.A., et al., Simulation three-way catalyst ageing - Analysis of two conventional catalyst. Applied Catalysis B-Environmental, 2003. 44(1): p. 41-52.

7. Hirata, H., et al., Characterization and dynamic behavior of precious metals in automotive exhaust gas purification catalysts. Catalysis Today, 2011. 164(1): p. 467-473.

8. Vlachos, D.G. and Y. Chen, Hydrogenation of Ethylene and Dehydrogenation and Hydrogenolysis of Ethane on Pt(111) and Pt(211): A Density Functional Theory Study. Journal of Physical Chemistry C, 2010. 114(11): p. 4973-4982.

9. Vlachos, D.G., M. Salciccioli, and Y. Chen, Microkinetic Modeling and Reduced Rate Expressions of Ethylene Hydrogenation and Ethane Hydrogenolysis on Platinum. Industrial & Engineering Chemistry Research, 2011. 50(1): p. 28-40.

10. Yang, H. and Z.M. Peng, Designer platinum nanoparticles: Control of shape, composition in alloy, nanostructure and electrocatalytic property. Nano Today, 2009. 4(2): p. 143-164.

11. Vidotti, M., et al., Platinum nanoparticle-modified electrodes, morphologic, and electrochemical studies concerning electroactive materials deposition. Journal of Solid State Electrochemistry, 2010. 14(4): p. 675-679.

12. Bedzyk, M.J., et al., Controlled Growth of Platinum Nanoparticles on Strontium Titanate Nanocubes by Atomic Layer Deposition. Small, 2009. 5(6): p. 750-757.

13. Christensen, S.T., et al., Nanoscale Structure and Morphology of Atomic Layer Deposition Platinum on SrTiO3 (001). Chemistry of Materials, 2009. 21(3): p. 516-521.

14. King, J.S., et al., Ultralow loading Pt nanocatalysts prepared by atomic layer deposition on carbon aerogels. Nano Letters, 2008. 8(8): p. 2405-2409.

15. Zhou, Y., et al., Optimal preparation of Pt/TiO2 photocatalysts using atomic layer deposition. Applied Catalysis B-Environmental, 2010. 101(1-2): p. 54-60.

16. Weimer, A.W., et al., Highly dispersed Pt nanoparticle catalyst prepared by atomic layer deposition. Applied Catalysis B-Environmental, 2010. 97(1-2): p. 220-226.

17. Lin, Y.H., et al., Enhancing the Photon-Sensing Properties of ZnO Nanowires by Atomic Layer Deposition of Platinum. Electrochemical and Solid State Letters, 2010. 13(12): p. K93-K95.

18. Hersam, M.C., et al., Nanoscale Structure and Morphology of Atomic Layer Deposition Platinum on SrTiO(3) (001). Chemistry of Materials, 2009. 21(3): p. 516-521.

19. George, S.M., et al., Nucleation and growth of Pt atomic layer deposition on Al(2)O(3) substrates using (methylcyclopentadienyl)-trimethyl platinum and O(2) plasma. Journal of Applied Physics, 2011. 109(8).

20. Valden, M., X. Lai, and D.W. Goodman, Onset of catalytic activity of gold clusters on titania with the appearance of nonmetallic properties. Science, 1998. 281(5383): p. 1647-1650.

21. Abida, B., et al., Preparation and characterization of Pt/TiO(2) nanotubes catalyst for methanol electro-oxidation. Applied Catalysis B-Environmental, 2011. 106(3-4): p. 609-615.

22. Lee, S.K., Platinum and palladium in semiconductor photocatalytic systems. Platinum metals review 2003. 47(2): p. 61-72.

23. Mills, A., Platinisation of Semiconductor Particles. J.Chem.Soc.,Chem.Commun., 1982: p. 367.

24. Yu, J., L.Qi, and M. Jaroniec, Hydrogen Production by Photocatalytic Water Splitting over Pt/TiO2 Nanosheets with Exposed (001) Facets. J.phys.Chem.C, 2010. 114(30): p. 13118-13125.

25. Li, G.X., et al., Study of Pt/TiO(2) nanocomposite for cancer-cell treatment. Journal of Photochemistry and Photobiology B-Biology, 2010. 98(3): p. 207-210.

26. Inagaki, M., et al., Photocatalytic activity of anatase powders for oxidation of methylene blue in water and diluted NO gas. Applied Catalysis B-Environmental, 2004. 51(4): p. 247-254.

27. Inagaki, M., et al., Dependence of photocatalytic activity of anatase powders on their crystallinity. Chemosphere, 2006. 64(3): p. 437-445.

28. Fujimoto, M., et al., Resistivity and resistive switching properties of Pr0.7Ca0.3MnO3 thin films. Applied Physics Letters, 2006. 89(24).

29. Aschauer, U., J. Chen, and A. Selloni, Peroxide and superoxide states of adsorbed O-2 on anatase TiO2 (101) with subsurface defects. Physical Chemistry Chemical Physics, 2010. 12(40): p. 12956-12960.

30. Gong, X.Q., et al., Small au and pt clusters at the anatase TiO2(101) surface: Behavior at terraces, steps, and surface oxygen vacancies. Journal of the American Chemical Society, 2008. 130(1): p. 370-381.

31. Liu, C.J., Y. Han, and Q.F. Ge, Interaction of Pt clusters with the anatase TiO2(101) surface: A first principles study. Journal of Physical Chemistry B, 2006. 110(14): p. 7463-7472.

32. Deskins, N.A., D.H. Mei, and M. Dupuis, Adsorption and diffusion of a single Pt atom on gamma-Al(2)O(3) surfaces. Surface Science, 2009. 603(17): p. 2793-2807.

33. Neyman, K.M., A. Bruix, and F. Illas, Adsorption, Oxidation State, and Diffusion of Pt Atoms on the CeO(2)(111) Surface. Journal of Physical Chemistry C, 2010. 114(33): p. 14202-14207.

34. Kresse, G., et al., Efficient iterative schemes for ab initio total-energy calculations using a plane-wave basis set. Physical Review B, 1996. 54(16): p. 11169.

35. Kresse, G. and J. Furthmüller, Efficiency of ab-initio total energy calculations for metals and semiconductors using a plane-wave basis set. Computational Materials Science, 1996. 6(1): p. 15-50.

36. Perdew, J.P., K. Burke, and M. Ernzerhof, Generalized Gradient Approximation Made Simple. Physical Review Letters, 1996. 77(18): p. 3865.

37. Blöchl, P.E., Projector augmented-wave method. Physical Review B, 1994. 50(24): p. 17953-17979.

38. Kresse, G. and D. Joubert, From ultrasoft pseudopotentials to the projector augmented-wave method. Physical Review B, 1999. 59(3): p. 1758-1775.

39. Henkelman, G., A. Arnaldsson, and H. Jónsson, A fast and robust algorithm for Bader decomposition of charge density. Computational Materials Science, 2006. 36(3): p. 354-360.

40. Sanville, E., et al., Improved grid-based algorithm for Bader charge allocation. Journal of Computational Chemistry, 2007. 28(5): p. 899-908.

41. Ropo, M., K. Kokko, and L. Vitos, Assessing the Perdew-Burke-Ernzerhof exchange-correlation density functional revised for metallic bulk and surface systems. Physical Review B, 2008. 77(19).

42. Mills, G., H. Jonsson, and G.K. Schenter, Reversible Work Transition-State Theory - Application to Dissociative Adsorption of Hydrogen. Surface Science, 1995. 324(2-3): p. 305-337.

43. Cheng, H.S., et al., Structural evolution of subnano platinum clusters. International Journal of Quantum Chemistry, 2007. 107(1): p. 219-224.

44. Ge, M.F., et al., Geometrical and electronic structure of the Pt-7 cluster: A density functional study. Journal of Physical Chemistry A, 2004. 108(17): p. 3806-3812.

45. Ratke, L. and P.W. Voorhees, Growth and coarsening: ripening in material processing. 2002.

46. Wang, L.Y., M. Eikerling, and A. Roudgar, Ab Initio Study of Stability and Site-Specific Oxygen Adsorption Energies of Pt Nanoparticles. Journal of Physical Chemistry C, 2009. 113(42): p. 17989-17996.

47. Lide, D.R., Handbook of Chemistry and Physics. 1990, CRC Dekker: Boca Raton, FL. p. 1991.

CHAPTER 5

The Effect of Surface Deposited Pt on the Photoactivity of TiO_2: DFT study

Abstract

The role of Pt clusters on anatase TiO_2 (101) surfaces have been studied using density functional theory. The calculated electronic structure of Pt clusters supported on (101) anatase shows that excited electrons and holes are trapped by Pt nearly equally, upon addition of an extra electron 0.57 e^- localizes on the Pt cluster, while the addition of a hole causes the loss of 0.59 e^- from the Pt cluster. Pt states were found to completely bridge the band gap and act as electron-hole recombination centers, which is deleterious to the photoactivity of TiO_2. In addition, the O_2 adsorption behavior was calculated on TiO_2 surface and on Pt cluster. The calculations show that O_2 will not adsorb on the TiO_2 surface unless an extra electron or subsurface defect exists. In aqueous solutions, O_2/TiO_2 interactions are rare because water covers the surface. On the other hand, the Pt cluster significantly enhances the adsorption of O_2, due to the high O_2 adsorption energy of -1.69 eV and large number of adsorption sites on the Pt cluster. This results in enhanced photocatalytic performance because O_2 can scavenge electrons more efficiently from Pt than from TiO_2, increasing the interfacial electron transfer rate. The initial increase and subsequent decrease in TiO_2's photoactivity with increasing Pt loading can be explained by the competition between increased O_2 adsorption and electron-hole recombination. At Pt loadings above the optimum level the increased electron-hole recombination outweighs the increased O_2 adsorption, which is limited by its concentration and diffusion in solution. Furthermore, the projected density of states shows that although surface deposited Pt does not red shift TiO_2 bands,

it does bridge the bandgap. This leads to visible light absorption, but not visible light photoactivity as verified experimentally using methylene blue as a probe.

5. 1 Introduction

Due to their high photoactivity, chemical stability and low cost, TiO_2 photocatalysts have been widely applied since their discovery in the 1970's. To improve the photoactivity of TiO_2, platinum doping has been widely studied and reported by numerous researchers to enhance TiO_2 photoactivity [1-8]. However, the mechanism for the improved photoactivity is still not clearly understood. In addition, the level of Pt loading was found to be critical to the photoactivity. Numerous reports have indicated the existence of an optimal weight loading of Pt for photo oxidation of pollutants [1, 4, 5, 8-11]. For example, Kennedy *et al.* report that the optimum loading of Pt is 1.0 wt% for photo oxidation of liquid phase alcohols [4]. Lam *et al.* suggested that Pt/TiO_2 exhibits a maximum photoactivity at a Pt loading of 2 wt% for resorcinol degradation [5]. Cho *et al.* observed that Pt deposited on TiO_2 increased the overall photocatalytic decomposition of O_3 up to 1 wt% Pt loading [1]. We have also observed that the photocatalytic activity of TiO_2 first increases and then decreases with increasing Pt loading, reaching a maximum at an optimum weight loading. When we deposited Pt nanoparticles on Degussa P25 TiO_2 powders by atomic layer deposition (ALD), the photoactivity of TiO_2 increased by three-fold with increasing number of Pt ALD cycles from one to three and subsequently decreased with additional Pt ALD cycles, which corresponds to higher Pt loading [12]. To explain this effect some reports have suggested that Pt doping serves as an electron-hole (e-h) *separation* center and therefore inhibits e-h recombination at low Pt loading, but that at high loading Pt acts as an e-h *recombination* center [3, 9, 10, 13, 14]. Unfortunately, this

suggestion has not been verified, leaving the field with no proven fundamental explanation for how Pt affects the photoactivity of TiO_2.

Photocatalytic reactions take place when photons with energies in excess of the band gap excite electrons from the semiconductor valence band into the conduction band to create electron-hole pairs. The e-h quasiparticle can separate into free carriers with the electron or hole migrating to a surface where the photoinduced electron can reduce an acceptor molecule or the hole can oxidize a donor molecule. Since the reactions involve electron transfer between the semiconductor surface and the reacting species, these photocatalytic reaction processes usually occur with species adsorbed to the surface. Surface adsorbed water or hydroxide anions act as the hole acceptor to produce hydroxyl radicals, although some organic materials may directly accept holes from TiO_2 [2, 15] :

$$H_2O + h^+ \rightarrow HO\cdot + H^+ \qquad (5.1)$$

$$OH^- + h^+ \rightarrow HO^\cdot \qquad (5.2)$$

In TiO_2 photocatalysis, surface adsorbed dioxygen functions as the primary electron acceptor and no photocatalysis is observed to occur in the absence of O_2 [15]. The reduction of dioxygen has also been demonstrated to be the rate-limiting step in semiconductor photocatalysis [15, 16]. In aqueous solutions, the following scheme has been proposed [15] to describe how surface adsorbed O_2 scavenges electrons:

$$O_2 + e^- \rightarrow O_2^{\cdot-} \qquad (5.3)$$

$$O_2^{\cdot-} + H^+ \rightarrow HO_2\cdot \qquad (5.4)$$

These reactive oxygen species on illuminated TiO_2 surfaces may contribute to the oxidation of organic compounds by acting as a direct electron acceptor or as a source of hydroxyl radicals, a very strong oxidizer, as shown by the following scheme:

$$HO_2 \cdot + e^- + H^+ \rightarrow H_2O_2 \qquad (5.5)$$

$$H_2O_2 + e^- \rightarrow HO \cdot + OH^- \text{ or } H_2O_2 \rightarrow 2HO \cdot \qquad (5.6)$$

Here, the produced peroxy species undergo reaction to produce H_2O_2, which subsequently converts to hydroxy species. OH radicals serve as the principal reactive oxidant in photodegradation of organic pollutants. As O_2 acts so important as an electron scavenger and it is the rate-limiting step in photocatalysis, an important question is how Pt supported on TiO_2 affects dioxygen as an electron scavenger to enhance photocatalysis.

In this study, the effect of Pt clusters on the photoactivity of TiO_2 was studied theoretically using electronic structure calculations based on density functional theory (DFT). DFT has become an invaluable theoretical tool in describing materials and molecular systems at a sufficient level of accuracy to make relatively accurate predictions of their behavior at a reasonably modest computational cost. Among a wide variety of applications, it has been used previously to describe properties relevant to the present study, including the electronic structure of crystalline semiconductor materials, the mechanisms of chemical reactions and the effect of catalysts to provide lower barrier pathways for chemical transformations.

Our model systems are based on the TiO_2 (101) anatase surface. Anatase is the major crystalline phase present in P25 TiO_2 powders and possesses the highest photoactivity among the three TiO_2 crystal structures (anatase, rutile and brookite); the (101) face is the most stable and abundant anatase surface [17, 18]. As a baseline for comparison with the effects of Pt, we first investigated the O_2 adsorption and related electronic properties on TiO_2. After that, a 37 atom Pt cluster supported on TiO_2 (101) anatase was employed as our model system. We selected a 37 atom Pt cluster because its diameter of 1.4 nm is similar to that of the Pt clusters we observed experimentally [12] and a 37 atom structure corresponds to a hemispherical fragment of the 55

atom magic number FCC Pt nanoparticle. Furthermore, a 37 atom cluster supported on a 144 atom TiO_2 supercell adequately describes the system while remaining within the practical limit of tractable DFT calculations. The electronic structure of the Pt/TiO_2 system was studied thoroughly and the O_2 adsorption behavior on the supported Pt cluster was investigated. Moreover, as H_2O is another source of OH radicals, H_2O adsorption was also investigated on the TiO_2 and Pt/TiO_2 surfaces. Finally, we used both theoretical analysis and photochemical experiments to study the effect of Pt on the photoactivity of TiO_2 under visible light illumination, which has been of great interest to numerous researchers in recently years [10, 19-22]. Our study provides the fundamental understanding of this important area considering the high interest in visible light photoactivity of TiO_2 because UV light represents only approximately 3% of the solar spectrum.

5. 2 Methods

5.2.2 Computational Methods

Plane wave periodic boundary condition DFT simulations were performed using the Vienna Ab initio Simulation Program (VASP) [23, 24]. The Perdew-Burke-Ernzerhof (PBE) generalized gradient approximation (GGA) exchange and correlation functional [25] was used coupled with projector augmented wave (PAW) pseudopotentials. In our case, PAW's were used to describe the H 1s; O 2s and 2p; C 2s and 2p; Ti 3p, 4s and 3d; and Pt 6s and 5d electrons explicitly, while freezing the remaining core electrons. A cut off energy study was conducted in the range of 200 to 500 eV with 400 eV determined to be sufficiently accurate; all calculations utilize a 400 eV cut off energy. All calculations were conducted at the Γ-point as the Γ-point accurately spans k-space for large unit cells, and reduces computational expense. This was

confirmed using a k-point study that demonstrated that the Γ-point was sufficient for our unit cells; we obtained a Γ point cell energy of 1,272.43 eV and a cell energy using a 2×2×2 Monkhorst-Pack k-point mesh of 1,272.38 eV for a unit cell containing a single Pt atom on a 144 atom TiO_2 slab. Bader charge analysis was conducted using software from the Henkelman group [26, 27]. Additionally, we carried out GGA+U calculations to investigate the effect of electron localization on the systems studied [17]. A Hubbard term [28] of U_{eff} = 3.5 eV on the Ti d-electrons, which attempts to provide better electron correlation by imposing an energy penalty for electrons occupying the same orbital type on the same nucleus, was included for calculations where more electron localization was desired than provided by the GGA functional alone. 3.5 eV was chosen for U_{eff} as it has been shown to accurately represent the electronic structure of TiO_2 [17].

Three different unit cells were utilized in this study to represent the (101) anatase surface. For single molecule adsorption on the (101) surface, a 3×2 supercell slab, consisting of 108 atoms, corresponding to a 3×1 slab cut along the [010] and [10$\bar{1}$] direction, was utilized. A 4×2 cell consisting of 144 atoms was used for studies of the effect of co-adsorbed H_2O on the behavior of O_2 on TiO_2; in both cases the slabs consist of three Ti-O double layers. This thickness allows for the creation of a sub-surface vacancy without interfering with the frozen bottom layer. Previous work has shown that three double layers are sufficient for calculations involving sub-surface defects [17, 29]. For calculations of supported platinum clusters a two Ti-O double layer thick 144 atom (4×3) supercell slab was used. A cell up to five double layers was constructed, and no significant differences, either electronic or geometric, were found between five and two layer model so the smaller model was chosen to reduce computational costs. This model provides adequate surface area for the 37 atom platinum cluster while still using a unit cell

sufficiently small to be computationally tractable. All cells had at least a 15 Å gap of vacuum between the adsorbed species and the backside of the periodic image of the slab. The active side of the slab was allowed to relax, while the atoms of the bottom double layer for all cells were frozen in their bulk positions to mimic a bulk-like layer. Geometry relaxations were carried out using the quasi-Newton-Raphson method converged to at least 1×10^{-3} eV.

The adsorption energies for O_2 and H_2O adsorbed on TiO_2 surface and Pt cluster supported on TiO_2 surface were estimated from the following equations:

$$E^{ads}_{O_2/TiO_2} = E_{O_2/TiO_2} - E_{TiO_2} - E_{O_2} \qquad (5.7)$$

$$E^{ads}_{H_2O/TiO_2} = E_{H_2O/TiO_2} - E_{TiO_2} - E_{H_2O} \qquad (5.8)$$

$$E^{ads}_{O_2/Pt-TiO_2} = E_{O_2/Pt-TiO_2} - E_{Pt-TiO_2} - E_{O_2} \qquad (5.9)$$

$$E^{ads}_{H_2O/Pt-TiO_2} = E_{H_2O/Pt-TiO_2} - E_{Pt-TiO_2} - E_{H_2O} \qquad (5.10)$$

where E_{TiO_2}, E_{Pt-TiO_2} are the total energies of the slab TiO_2 and Pt cluster supported on TiO_2, E_{O_2/TiO_2}, $E_{O_2/Pt-TiO_2}$ are the total energies of O_2 adsorbed on TiO_2 surface and Pt cluster, E_{H_2O/TiO_2}, $E_{H_2O/Pt-TiO_2}$ are the total energies of H_2O adsorbed on TiO_2 surface and Pt cluster, and E_{O_2}, E_{H_2O} are the total energies of O_2 and H_2O in gas phase.

5.2.2 Experimental methods

The Pt nanoclusters were deposited on the surfaces of TiO_2 P25 nanoparticles by ALD in a fluidized bed reactor (FBR). Methylcyclopentadienyl-(trimethyl) Platinum(IV) ($MeCpPtMe_3$) and oxygen were used as the precursors. Different numbers of ALD cycles of Pt were carried out on TiO_2 particles and the deposited Pt loading was measured by inductively coupled plasma

atomic emission spectroscopy (ICP-AES, Applied Research Laboratories 3410+). A UV/Vis Spectrometer (Ocean optics, USB4000) equipped with 50mm integrating sphere (Ocean optics, ISP-50-8-R-GT) was used to investigate the light absorbance of these composite particles. Their photocatalytic activity was estimated by studying the decomposition kinetics of methylene blue (MB). The MB concentration was measured after periodic time intervals of light irradiation to determine the decrease in MB concentration with reaction time under illumination. The details of the experimental methods have been described previously [12].

5.3 Results and Discussion

5.3.1 Adsorption of O_2 on TiO_2

5.3.1.1 Adsorption of O_2 on the perfect anatase surface

The perfect anatase TiO_2 (101) surface, shown in Figure 5.1a and b, has a stepped structure with coordinatively unsaturated ions. The perfect anatase (101) surface consists of Ti atoms with two different coordinations: a 5-fold-coordinated Ti (5f-Ti) located nearer the vacuum; and a 6-fold (fully) coordinated Ti (6f-Ti) located below 5f-Ti atoms; and three different O atoms: a 2-fold-coordinated bridging position O (2f-O) located furthest into the vacuum, and two different 3-fold coordinated atoms, 3f-O, and 3f'-O, which differ mainly in the extent to which they extend into the vacuum. Previous reports have demonstrated that while a GGA method does well at predicting geometric structures of water and O_2 on TiO_2, it does not accurately represent the electronic structure of the TiO_2 system [17]. To accurately describe the electronic structure, a Hubbard correction must be used. As we are interested in not only the geometries of the TiO_2 surface, but also the electronic structure, a Hubbard correction of U=3.5 eV was imposed on calculations of interactions with the TiO_2 surface. As such, all the data and figures reported in the O_2 on TiO_2 section are from the Hubbard correction calculations.

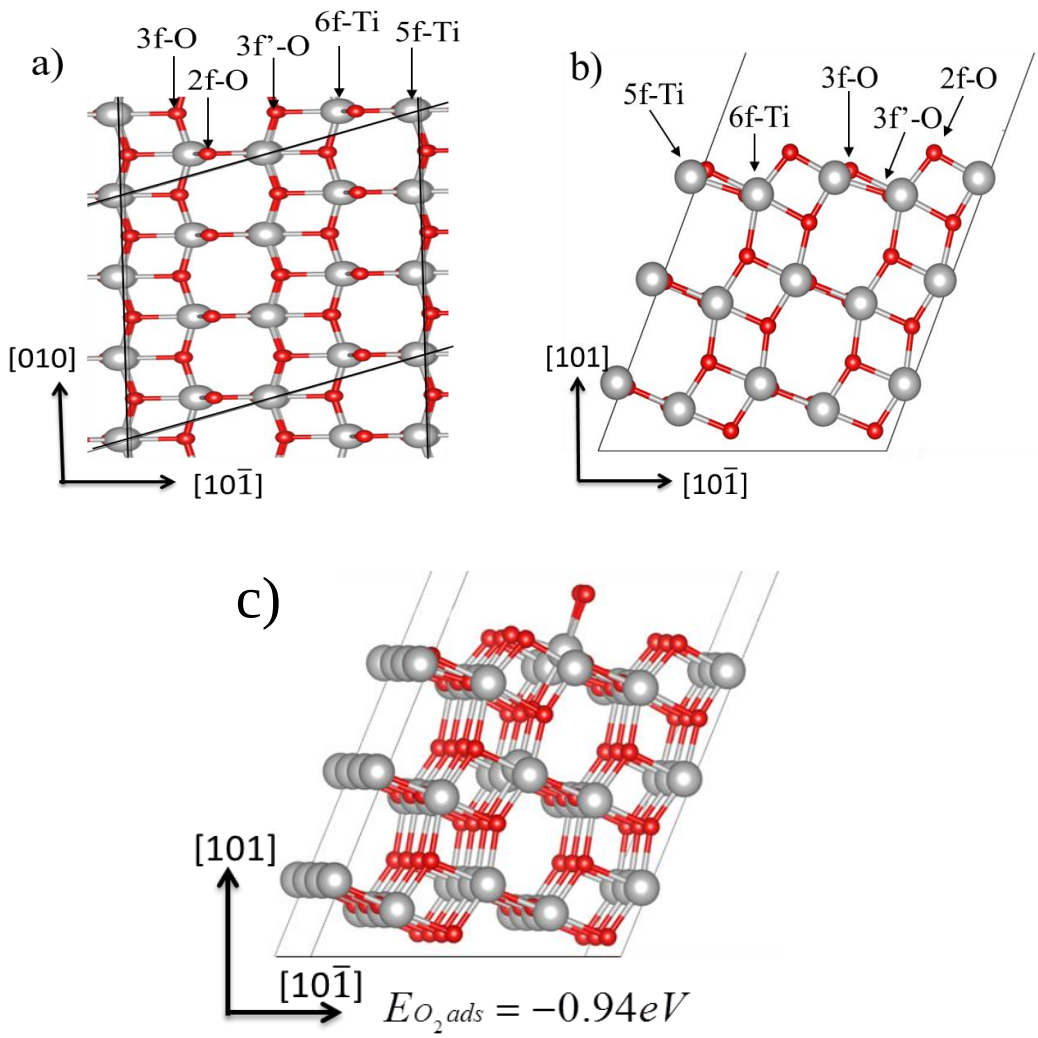

Figure 5.1 a) Top view of the perfect TiO_2 surface b) side view of the perfect TiO_2 surface c) O_2 adsorption on the perfect surface with an additional electron. Large gray atoms are Ti, medium red atoms are oxygen. If viewing in black and white, large light atoms and small dark atoms represent Ti and O, respectively.

As shown previously, O_2 does not adsorb to a perfect, neutral TiO_2 surface [14, 30-32]. Our calculation also shows when O_2 placed on the TiO_2 surface, it relaxes into the vacuum rather than adsorbing to the surface. However, upon interacting with an extra electron in the conduction band of TiO_2 (which is primarily of Ti d character) O_2 chemisorbs to the surface with an adsorption energy of -0.94 eV (see Figure 5.1c). The adsorbed dioxygen is bound to a surface Ti

atom and is parallel to the rows of bridging surface oxygen atoms. Both Ti-O bonds have a length of 2.08 Å while the O-O bond lengthens from 1.23 Å to 1.33 Å upon adsorption, indicative of the formation of the superoxide state of oxygen, which has an O-O bond length of 1.33 Å. When this occurs, the surface Ti atom bound to the adsorbed O_2 relaxes away from the surface with its bonds to the subsurface O atoms lengthening from 1.84 Å to 2.15 Å. This indicates a significant weakening of the Ti-O bonds between the surface Ti to which dioxygen adsorbs and the subsurface O atoms to which the Ti atom is bound.

Although the superoxide O_2^- formally gains a full electron relative to O_2, Bader charge analysis of the adsorbed state predicts that the adsorbing O_2 gains only 0.55 e^- as seen in Table 5.1. We attribute the gain of only 0.55 e^- to the fact that some of the extra electron density is localized on the surface 5f-Ti atom to form bonds to the adsorbing O_2. The projected density of states (PDOS), shown in Figure 5.3a, indicates that the highest energy occupied band is composed of O 2p character from the adsorbed O_2 and Ti 3d character from the 5f-Ti atom to which the O_2 adsorbs, suggesting that Ti-O bonds are of d-p π character. The d-p π bond between the d_{xz} orbital of the 5f-Ti atom and the π_z* antibonding orbital of O_2 leads to additional occupation of what was once one of the two degenerate partially occupied π* HOMO's of O_2. A schematic of the bond is shown in the insert of Figure 5.3a. Additional occupation of the O_2 π* antibonding orbital increases the O_2 bond length to that of superoxide. The lowest energy unoccupied band is composed mostly of O $2p_y$ character from the other O_2 π* antibonding orbital with contributions from the Ti d_{xy} character, also shown in Figure 3a. The transfer of only ~0.5 e to O_2 is a characteristic of the Ti-O_2 d-p π bond that forms between the Ti d_{xz}-orbital and the O_2 π_z* antibonding orbital.

Table 5. 1 The O_2 Bader charge and the O-O, O-Ti and O-Pt bond length upon O_2 adsorption on the perfect TiO_2 surface, defect TiO_2 surface with sub-surface O vacancy, and Pt cluster supported on TiO_2 surface. Positive Bader charge values indicate an increase in the electron density.

System	Perfect TiO_2		Defect TiO_2		Pt/TiO_2	
System charge	1 extra e^-	2 extra e^-	neutral	1 extra e^-	neutral	1 extra e^-
O_2 bader charge upon adsorption (e)	0.55	1.05	0.98	1.02	0.65	0.69
O-O bond length (Å)	1.33	1.46	1.45	1.46	1.40	1.41
O-Ti bond length (Å) (*O-Pt bond for Pt/TiO_2 system)	2.08	1.89	1.87	1.88	1.98	1.98

Upon the addition of a second electron to the supercell mimic of the TiO_2 surface, O_2 acquires an additional 0.50 e^-, giving a total of 1.05 e^-, and the O-O bond lengthens further to 1.46 Å (a comparison of bond lengths is listed in Table 5.1), roughly the length of the peroxide bond (1.49 Å). As indicated by the PDOS analysis shown in Figure 3b the addition of the second electron occupies the state that arise from the O_2 π_y* orbital composed of O $2p_y$-orbitals and Ti $3d_{xy}$ orbitals which is orthogonal to the 5f-Ti d_{xy} – π_y* orbital. The lower energy of the Ti d_{xz}- O π_z* is intuitive, as there is more overlap of the individual atom's orbitals than of the Ti d_{xy}- O π_y* bond leading to increased strength of the Ti d_{xz}- O π^*_z bond.

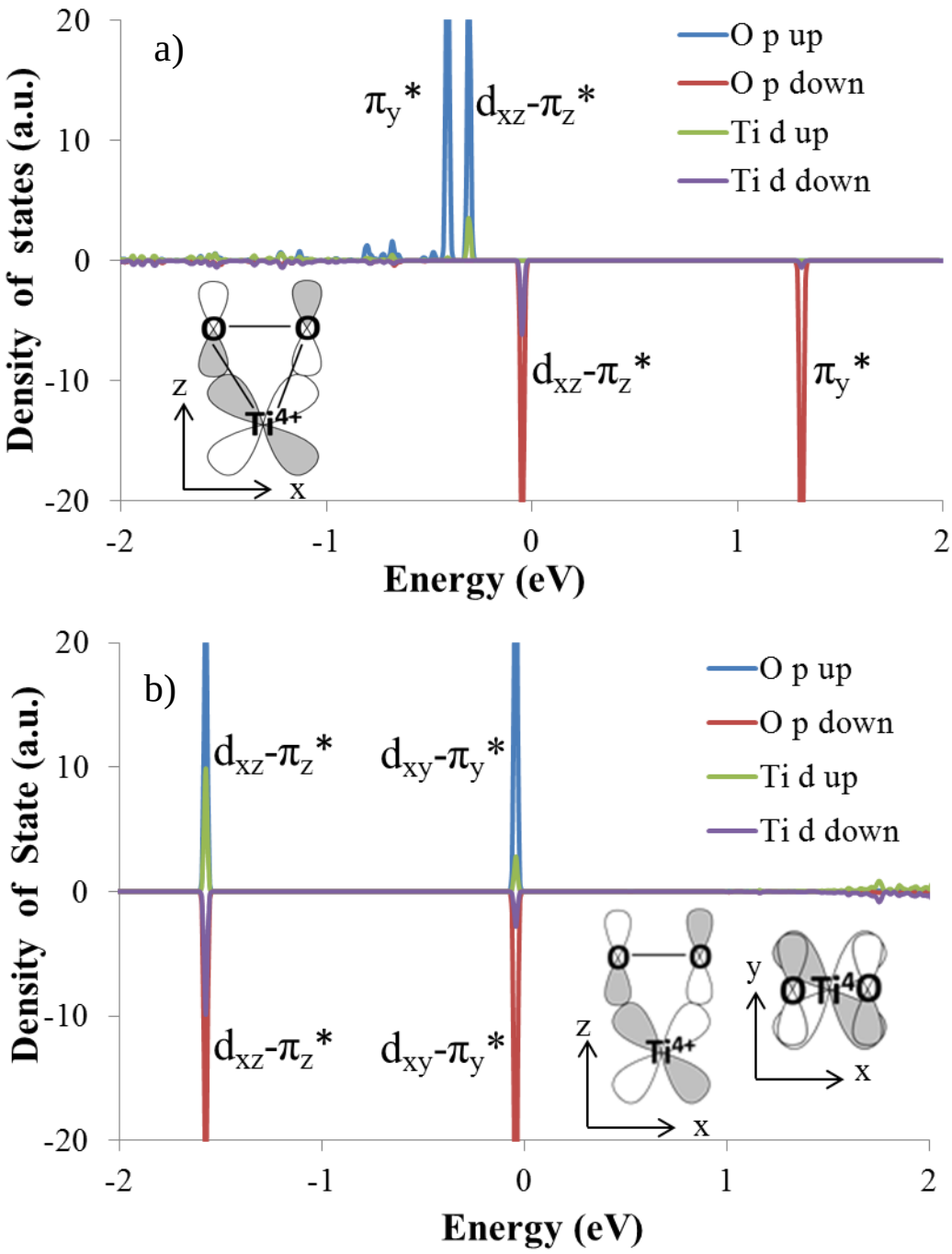

Figure 5.2 PDOS of O_2 on the perfect anatase surface with one additional electron (a) and two additional electrons (b). Insert: displays the molecular orbital interpretation of the highest energy band from the DOS

The fact that an extra electron allows for O_2 adsorption on the perfect anatase (101) surface suggests that if photoexcitation of TiO_2 occurs during sufficient O_2 exposure, O_2 can act as an electron scavenger in the absence of defects. This is consistent with what observed by Berger et al [33]. They observed a greater increase in the O_2^- signal in the EPR spectra upon TiO_2 UV irradiation during exposure to O_2 than that obtained upon UV irradiation of TiO_2 after O_2 was evacuated from the chamber. If the O_2 is removed before irradiation, O_2 is only adsorbed at defects, leading to a small number of adsorbed oxygen species. In contrast, if the irradiation occurs in the presence of O_2, then O_2 can interact with the surface, acquire electron density by electron transfer and adsorb to the surface. This could be the mechanism for electron scavenging in air where a significant flux of impinging O_2 increases the probability that an excited electron is transferred to O_2, hence allowing it to adsorb. In contrast, the probability that O_2 interacts with a free electron in TiO_2 is greatly decreased in an aqueous environment because the concentration of O_2 near the surface and flux of O_2 to the surface are low as the TiO_2 surface is covered by water. We discuss this in detail later.

5.3.1.2 Adsorption of O_2 on anatase with subsurface O vacancy

Because O subsurface vacancy has a formation energy approximately half that of interstitial Ti [32], making much more O vacancies exist than Ti interstitials at equilibrium, we restricted our investigation to TiO_2 surface with sub-surface O vacancy. The TiO_2 surface with a subsurface O vacancy is illustrated in Figures 5.3a and b, where the 6f'-Ti atom is the atom positioned above the subsurface O vacancy, 5f'-Ti is the 5f-Ti atom neighbors the 6f'-Ti, and the Ti atom positioned below the subsurface O vacancy is labeled as B-Ti.

Figure 5.3c shows the structure of O_2 adsorbed on this defect surface, where the O_2 adsorbs at 5f'-Ti and the adsorption energy is -2.53 eV. Upon adsorption, the O-O bond lengthens from its gas phase value of 1.23 Å to 1.45 Å, in good agreement with previous studies [17]. Because this bond is almost the same length as the 1.49 Å O-O bond length of peroxide (O_2^{2-}), one might expect that the adsorbed dioxygen would have an overall charge of 2 e^-. However, Bader charge analysis predicts that O_2 gains only 0.98 e^-. This once again arises from O_2 sharing the electrons in the two d-p π bonds: d_{xz}- π_z* and d_{xy}- π_y* formed with the TiO_2 surface as discussed above. The fact that the Ti-O_2 bonds have ~1 e^- associated with it, rather than the ~0.5 e^- found on the perfect surface with one additional electron explains why the Ti-O_2 bond is 0.21 Å shorter and 1.6 eV stronger than the Ti-O_2 bond on the perfect surface with one photoexcited electron.

In order to understand what occurs when the adsorbed O_2 encounters an excited electron, an e^- was added to the defect containing slab with an adsorbed O_2. We calculated that upon the addition of an extra electron to the slab, the O_2 does not become significantly more strongly adsorbed to the surface O_2's adsorption energy is -2.64eV compared to -2.53eV without the additional election. This indicates that no significant electron density has been transferred to the O_2, or the Ti-O_2 bond, because significant density transfer usually leads to increased adsorption energy, as discussed in the case of O_2 on the perfect surface. The fact that the added electron does not localize on the adsorbed O_2 was confirmed using Bader analysis which shows that the O_2 only gains 0.04 e^- (see Table 5.1), implying the O_2 has likely picked up all of the electron density that it can.

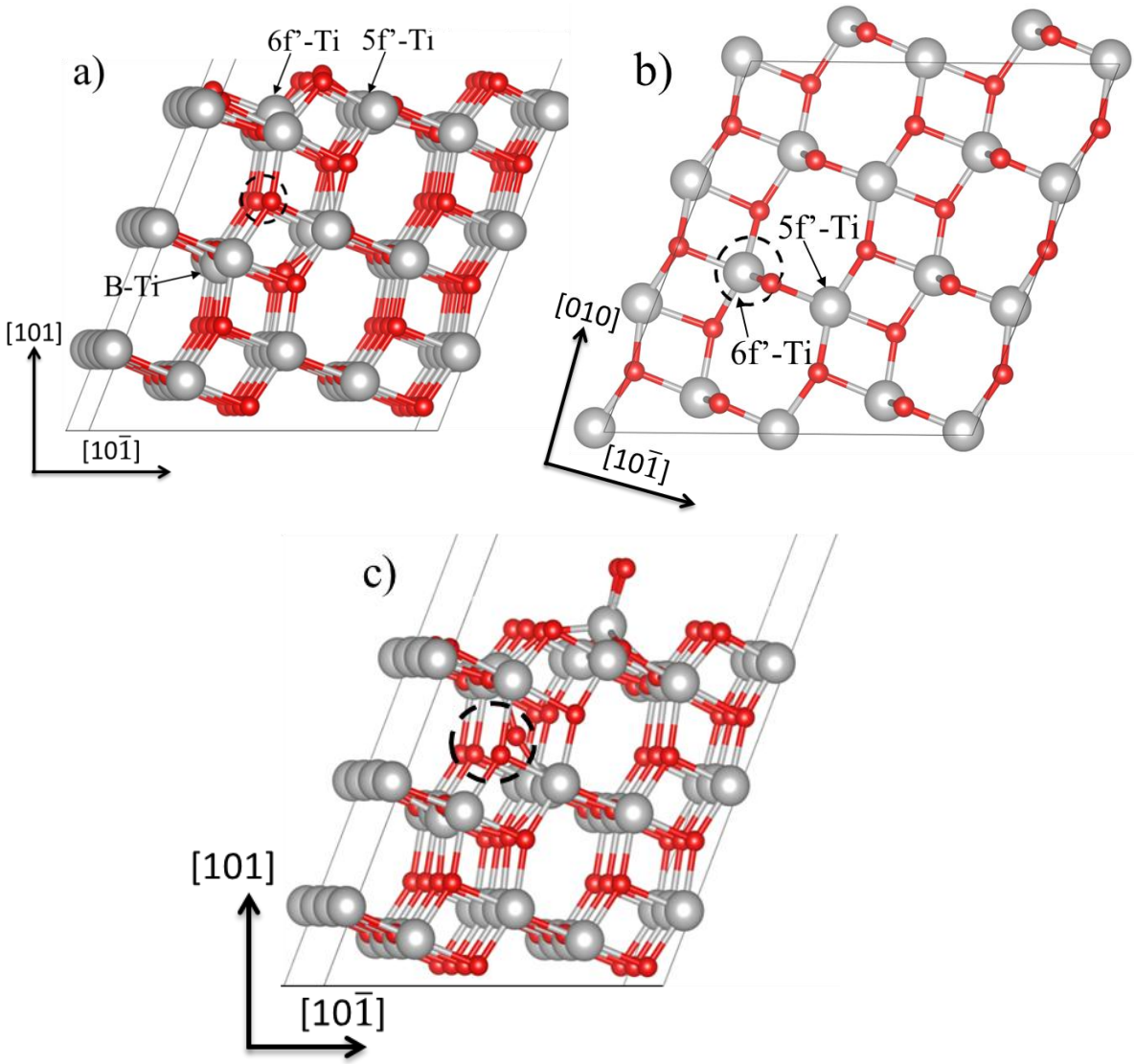

Figure 5.3 a) Top view of TiO_2 with a subsurface O vacancy, location of defect marked with a dashed circle b) side view of TiO_2 with a subsurface O vacancy, location of defect marked with a dashed circle top view of the perfect TiO_2 surface c) O_2 adsorbed at the TiO_2 surface with subsurface O vacancy. Large gray atoms are Ti, medium red atoms are oxygen. If viewing in black and white, large light atoms and small dark atoms represent Ti and O, respectively.

In the removal of organic pollutants from aqueous systems, the defect-free TiO_2 surface will be covered with water because water has a favorable adsorption energy on the perfect TiO_2 surface. We calculated H_2O adsorption energies of -0.88 eV for a single H_2O molecule and -0.86

eV per H_2O for a 2×2 monolayer of water on perfect TiO_2 surface, in agreement with past studies [34]. This, coupled with the low concentrations of O_2 in aqueous phases and transport limitations in liquid, suggests that the probability of O_2 striking a perfect TiO_2 surface site and interacting with an excited electron is negligible. Additionally, there is only a small thermodynamic driving force for O_2 to replace one of the waters on the surface even when there is an additional electron, by -0.12 eV, which is within the error of DFT. Consequently, the most likely locations for O_2/TiO_2 interactions, and hence electron transfer, is at defects that are not occupied by H_2O. Our calculations show that the adsorption energy per H_2O for a monolayer H_2O on the surface with subsurface O vacancies is -0.92 eV, in compassion to that of -0.86 eV on perfect surface, suggesting only a slight preference for adsorption on and around the defect sight. In contrast, O_2 does not adsorb to the perfect, neutral surface but strongly adsorbs near subsurface O vacancies with a calculated adsorption energy of -2.53 eV. When a monolayer of water surrounds an O_2 adsorbed on the defect site the adsorption energy of O_2 becomes to -2.82 eV. Overall, it is downhill in energy for an O_2 in to replace a water molecule on a defect site by -1.87 eV. Since O_2 cannot easily replace an H_2O on the non-defective surface, where water occupies all adsorption sites, but O_2 can replace one at the defect site, suggesting that electron scavenging by O_2 adsorbed near subsurface O vacancy sites is the main path for electron scavenging by O_2 in aqueous TiO_2 systems.

5.3.2 The electronic structure of Pt on TiO_2

A truncated cuboctahedron Pt cluster with 37 atoms was constructed on the (101) anatase TiO_2 surface slab. The Pt cluster has three atomic layers (as shown in Figure 5.4a and b), with 19 atoms in the hexagonal shaped bottom layer, 12 atoms in the middle layer, and 6 atoms in the top

layer. The cluster has an FCC structure with each layer composed of a (111) plane. A Hubbard term on the Ti atoms in the Pt/TiO_2 system was tested to determine whether it had any effect on the predicted structure. As expected, no significant effect on structure was found upon inclusion of the Hubbard interaction. This is likely because Hubbard on-site interaction terms do not localize electrons in metallic systems. As the following study is on the interaction of O_2 and H_2O with the TiO_2 supported Pt cluster and not the semiconducting TiO_2 surface, the Hubbard term does not affect the Pt-O interactions that are of interest and because Hubbard terms increase the computational expense, the following calculations did not employ a Hubbard term.

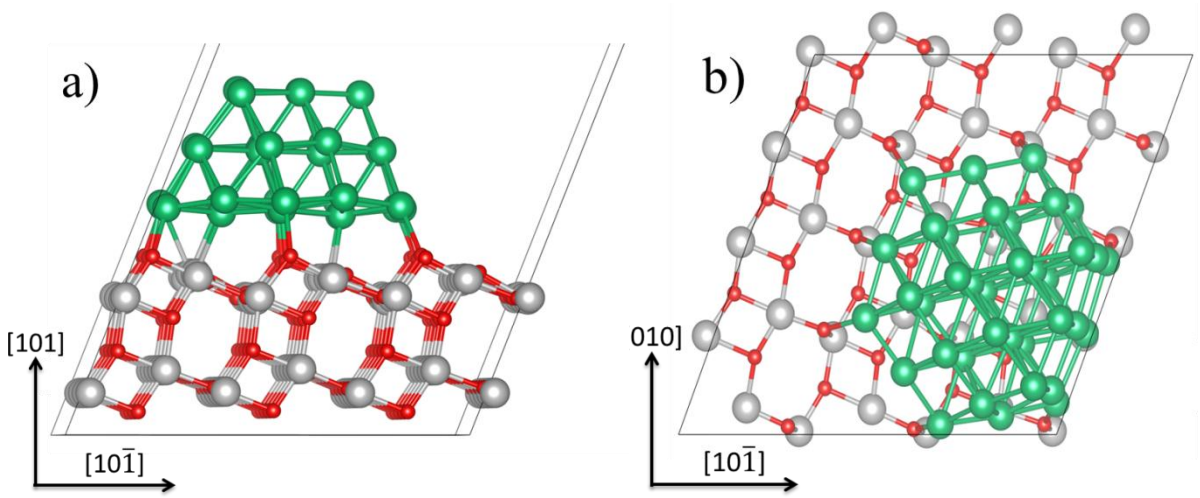

Figure 5.4 a) Side view of 37 atom Pt cluster on the anatase (101) surface, b) top view of 37 atom Pt cluster on the anatase (101) surface. Gray, red and green represent Ti, O and Pt atoms, respectively. If viewing in black and white, large light atoms, small dark atoms and large dark atoms represent Ti, O and Pt respectively.

Bader charge analysis was carried out to study the electronic properties of the Pt cluster supported on TiO_2. As the results in Table 5.2 show, the Pt cluster is positively charged with ~ 1 e when it is supported on the neutral, ground state TiO_2 surface. A detailed delineation of the

charge of each atom shows that the positive charge does not distribute itself equally among the Pt atoms of the cluster, but instead localizes on the Pt atoms in the bottom layer that are directly bonded to O atoms of TiO_2. This is because O has a higher electronegativity than Pt, resulting in Pt atoms losing electron density to neighboring oxygen atoms. On the other hand, the Pt atoms at the interface with TiO_2 adjacent to Ti atoms are slightly negatively charged as they accept electron density from Ti, although significantly less than that withdrawn by interfacial O atoms. To model excitation under UV light, an extra electron or a hole is added to the supercell. We find that the Pt cluster shows similar electron and hole trapping ability, with 0.57 e^- of the added electron and 0.59 e^- of the added hole localized over the Pt cluster. While the added electron or hole is not entirely localized on the Pt cluster when these charges are added to the system separately, the Coulombic attraction of the electron-hole pair makes it likely that Pt fully localizes the quasiparticle. The predicted equal electron and hole trapping ability indicates that the Pt cluster does not act solely as an electron trap as most previous reports have suggested [3, 9, 13, 14].

Table 5.2 Badder charge analysis for addition of an electron or hole into a TiO_2 surface with a Pt cluster. The neutral row shows changes in charge with respect to an isolated 37 atom Pt cluster and isolated TiO_2 slab. The e^- and h^+ addition rows report changes of charge with respect to the neutral system. The negative values indicate an increase in the electron density.

System Charge	Charge Change (e)	
	Pt	TiO_2
neutral	0.98	-0.91
1 extra e^-	-0.57	-0.42
1 extra h^+	0.59	0.40

Figure 5.5 shows the PDOS plots of the bare TiO_2 and the Pt/TiO_2 structures. The energy scale was shifted to align the Fermi level to zero to serve as a reference energy. The Fermi level of bare TiO_2 is at the valence band edge. The band gap of (101) anatase TiO_2 was calculated to be 2.1 eV, which is lower than the experimental value of 3.2 eV. The under estimation of band gaps by DFT is well known [35-37], and is caused by the inaccuracy in describing unoccupied bands and hence an inability to accurately describe the energy required to promote an electron to the unoccupied band. The valence band of TiO_2 is comprised mainly of oxygen 2p character with a minor contribution from Ti 3d orbitals while the conduction band is comprised of major contributions from Ti 3d orbitals and small contributions from O 2p orbitals. With a Pt cluster on the TiO_2 surface, the Fermi level shifts upwards towards TiO_2's conduction band. The distribution of the O and Ti states remain in similar locations relative to one another in the presence of the supported Pt cluster, while a continuum of Pt states now appears within the bandgap. The similar location of Ti and O states with and without Pt suggests that the bandgap of bulk TiO_2 does not change on addition of Pt, but that new states are introduced over the entire band gap so that no bandgap exists for the Pt/TiO_2 system.

The states with energies near the Fermi level are predominately of Pt 5d character. Consequently, when e-h pairs are generated in TiO_2, it is favorable for both the electron and hole to transfer to the Pt cluster as it is energetically favorable for the electron to fill low energy bands and holes to fill bands that are high energy for electrons. This is consistent with the Bader analysis that shows the Pt cluster is both an electron and a hole trap. Additionally, the fact that the electrons and holes can easily relax through the non-segmented density of states, and that Pt states completely bridge TiO_2's band gap, suggest that Pt clusters act as e-h recombination centers. This recombination effect is independent of Pt cluster size; Pt fills the bandgap of TiO_2

even at cluster sizes of only three Pt atoms. As reported by Han et al., and confirmed by our own calculations, the bandgap of the Pt/TiO_2 system disappears for Pt clusters of trimers or larger ones on the surface [14]. Our calculated Pt clusters with sizes greater than three atoms also show a completely filled bandgap. For Pt monomars and dimers, the Pt states mainly localize between the VB and CB and incompletely fill the bandgap. These states reside near the Fermi level and still possess Pt 5d character, leading the excited electron and hole to localize on Pt even for extremely small clusters and even individual Pt atoms. Considering that Pt deposition on TiO_2 produces Pt clusters with average diameters of 1-2 nm, which corresponds to tens to hundreds of Pt atoms, we conclude that Pt clusters act as e-h recombination centers independent of loading, contrary to claims that Pt transforms into an e-h recombination center only after the Pt loading exceeds a specific level.

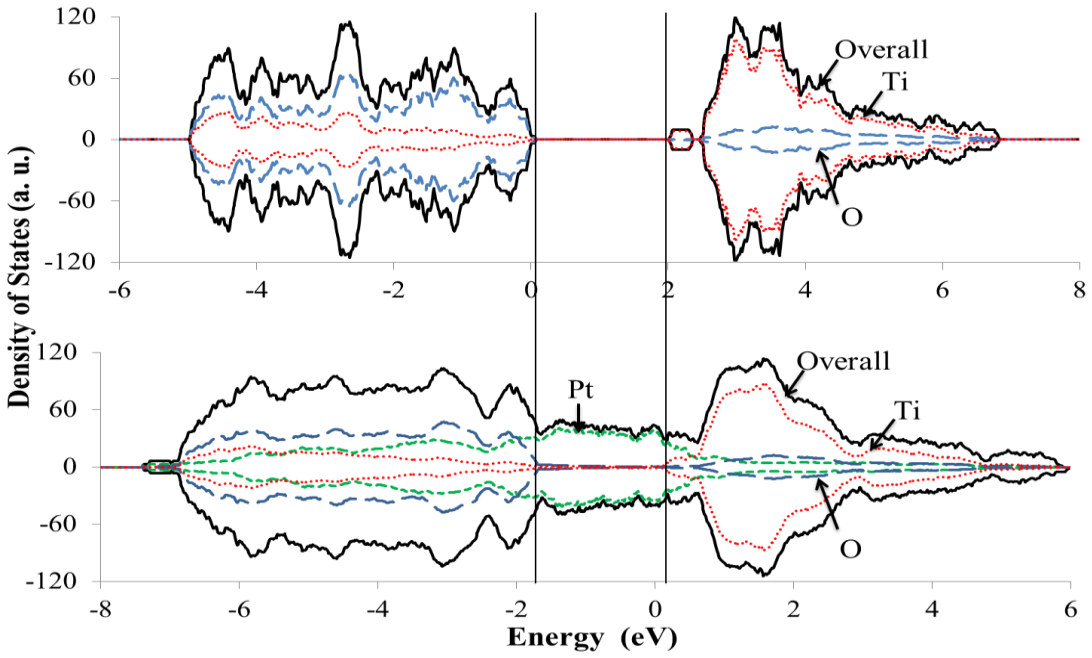

Figure 5.5 a) Projected density of states for a TiO_2 surface and b) Projected density of states for a 37 Pt atom cluster on a TiO_2 surface.

The PDOS of Pt/TiO_2 suggests that the Pt deposited TiO_2 adsorbs visible light. We measured visible light adsorption experimentally, as shown in Figure 5.6, which displays the UV/Vis absorption spectra for bare TiO_2 P25 nanoparticles and Pt/TiO_2 composite particles. The Pt clusters were deposited on TiO_2 particles by using atomic layer deposition (ALD) [12]. As shown in Figure 5.6, TiO_2 absorbs UV light only and no absorption is observed for wavelengths longer than ~385nm, which corresponds to a TiO_2 bandgap of 3.2 eV. However, Pt deposited TiO_2 samples adsorb light in both the UV and whole visible light range. The visible absorption intensity increases with the Pt loading. This result agrees with the behavior predicted by the PDOS plot that shows that the bandgap of the Pt/TiO_2 particles is filled by Pt states, leading to the absorption of low energy visible light. Visible light absorption, however, does not necessarily result in visible light photoactivity. This hypothesis was confirmed by experiment using methylene blue (MB) as the evaluation probe. TiO_2 nanoparticles with 2.96 wt% Pt deposited particles were dispersed in a solution of MB and the relative concentration of MB was measured at various reaction times, as shown in Figure 5.7. The MB degraded much slower under visible light exposure than under UV irradiation. The low rate of MB decomposition can be attributed to Pt's thermal catalytic properties because the decomposition rates under no irradiation and under visible light irradiation are equal. This demonstrates that Pt deposition on TiO_2 does not provide a pathway for visible light photoactivity for MB decomposition. Furthermore, because the PDOS shows that the bandgap of the underlying TiO_2 semiconductor does not change upon Pt deposition, the observed visible light adsorption does not equate to a red shift in TiO_2's bandgap, contrary to previous suggestions[20].

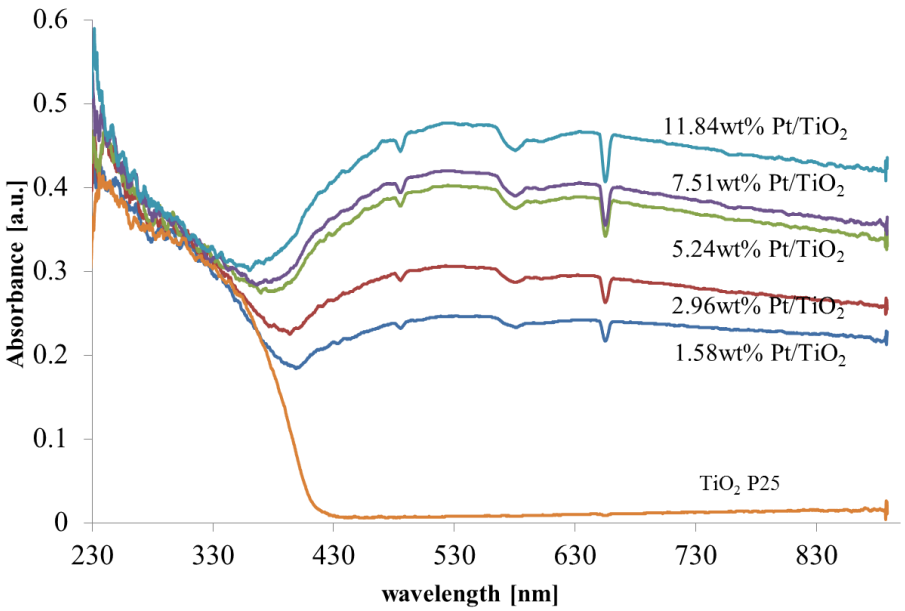

Figure 5.6 Comparison of absorption spectra of TiO_2 P25, and different loading of Pt deposited TiO_2 particles

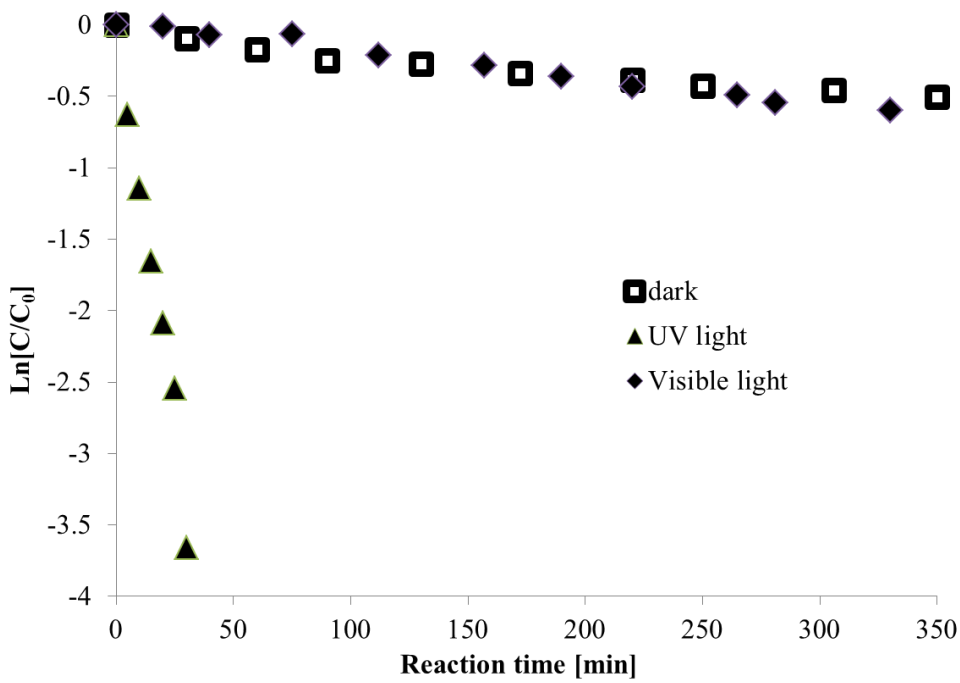

Figure 5.7 MB decomposition rate for Pt/TiO_2 under different light conditions

Visible light absorption over the entire visible spectrum stems from excitations involving Pt metal states, which can absorb light of any wavelength because there is no gap between occupied and unoccupied Pt states. If an e-h pair is generated from the absorption of visible light by Pt, it rapidly recombines within the Pt before it can migrate into TiO_2. So, although visible light absorption by Pt clusters supported on TiO_2 was observed, no visible light photoactivity is expected unless the transfer rate of the electron/hole transfer from Pt to TiO_2 or to a nearby adsorbed species competes with quasi-particle recombination and thermalization.

5.3.3 Adsorption of O_2 on Pt particles supported on Anatase

As discussed above, Pt particles on TiO_2 act as e-h recombination centers independent of Pt loading, which is deleterious to the photoactivity of TiO_2. However, it is well known that Pt enhances the photoactivity of TiO_2 up to an optimal loading. Consequently, at low Pt loadings Pt clusters on TiO_2 must possess an ability to enhance the photoactivity that successfully competes with its acceleration of e-h pair annihilation. Unfortunately, no credible suggestions for what this effect is have been reported. In an attempt to identify the source of the enhanced photoactivity, the adsorption characteristics of O_2 and H_2O on the TiO_2 supported Pt cluster was investigated using DFT. Several different O_2 adsorption configurations and positions were calculated, including a bridging site on top of the cluster, as well as adsorption on the sides and edges of the Pt cluster. The bridge site on the top surface of the Pt cluster was found to be the most energetically favorable, in agreement with previous work on O_2 adsorption on Pt clusters [33-35]. As illustrated in Figure 5.8a, each of the two O atoms forms covalent bonds to its neighboring Pt atom of length 1.98 Å where the O-O bond lies parallel to the Pt-Pt axis between the two Pt atoms to which O_2 adsorbs. The predicted adsorption energy is -1.69 eV, which is significantly

stronger than that of O_2 chemisorbed on the negatively charged (101) anatase surface (-0.94 eV) and the defect-free non-charged surface to which O_2 has no inclination to adsorb (Table 5.3). O_2 adsorption is also greatly enhanced by Pt relative to adsorption on defect TiO_2 surface near O vacancies due to the low concentration of O vacancies at equilibrium. Thus, the deposition of Pt on the TiO_2 greatly increases O_2 adsorption as adsorption is highly favorable and Pt provides multiple sites for O_2 adsorption. In contrast, O_2 on bare TiO_2 requires either photoexcited electrons or defects to provide free electron density. This would be responsible for the ability of Pt to enhance the net rate of electron scavenging by O_2.

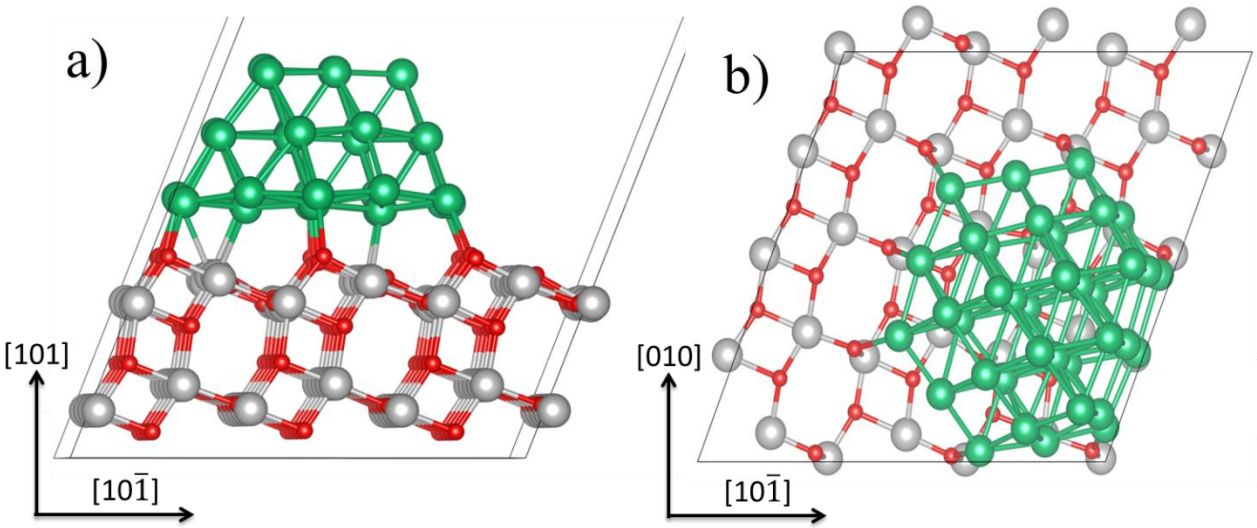

Figure 5.8 a) Side view of O_2 adsorbed on Pt cluster and adsorption energy b) side view of H_2O adsorbed on Pt cluster and adsorption energy. Gray, red and green represent Ti, O and Pt atoms, respectively. If viewing in black and white, large light atoms, small dark atoms and large dark atoms represent Ti, O and Pt respectively.

The O-O bond distance of bridge site adsorbed O_2 is 1.40 Å, which is longer than that of superoxide (1.32 Å), but shorter than that of peroxide (1.49 Å). Furthermore, Bader charge analysis (Table 5.1) shows the adsorbed O_2 gains 0.65 e upon adsorption, which is more than the 0.55 e gained when O_2 adsorbs in a peroxide-like state and less than the 0.98 e gain O_2 adsorbs in

a superoxide like state, as discussed above. This suggests that on adsorption to Pt O_2 partially fills its second π* orbital, suggesting that π* states lie below the highest lying Pt occupied states. The 0.65 gain in charge on O_2 on adsorption to Pt is primarily withdrawn from the Pt cluster, since Bader charge analysis shows that 0.62 e of the 0.65 e gained by O_2 is provided by Pt. This leaves the Pt cluster positively charged with a "hole". Furthermore, population analysis shows this electron density is mostly provided by the two Pt atoms to which the O_2 molecule adsorbs, with each losing ~0.3 e. When an extra electron is subsequently added to the system to mimic a photoexcited electron, the extra electron is not transferred to the adsorbed O_2, as evidenced by only 0.04 e localized in the O_2, as shown in Table 5.1. Instead, the additional electron primarily fills the hole in Pt, as a result of the fact that the LUMO is comprised and the unoccupied O_2 states are at higher energy levels. This is further evidenced by only a slight increase in the O-O bond length after addition of the extra electron to 1.41 Å versus 1.40 Å in neutral system. This suggests that the electron scavenging mechanism involves O_2 removing electrons from Pt to produce a charged O_2 species and a hole in the Pt cluster that can then be annihilated by a photoexcited electron. Therefore, strong adsorption of O_2 to Pt at many adsorption sites and the coupling of adsorption to electron transfer demonstrates that Pt increases photoactivity by providing surface sites for O_2 adsorption that increases electron scavenging and leads to OH ·formation, both of which are key to photocatalytic activity.

Table 5.3 Binding energy comparison for O_2 and H_2O adsorption on perfect TiO_2 and Pt/TiO_2 surface. N/A means the O_2 or H_2O has no inclination to adsorb.

System charge	Neutral			1 extra e^-			1 extra h^+		
system	Perfect TiO_2	defect TiO_2	Pt/TiO_2	Perfect TiO_2	defect TiO_2	Pt/TiO_2	Perfect TiO_2	defect TiO_2	Pt/TiO_2
O_2 (eV)	N/A	-2.52	-1.69	-0.94	-0.64	-1.72	N/A	-1.52	-1.65
H_2O (eV)	-0.88	-0.88	-0.52	-0.83	-0.92	-0.39	-0.96	-1.13	-0.66

When we inject a hole into the supercell describing O_2 adsorbed to Pt, the majority of the additional hole still accumulates within the Pt cluster and is *not* repelled by the Pt cluster although the cluster is already positively charged, as shown in Table 5.4. This indicates that even with O_2 adsorbed on the Pt cluster, both electrons and holes are attracted to the cluster, ruling out the possibility that O_2 adsorbed on Pt prevents the cluster from acting as a recombination center. Therefore, O_2 adsorption does not change the Pt's function as an e-h recombination center, although it facilitates the scavenging of electrons that significantly lowers e-h recombination. When the rate of electron scavenging due to the O_2 adsorption is faster than the rate of e-h recombination photoactivity is enhanced; if on the other hand O_2 adsorption is limited or Pt loading is too high, e-h recombination dominates and decreases photoactivity.

Table 5.4 Bader charge analysis of the effect of O_2 and H_2O adsorbing onto Pt on TiO_2 and the further effects of adding an e^- or h^+ to the system. Negative values indicate an increase in the electron density. The Bader charge change after an e^- or h^+ addition is calculated with respect to the neutral system.

system charge	O_2 on Pt Charge Change (e)			H_2O on Pt Charge Change (e)		
	O_2	Pt	TiO_2	H_2O	Pt	TiO_2
Neutral	-0.65	0.62	0.03	0.11	-0.08	-0.03
1 extra e^-	-0.04	-0.50	-0.46	-0.03	-0.53	-0.44
1 extra h^+	0.05	0.55	0.40	0.03	0.58	0.39

Water adsorption on Pt was also calculated for a single H_2O molecule adsorbed on the Pt cluster, as shown in Figure 5.8b. Adsorbed H_2O aligns so that the O atom is located above a Pt atom and both H atoms are oriented parallel to the two Pt-Pt axis to which H_2O adsorbs and the two neighboring Pt atoms on the top of the cluster. The H-O-H plane is titled by 12.5° from the Pt surface plane. The O-H bond is slightly lengthened to 0.98 Å relative to its length in the H_2O molecule of 0.96 Å, while the H-O-H angle remains constant (104.4° versus 104.5° in the molecule), indicating a molecularly adsorbed state with little perturbation to structure of the adsorbed water. The large O-Pt distance of 2.26 Å suggests that one of oxygen's lone pair π* orbitals donates into Pt d-orbital to form a dative "donor-acceptor" bond, implying weak chemisorption. The calculated H_2O adsorption energy is -0.52 eV, suggesting H_2O does not adsorb as strongly to Pt as it does to TiO_2, nor as strongly as O_2 adsorbs to Pt, by comparing to

the adsorption energy for H_2O adsorbed on bare TiO_2 (-0.88 eV), and the adsorption energy for O_2 adsorbed at bridge sites on Pt (-1.69 eV). So the H_2O will not prevent O_2 from adsorbing on Pt to the extend it does on the perfect (101) anatase surface. As H_2O adsorbs on Pt, it does not accept a significant charge, irrespective of whether the system is neutral, positively or negatively charged, as shown in Table 5.4. This demonstrates that H_2O does not accept the holes that are localized within the Pt cluster. Thus, the likely mechanism for hole removal from the cluster, ignoring recombination which is not a hole transfer process, is direct hole transfer to organic pollutants. Because the H_2O concentration is generally significantly higher than organic chemicals in solution, and because Pt is likely to be covered with H_2O and O_2, the probability of an organic molecule adsorbing to Pt and scavenging a hole is low. Thus, the main pathway for hole removal is likely through acceptors on the TiO_2 surface rather than on the Pt surface. If too much Pt presents, it will block the hole remove sites on TiO_2 surface.

5.4. Conclusions

This study presents a fundamental description of the principles governing the photoactivity of Pt on TiO_2 and aims to provide insight into the effects of deposited Pt on the photoactivity of TiO_2 to clarify several long-held assumptions about this process. For example, many have suggested that the initial increase and subsequent decrease of the photoactivity of TiO_2 with increasing Pt loading results from Pt separating e-h pairs at low loading, but transforming into a recombination center at high Pt loadings. Our calculations demonstrate that this description provides an inaccurate picture of the role of Pt.

As shown above, O_2 does not readily adsorb on the neutral perfect (101) anatase surface, although it does adsorb to the negatively charged surface, for example as would occur when O_2

encounters a surface excited electron. While this may take place often when TiO_2 is exposed to air, the probability is reduced in the aqueous phase where H_2O bonds readily to the TiO_2 surface to block impinging O_2 from the surface. For neutral TiO_2 surfaces without an excited electron, O_2 can adsorb only at defect sites, such as near subsurface O vacancies where O_2 adsorption is more favorable than H_2O adsorption. While these defects act as interaction points for O_2 with the TiO_2 surface, their equilibrium concentration is low owing to their high formation energy of 3.87 eV. This limits the extent of O_2 removing excited electrons from TiO_2 surface.

Our calculations show that Pt clusters deposited on TiO_2 increase O_2 adsorption leading to an increase in the photoactivity of TiO_2 at low Pt loadings. When O_2 adsorbs on the supported Pt cluster, it scavenges electrons and consequently reduces the rate of electron-hole recombination. Additionally, the large number of charged O_2 molecules results in an increase in the number of reactive OH ·radicals in solution that oxidize organic pollutants. This is significant because the electron transfer to oxygen is the rate-limiting step in semiconductor photocatalysis. However, the Pt cluster is itself an e-h recombination center independent of Pt loading; when photoexcitation generates the e-h pair, both the electron and hole readily accumulate on Pt clusters nearly equally enhancing recombination and reducing the photoactivity of TiO_2. When the Pt loading is higher than the optimum loading level, the recombination effect outweighs the positive effect from increased O_2 adsorption, because the O_2 adsorption rate is limited by the concentration of O_2 in the solution and its transport to the Pt surface. In addition, the Pt clusters block the adsorption of H_2O and organics on TiO_2 and hence reduce hole removal. All these factors results in the decreased photocatalytic activity at high Pt loadings. Furthermore, a DOS analysis shows that while Pt doping enables visible light absorption, it does not lead to a red shift of the TiO_2 semiconductor nor to visible light photoactivity, as we confirmed experimentally.

This study clarifies the role of Pt doping on the photoactivity of TiO_2, contributing a significant advance to this important application field.

5.5 References:

1. Cho, K.C., et al., Photocatalytic performance of Pt-loaded TiO2 in the decomposition of gaseous ozone. Journal of Photochemistry and Photobiology a-Chemistry, 2004. 161(2-3): p. 155-161.

2. Mills, A.a.L., SK, Platinum group metals and their oxides in semiconductor photosensitisation. Platinum metals review, 2003. 47(1): p. 2-12.

3. Kryukova, G.N., et al., Structural peculiarities of TiO2 and Pt/TiO2 catalysts for the photocatalytic oxidation of aqueous solution of Acid Orange 7 Dye upon ultraviolet light. Applied Catalysis B-Environmental, 2007. 71(3-4): p. 169-176.

4. Kennedy, J.a.D., AK, Photothermal heterogeneous oxidation of ethanol over Pt/TiO2. Journal of Catalysis, 1998. 179: p. 375-389.

5. Lam, S., et al, The effect of Platinum and Silver deposits in the photocatalytic oxidation of resorcinol. Applied Catalysis B-Environmental, 2007. 72: p. 363-372.

6. Sano, T., et al, Degradation of toluene and acetaldehyde with Pt-loaded TiO2 catalyst and parabolic trough concentrator. Solar enengy, 2004. 77: p. 543-552.

7. Yamakata, A., T. Ishibashi, and H. Onishi, Water- and oxygen-induced decay kinetics of photogenerated electrons in TiO2 and Pt/TiO2: A time-resolved infrared absorption study. Journal of Physical Chemistry B, 2001. 105(30): p. 7258-7262.

8. Li, F.B. and X.Z. Li, The enhancement of photodegradation efficiency using Pt-TiO2 catalyst. Chemosphere, 2002. 48(10): p. 1103-1111.

9. Riassetto, D., C. Holtzinger, and M. Langlet, Influence of platinum nano-particles on the photocatalytic activity of sol-gel derived TiO2 films. Journal of Materials Science, 2009. 44(10): p. 2637-2646.

10. Gray, K.A., et al., The Effects of Pt Doping on the Structure and Visible Light Photoactivity of Titania Nanotubes. Journal of Physical Chemistry C, 2010. 114(49): p. 21262-21269.

11. Ikuma, Y. and H. Bessho, Effect of Pt concentration on the production of hydrogen by a TiO2 photocatalyst. International Journal of Hydrogen Energy, 2007. 32(14): p. 2689-2692.

12. Zhou, Y., et al., Optimal preparation of Pt/TiO2 photocatalysts using atomic layer deposition. Applied Catalysis B-Environmental, 2010. 101(1-2): p. 54-60.

13. Ding, X.J., et al., Preparation and characterization of hydrophobic TiO2 pillared clay: The effect of acid hydrolysis catalyst and doped Pt amount on photocatalytic activity. Journal of Colloid and Interface Science, 2008. 320(2): p. 501-507.

14. Han, F., et al., Tailored titanium dioxide photocatalysts for the degradation of organic dyes in wastewater treatment: A review. Applied Catalysis a-General, 2009. 359(1-2): p. 25-40.

15. Hoffmann, M.R., et al., Environmental Applications of Semiconductor Photocatalysis. Chemical Reviews, 1995. 95(1): p. 69-96.

16. Gerischer, H. and A. Heller, The Role of Oxygen in Photooxidation of Organic-Molecules on Semiconductor Particles. Journal of Physical Chemistry, 1991. 95(13): p. 5261-5267.

17. Aschauer, U., J. Chen, and A. Selloni, Peroxide and superoxide states of adsorbed O-2 on anatase TiO2 (101) with subsurface defects. Physical Chemistry Chemical Physics, 2010. 12(40): p. 12956-12960.

18. Gong, X.Q., et al., Small au and pt clusters at the anatase TiO2(101) surface: Behavior at terraces, steps, and surface oxygen vacancies. Journal of the American Chemical Society, 2008. 130(1): p. 370-381.

19. Remita, H., et al., Modification of titanium dioxide with platinum ions and clusters: Application in photocatalysis. Journal of Physical Chemistry C, 2008. 112(4): p. 1124-1131.

20. Sun, B., P.G. Smirniotis, and P. Boolchand, Visible light photocatalysis with platinized rutile TiO2 for aqueous organic oxidation. Langmuir, 2005. 21(24): p. 11397-11403.

21. Yi, Z., et al., Photocatalytic performance of plasma sprayed Pt-modified TiO2 coatings under visible light irradiation. Catalysis Communications, 2007. 8(6): p. 906-912.

22. Hoffmann, M.R., J. Choi, and H. Park, Effects of Single Metal-Ion Doping on the Visible-Light Photoreactivity of TiO(2). Journal of Physical Chemistry C, 2010. 114(2): p. 783-792.

23. Kresse, G., et al., Efficient iterative schemes for ab initio total-energy calculations using a plane-wave basis set. Physical Review B, 1996. 54(16): p. 11169.

24. Kresse, G. and J. Furthmüller, Efficiency of ab-initio total energy calculations for metals and semiconductors using a plane-wave basis set. Computational Materials Science, 1996. 6(1): p. 15-50.

25. Perdew, J.P., K. Burke, and M. Ernzerhof, Generalized Gradient Approximation Made Simple. Physical Review Letters, 1996. 77(18): p. 3865.

26. Henkelman, G., A. Arnaldsson, and H. Jónsson, A fast and robust algorithm for Bader decomposition of charge density. Computational Materials Science, 2006. 36(3): p. 354-360.

27. Sanville, E., et al., Improved grid-based algorithm for Bader charge allocation. Journal of Computational Chemistry, 2007. 28(5): p. 899-908.

28. Hubbard, J., ELECTRON CORRELATIONS IN NARROW ENERGY BANDS. Proceedings of the Royal Society of London Series a-Mathematical and Physical Sciences, 1963. 276(1364): p. 238-+.

29. Cheng, H. and A. Selloni, Surface and subsurface oxygen vacancies in anatase TiO_{2} and differences with rutile. Physical Review B, 2009. 79(9): p. 092101.

30. Filippone, F., G. Mattioli, and A.A. Bonapasta, Reaction intermediates and pathways in the photoreduction of oxygen molecules at the (1 0 1) TiO2 (anatase) surface. Catalysis Today, 2007. 129(1-2): p. 169-176.

31. Zhang, L., et al., Oxygen adsorption on anatase surfaces and edges. Applied Surface Science, 2011. 257(20): p. 8402-8408.

32. Aschauer, U., et al., Influence of Subsurface Defects on the Surface Reactivity of TiO2: Water on Anatase (101). Journal of Physical Chemistry C, 2010. 114(2): p. 1278-1284.

33. Berger, T., et al., Light-Induced Charge Separation in Anatase TiO2 Particles. The Journal of Physical Chemistry B, 2005. 109(13): p. 6061-6068.

34. He, Y., et al., Local ordering and electronic signatures of submonolayer water on anatase TiO2(101). Nat Mater, 2009. 8(7): p. 585-589.

35. Miller, K.L., et al., Effects of water and formic acid adsorption on the electronic structure of anatase TiO2 (101). Journal of Physical Chemistry C, 2011.

36. Qu, Z.W. and G.J. Kroes, Theoretical study of stable, defect-free (TiO2)(n) nanoparticles with n=10-16. Journal of Physical Chemistry C, 2007. 111(45): p. 16808-16817.

37. Labat, F., et al., Density functional theory analysis of the structural and electronic properties of TiO2 rutile and anatase polytypes: Performances of different exchange-correlation functionals. Journal of Chemical Physics, 2007. 126(15).

CHAPTER 6

Summary, Conclusions and Recommendations

6.1 Conclusions and Recommendations

This dissertation focuses on the TiO_2 photocatalyst and it's modification by Pt doping using the atomic layer deposition (ALD). Experimental and theoretical studies are included to thoroughly investigate the effect of Pt doping on the photoactivity of TiO_2 and the particle growth mechanism for Pt ALD.

The experimental work includes two major parts: one is TiO_2 thin films deposition on magnetic cores to create magnetic photocatalysts; the other is Pt deposition on TiO_2 photocatalyst to increase the photoactivity. For the first part, in order to recycle and reuse TiO_2 photocatalyst for water treatment, nanosized magnetic photocatalyst particles were synthesized to combine the TiO_2 photoactivity and the magnetic separation. The overall method to produce the passivated and functionalized magnetic photocatalyst particles included four steps. First, the particle size of the original feed iron oxalate particles was decreased by a milling process. The solvent-based cryogenic milling was demonstrated to be highly efficient at breaking down powders and achieving small particle size distributions. Second, iron nanoparticles were synthesized by decomposing the milled iron oxalate powders at high temperature in a reducing gas environment in a fluidized bed reactor (FBR). Due to the high surface area, the iron nanoparticles were unstable and spontaneously oxidized when exposed to oxidized precursor during TiO_2 ALD processing, leading to the reduced magnetic moment of the core particles. So, as an improvement in the process, a subsequent passivation step was to coat the iron particles via an *in-situ* AlN ALD prior to TiO_2 deposition. This oxygen-free film protects the iron core

particles and significantly reduced the iron oxidation as determined by X-ray diffraction and magnetization measurements. After the AlN ALD, the final step is to deposit TiO_2 film in the same FBR to provide the particles with a photocatalytic property. The TiO_2 ALD proceeded at 100 ^oC with $TiCl_4$ and H_2O_2 as precursors. Coupling the photoactivity with the magnetic property, this nanocomposite material is believed to be promising for the applications involving environmental treatment.

For this part, as a small amount of iron oxide still exists after the AlN passivation, several options might be available to help to achieve better performance. One is to increase the thickness of the AlN film in order to achieve an improved passivation effect. The insufficient thickness of AlN may allow the exposure of the underlying iron particles to the strong oxidizing TiO_2 ALD precursor. However, thicker AlN films might reduce the magnetic property of the iron core. Other nitride films can be applied to study their passivation effect, such as TiN, to optimize the passivation effect with least film thickness. Finally, using milder oxygen-containing precursors for TiO_2 ALD may also help.

Second, in order to increase the photoactivity of TiO_2, Platinum (Pt) was deposited on the TiO_2 photocatalyst nanoparticles by the ALD technique using Methylcyclopentadienyl-(trimethyl) Platinum(IV) ($MeCpPtMe_3$) and oxygen as precursors. ALD was demonstrated to be an excellent method for depositing Pt nanoparticles on TiO_2 particle surfaces. The Pt clusters were nanosized and retained a high level of dispersion. Pt ALD was carried out over a deposition temperature range of 150 - 400 ℃. The effect of operating temperature was investigated by studying the Pt deposition rate, the resulting carbon impurity levels, and the variation in photocatalytic activity. The lower temperature limit for Pt ALD was found to be approximately 200 ℃. When the temperature was below 200 ℃, the low temperature limit of Pt ALD, the $MeCpPtMe_3$ precursor

ligands were not removed by the subsequent O_2 dosing. This results in no continuous MB decomposition beyond five minutes of UV light irradiation. When the deposition temperature was at or above 200 ℃, all of the single-cycle Pt/TiO_2 samples exhibited significantly higher photoactivity than that of uncoated TiO_2. The highest MB decomposition rate was achieved at 320 ℃ with Pt loading 0.6 wt%, which is threefold of the decomposition rate result from pure TiO_2. This level of improvement far exceeds that attainable using other Pt incorporation techniques, especially at such low loading. Different cycles of Pt ALD were deposited on TiO_2 at 400°C, and the photoactivity was observed to increase at beginning with Pt loading and then reach a maximum at 3 cycles of Pt ALD deposited sample. This highest photoactivity, equivalent to the photoactivity deposited by 1 cycle of Pt ALD at 320°C, while the Pt loading is about 2.5 times that of the latter. With more than three ALD cycles of Pt deposition, the photoactivity decreased with the Pt loading further increasing. The Pt ALD method demonstrated in this work can be potentially used for the facile fabrication of TiO_2 photocatalyst particles loaded with highly dispersed Pt nanoparticles, resulting in enhanced photoactivity under optimized deposition conditions.

This Pt work can supply insights to other metal ALD and photoactivity studies. Although many reports have suggested that Pt provides the best improvement to the photoactivity of TiO_2 among different metal dopings[1-4], the expensive nature of Pt increases the overall cost of the catalyst. So, if other metals or their oxides, such as Fe, Mn, Ni, Co, can be deposited by the ALD method on TiO_2 surfaces with high dispersion, it would be valuable to study their effect on the photoactivity of TiO_2.

The above experimental study raised two main questions. One is why Pt ALD generates Pt clusters, for the first tens or hundreds of cycles, rather than thin films, more typical ofALD.

The other is why the photoactivity of Pt/TiO_2 first increases and then decreases with increasing Pt loading, reaching a maximum at an optimum weight loading. In order to fundamentally answer the two questions, theoretical study based on the DFT method was applied to thoroughly understand the mechanism of Pt growth and its effect on the photoactivity of TiO_2. Theoretical studies have become a widely used tool to interpret experimental results and to furnish new insights for experiments. Especially, Ab initio pesudopotential calculations based on DFT have become an invaluable theoretical tool in describing materials and molecular systems at a sufficient level of accuracy over several decades.

The theoretical work includes two major parts, with each one answering one question. In order to understand the Pt particle growth mechanism, the geometry of the Pt cluster on the TiO_2 surface and the diffusion of Pt atoms were studied using first principle DFT calculations. Pt_n clusters with n up to 37 atoms were calculated and the most stable configurations among the calculated structures were identified. Due to large cohesive energy, Pt prefers to form 3D structures rather than 2D structures or monolayers on the TiO_2 surface. The clustering energy decreases with Pt cluster size and approaches the bulk Pt cohesive energy as the cluster size approaches infinity. The monotonic energy decrease trend suggests that large clusters are always thermodynamically favorable. However, it is not exactly as what we observed in the Pt ALD, which shows that the Pt particles become much denser while the particle size doesn't increase proportionally after 20 cycles of ALD, compared to 1 cycle samples. Kinetic limitations were found to be responsible for that. The activation barriers for a single Pt adatom hopping along the surface bridge oxygen row and across the bridge oxygen rows were calculated to be above 1 eV for both directions, leading to limited Pt diffusion over the TiO_2 surface. The desorption energy barrier for a Pt atom detaching from a Pt_{38} cluster was calculated to be 2.12 eV.

This large barrier would slow the Pt Ostwald ripening process. Therefore, although large particles are thermodynamically favorable, the high desorption barrier and low diffusion rate would limit the Pt detaching from small particles and then diffusing to large particles, leading to the presence of a large number of small particles during the Pt ALD growth. This diffusion study also reveals that Pt atoms can be trapped at certain surface sites; as a result the sintering process is extremely slow at room temperature.

This theoretical study thoroughly explores the Pt cluster growth and diffusion characteristics, which are significant for the Pt/TiO_2 application as a heterogeneous catalyst and provides insight for other studies related with transition metal ALD growth and heterogeneous catalysis. For example, the method to understand the Pt/TiO_2 interaction can be applied to study other metal/support system. If the metal growth mechanism on a certain support is fundamentally understood, this knowledge could directly guide one to choose the proper metal and support and, thus, save experimental time and expense.

The second part of the theoretical study presents a fundamental description of the principles governing the photoactivity of Pt/TiO_2 and provides insight into the effects of deposited Pt on the photoactivity of TiO_2. The calculations show the largest positive effect on photoactivity driven by Pt is the increase of O_2 adsorption due to the high O_2 adsorption energy of -1.69 eV and large number of adsorption sites on the Pt cluster. This results in enhanced photocatalytic performance because the increased O_2 can increase the interfacial electron transfer rate, which is the rate-limiting step in semiconductor photocatalysis [5]. O_2 does not readily adsorb on the neutral perfect (101) anatase surface, unless a negatively charged surface exists, which could be from photoexcited electrons or surface defects. In aqueous solutions, O_2/TiO_2 interactions are rare because water covers the surface. On the other hand, deposition of Pt

clusters on the surface greatly increases the number of available sites for O_2 adsorption, and, thus, the net rate of electron scavenging. However, the Pt cluster is itself an e-h recombination center independent of Pt loading. When the Pt loading is higher than the optimum loading level, the recombination effect outweighs the positive effect from increased O_2 adsorption, because the O_2 adsorption rate is limited by the O_2 concentration in the solution and its transport to the Pt surface. In addition, the Pt clusters block TiO_2 adsorption sites for H_2O and organics, the hole acceptors. Therefore, the photoactivity of Pt/TiO_2 is decreased when the Pt loading is too high. Furthermore, a DOS analysis shows that while Pt doping enables visible light absorption, it does not lead to a red shift of the TiO_2 semiconductor nor to visible light photoactivity, as confirmed by experiment.

This study clarifies the role of Pt doping on the photoactivity of TiO_2, contributing a significant advance to this important application field. As we more clearly understand the effect of Pt doping on the photoactivity of TiO_2, we can optimize the Pt doping and reaction situation to achieve maximum photocatalytic performance. However, due to the limitation of the DFT, for instance the size of the slab was limited to below 200 atoms and the TiO_2 surface was restricted to anatase TiO_2 (101) surface, this study only qualitatively describes the role of Pt doping. If quantitive understanding is desired to distinguish at which Pt loading and O_2 concentration the highest photoactivity could be achieved, the experimental study would need to be carried out.

6.2 References

1. Sano, T., et al., Photocatalytic degradation of gaseous acetaldehyde on TiO2 with photodeposited metals and metal oxides. Journal of Photochemistry and Photobiology a-Chemistry, 2003. 160(1-2): p. 93-98.

2. Lee, S.L. and J. Scott, Gas-phase phtocatalytic degradation of volatile organic compounds using metallised titania, in Chemeca 2007. 2007: Australis.

3. Sivalingam, G., et al., Photocatalytic degradation of various dyes by combustion synthesized nano anatase TiO2. Applied Catalysis B-Environmental, 2003. **45**(1): p. 23-38.

4. Cho, K., et al, Photocatalytic performance of Pt-loaded TiO2 in the decomposition of gaseous ozone. Journal of Photochemistry and Photobiology a-Chemistry, 2004. **161**: p. 155-161.

5. Gerischer, H. and A. Heller, The Role of Oxygen in Photooxidation of Organic-Molecules on Semiconductor Particles. Journal of Physical Chemistry, 1991. **95**(13): p. 5261-5267.

BIBLIOGRAPHY

1. Aaltonen, T., et al., Reaction mechanism studies on atomic layer deposition of ruthenium and platinum. Electrochemical and Solid State Letters, 2003. 6(9): p. C130-C133.

2. Aaltonen, T., et al., Atomic layer deposition of platinum thin films. Chemistry of Materials, 2003. 15(9): p. 1924-1928.

3. Aaltonen, T., et al., Atomic layer deposition of noble metals: Exploration of the low limit of the deposition temperature. Journal of Materials Research, 2004. 19(11): p. 3353-3358.

4. Aarik, J., et al., Atomic layer deposition of titanium dioxide from TiCl4 and H2O: investigation of growth mechanism. Applied Surface Science, 2001. 172(1-2): p. 148-158.

5. Abida, B., et al., Preparation and characterization of Pt/TiO(2) nanotubes catalyst for methanol electro-oxidation. Applied Catalysis B-Environmental, 2011. 106(3-4): p. 609-615.

6. Argaman, N. and G. Makov, Density functional theory: An introduction. American Journal of Physics, 2000. 68(1): p. 69-79.

7. Aschauer, U., J. Chen, and A. Selloni, Peroxide and superoxide states of adsorbed O(2) on anatase TiO(2) (101) with subsurface defects. Physical Chemistry Chemical Physics, 2010. 12(40): p. 12956-12960.

8. Aschauer, U., J. Chen, and A. Selloni, Peroxide and superoxide states of adsorbed O-2 on anatase TiO2 (101) with subsurface defects. Physical Chemistry Chemical Physics, 2010. 12(40): p. 12956-12960.

9. Aschauer, U., et al., Influence of Subsurface Defects on the Surface Reactivity of TiO2: Water on Anatase (101). Journal of Physical Chemistry C, 2010. 114(2): p. 1278-1284.

10. Augugliaro, V., Litter,M., ect, The combination of heterogeneous photocatalysis with chemical and physical operations: A tool for improving the photoprocess performance. Journal of Photochemistry and Photobiology C: photochemistry reviews, 2006. 7: p. 127-144.

11. Badylevich, M., et al., Electronic structure of the interface of aluminum nitride with Si(100). Journal of Applied Physics, 2008. 104(9): p. -.

12. Bartram, M.E., et al., Nucleation and Growth of Ain - Self-Limiting Reactions and the Regeneration of Active-Sites Using Sequential Exposures of Trimethylaluminum and Ammonia on Silica at 600 K. Chemistry of Materials, 1993. 5(10): p. 1424-1430.

13. Bedzyk, M.J., et al., Controlled Growth of Platinum Nanoparticles on Strontium Titanate Nanocubes by Atomic Layer Deposition. Small, 2009. 5(6): p. 750-757.

14. Berger, T., et al., Light-Induced Charge Separation in Anatase TiO2 Particles. The Journal of Physical Chemistry B, 2005. 109(13): p. 6061-6068.

15. Bertolet, D.C. and J.W. Rogers, Mechanistics of Early Stage Growth of Aln on Alumina - Tmal and Nh3. Chemistry of Materials, 1993. 5(3): p. 391-395.

16. Blake, D., ed. Bibliography of work on photocatalytic removal of hazardous compounds from water and air 1999, national renewable energy laboratory.

17. Capelle, K., A bird's-eye view of density-functional theory. Brazilian Journal of Physics, 2006. 36(4A): p. 1318-1343.

18. Castellani, N.J., et al., Theoretical modeling of photocatalytic active species on illuminated TiO2. Applied Surface Science, 2007. 254(1): p. 32-35.

19. Chen, X. and S.S. Mao, Titanium dioxide nanomaterials: Synthesis, properties, modifications, and applications. Chemical Reviews, 2007. 107(7): p. 2891-2959.

20. Chen, X.B. and S.S. Mao, Synthesis of titanium dioxide (TiO2) nanomaterials. Journal of Nanoscience and Nanotechnology, 2006. 6(4): p. 906-925.

21. Cheng, H. and A. Selloni, Surface and subsurface oxygen vacancies in anatase TiO_{2} and differences with rutile. Physical Review B, 2009. 79(9): p. 092101.

22. Cheng, H.E., C.M. Hsu, and Y.C. Chen, Substrate Materials and Deposition Temperature Dependent Growth Characteristics and Photocatalytic Properties of ALD TiO2 Films. Journal of the Electrochemical Society, 2009. 156(8): p. D275-D278.

23. Cheng, H.S., et al., Structural evolution of subnano platinum clusters. International Journal of Quantum Chemistry, 2007. 107(1): p. 219-224.

24. Cheng, H.Z. and A. Selloni, Energetics and diffusion of intrinsic surface and subsurface defects on anatase TiO(2)(101). Journal of Chemical Physics, 2009. 131(5).

25. Cho, K., et al, Photocatalytic performance of Pt-loaded TiO2 in the decomposition of gaseous ozone. Journal of Photochemistry and Photobiology a-Chemistry, 2004. 161: p. 155-161.

26. Cho, K.C., et al., Photocatalytic performance of Pt-loaded TiO2 in the decomposition of gaseous ozone. Journal of Photochemistry and Photobiology a-Chemistry, 2004. 161(2-3): p. 155-161.

27. Christensen, S.T., et al., Nanoscale Structure and Morphology of Atomic Layer Deposition Platinum on SrTiO3 (001). Chemistry of Materials, 2009. 21(3): p. 516-521.

28. Climent, M.J., A. Corma, and S. Iborra, Converting carbohydrates to bulk chemicals and fine chemicals over heterogeneous catalysts. Green Chemistry, 2011. 13(3): p. 520-540.

29. Cramer, C.J., Essentials of comutational chemistry. 2004.

30. Cross, E.K.U. and R.M. Dreizler, eds. Density Functional Theory. 1995.

31. Deskins, N.A., D.H. Mei, and M. Dupuis, Adsorption and diffusion of a single Pt atom on gamma-Al(2)O(3) surfaces. Surface Science, 2009. 603(17): p. 2793-2807.

32. Ding, X.J., et al., Preparation and characterization of hydrophobic TiO2 pillared clay: The effect of acid hydrolysis catalyst and doped Pt amount on photocatalytic activity. Journal of Colloid and Interface Science, 2008. 320(2): p. 501-507.

33. Einaga, H., S. Futamura, and T. Ibusuki, Improvement of catalyst durability in benzene photooxidation by rhodium deposition on TiO2. Chemistry Letters, 2001(6): p. 582-583.

34. Falconer, J.L.a.M.-B., KA, Photocatalytic and thermal catalytic oxidation of acetaldehyde on Pt/TiO2. Journal of Catalysis, 1998. 179: p. 171-178.

35. Farnood, R. and P. Azadi, Review of heterogeneous catalysts for sub- and supercritical water gasification of biomass and wastes. International Journal of Hydrogen Energy, 2011. 36(16): p. 9529-9541.

36. Farrell, D., S.A. Majetich, and J.P. Wilcoxon, Preparation and characterization of monodisperse Fe nanoparticles. Journal of Physical Chemistry B, 2003. 107(40): p. 11022-11030.

37. Filippone, F., G. Mattioli, and A.A. Bonapasta, Reaction intermediates and pathways in the photoreduction of oxygen molecules at the (1 0 1) TiO2 (anatase) surface. Catalysis Today, 2007. 129(1-2): p. 169-176.

38. Floro, J.A., et al., The dynamic competition between stress generation and relaxation mechanisms during coalescence of Volmer-Weber thin films. Journal of Applied Physics, 2001. 89(9): p. 4886-4897.

39. Fujimoto, M., et al., Resistivity and resistive switching properties of Pr0.7Ca0.3MnO3 thin films. Applied Physics Letters, 2006. 89(24).

40. Galan, M.A., et al., Simulation three-way catalyst ageing - Analysis of two conventional catalyst. Applied Catalysis B-Environmental, 2003. 44(1): p. 41-52.

41. Ge, M.F., et al., Geometrical and electronic structure of the Pt-7 cluster: A density functional study. Journal of Physical Chemistry A, 2004. 108(17): p. 3806-3812.

42. George, S.M., Atomic Layer Deposition: An Overview. Chemical Reviews, 2010. 110(1): p. 111-131.

43. George, S.M., et al., Nucleation and growth of Pt atomic layer deposition on Al(2)O(3) substrates using (methylcyclopentadienyl)-trimethyl platinum and O(2) plasma. Journal of Applied Physics, 2011. 109(8).

44. George, S.M., et al., Surface chemistry and film growth during TiN atomic layer deposition using TDMAT and NH3. Thin Solid Films, 2003. 436(2): p. 145-156.

45. George, S.M., A.W. Ott, and J.W. Klaus, Surface chemistry for atomic layer growth. Journal of Physical Chemistry, 1996. 100(31): p. 13121-13131.

46. Gerischer, H. and A. Heller, The Role of Oxygen in Photooxidation of Organic-Molecules on Semiconductor Particles. Journal of Physical Chemistry, 1991. 95(13): p. 5261-5267.

47. Gong, X.Q. and A. Selloni, Role of steps in the reactivity of the anatase TiO2(101) surface. Journal of Catalysis, 2007. 249(2): p. 134-139.

48. Gong, X.Q., et al., Small au and pt clusters at the anatase TiO2(101) surface: Behavior at terraces, steps, and surface oxygen vacancies. Journal of the American Chemical Society, 2008. 130(1): p. 370-381.

49. Gratzel, M., Efficient Water Cleavage by Visible-Light in Colloidal Solutions of Bifunctional Redox Catalysts. Abstracts of Papers of the American Chemical Society, 1981. 181(Mar): p. 13-Inor.

50. Gray, K.A., et al., The Effects of Pt Doping on the Structure and Visible Light Photoactivity of Titania Nanotubes. Journal of Physical Chemistry C, 2010. 114(49): p. 21262-21269.

51. Hafner, J., Materials simulations using VASP - a quantum perspective to materials science. Computer Physics Communications, 2007. 177(1-2): p. 6-13.

52. Hafner, J., Ab-initio simulations of materials using VASP: Density-functional theory and beyond. Journal of Computational Chemistry, 2008. 29(13): p. 2044-2078.

53. Hakim, L.F., et al., Nanoparticle coating for advanced optical, mechanical and rheological properties. Advanced Functional Materials, 2007. 17(16): p. 3175-3181.

54. Hakim, L.F., et al., Aggregation behavior of nanoparticles in fluidized beds. Powder Technology, 2005. 160(3): p. 149-160.

55. Hakim, L.F., et al., Synthesis of oxidation-resistant metal nanoparticles via atomic layer deposition. Nanotechnology, 2007. 18(34): p. -.

56. Han, F., et al., Tailored titanium dioxide photocatalysts for the degradation of organic dyes in wastewater treatment: A review. Applied Catalysis a-General, 2009. 359(1-2): p. 25-40.

57. Hara, M., Environmentally Benign Production of Biodiesel Using Heterogeneous Catalysts. Chemsuschem, 2009. 2(2): p. 129-135.

58. Hashimoto, K., H. Irie, and A. Fujishima, TiO2 photocatalysis: A historical overview and future prospects. Japanese Journal of Applied Physics Part 1-Regular Papers Brief Communications & Review Papers, 2005. 44(12): p. 8269-8285.

59. He, Y., et al., Local ordering and electronic signatures of submonolayer water on anatase TiO2(101). Nat Mater, 2009. 8(7): p. 585-589.

60. Henkelman, G., A. Arnaldsson, and H. Jónsson, A fast and robust algorithm for Bader decomposition of charge density. Computational Materials Science, 2006. 36(3): p. 354-360.

61. Herrmann, J.M., Heterogenous photocatalysis: an emerging technology for water treatment. Catalysis Today, 1993. 17: p. 7-20.

62. Herrmann, J.M., Heterogeneous photocatalysis: State of the art and present applications. Topics in Catalysis, 2005. 34(1-4): p. 49-65.

63. Herrmann, J.M., From catalysis by metals to bifunctional photocatalysis. Topics in Catalysis, 2006. 39(1-2): p. 3-10.

64. Hersam, M.C., et al., Nanoscale Structure and Morphology of Atomic Layer Deposition Platinum on SrTiO(3) (001). Chemistry of Materials, 2009. 21(3): p. 516-521.

65. Hiehata, K., A. Sasahara, and H. Onishi, Local work function analysis of Pt/TiO2 photocatalyst by a Kelvin probe force microscope. Nanotechnology, 2007. 18(8): p. -.

66. Hinchliffe, A., ed. Computational quantum chemistry. 1989.

67. Hirata, H., et al., Characterization and dynamic behavior of precious metals in automotive exhaust gas purification catalysts. Catalysis Today, 2011. 164(1): p. 467-473.

68. Hoffmann, M.R., J. Choi, and H. Park, Effects of Single Metal-Ion Doping on the Visible-Light Photoreactivity of TiO(2). Journal of Physical Chemistry C, 2010. 114(2): p. 783-792.

69. Hoffmann, M.R., et al., Environmental Applications of Semiconductor Photocatalysis. Chemical Reviews, 1995. 95(1): p. 69-96.

70. Hoover, R.R. and Y.V. Tolmachev, Electrochemical Properties of Pt Coatings on Ni Prepared by Atomic Layer Deposition. Journal of the Electrochemical Society, 2009. 156(1): p. A37-A43.

71. Hubbard, J., ELECTRON CORRELATIONS IN NARROW ENERGY BANDS. Proceedings of the Royal Society of London Series a-Mathematical and Physical Sciences, 1963. 276(1364): p. 238-+.

72. Ikuma, Y. and H. Bessho, Effect of Pt concentration on the production of hydrogen by a TiO2 photocatalyst. International Journal of Hydrogen Energy, 2007. 32(14): p. 2689-2692.

73. Inagaki, M., et al., Photocatalytic activity of anatase powders for oxidation of methylene blue in water and diluted NO gas. Applied Catalysis B-Environmental, 2004. 51(4): p. 247-254.

74. Inagaki, M., et al., Preparation of stable anatase-type TiO2 and its photocatalytic performance. International Journal of Inorganic Materials, 2001. 3(7): p. 809-811.

75. Inagaki, M., et al., Dependence of photocatalytic activity of anatase powders on their crystallinity. Chemosphere, 2006. 64(3): p. 437-445.

76. Ishitani, O., et al., Photocatalytic Reduction of Carbon-Dioxide to Methane and Acetic-Acid by an Aqueous Suspension of Metal-Deposited Tio2. Journal of Photochemistry and Photobiology a-Chemistry, 1993. 72(3): p. 269-271.

77. Kennedy, J.a.D., AK, Photothermal heterogeneous oxidation of ethanol over Pt/TiO2. Journal of Catalysis, 1998. 179: p. 375-389.

78. Kessels, W.M.M., et al., Surface reactions during atomic layer deposition of Pt derived from gas phase infrared spectroscopy. Applied Physics Letters, 2009. 95(1).

79. Kim, H., H.B.R. Lee, and W.J. Maeng, Applications of atomic layer deposition to nanofabrication and emerging nanodevices. Thin Solid Films, 2009. 517(8): p. 2563-2580.

80. Kim, K.H., et al., Atomic layer deposition of insulating nitride interfacial layers for germanium metal oxide semiconductor field effect transistors with high-kappa oxide/tungsten nitride gate stacks. Applied Physics Letters, 2007. 90(21).

81. King, D.M., et al., Atomic layer deposition of UV-absorbing ZnO films on SiO(2) and TiO(2) nanoparticles using a fluidized bed reactor. Advanced Functional Materials, 2008. 18(4): p. 607-615.

82. King, D.M., et al., Low-temperature atomic layer deposition of ZnO films on particles in a fluidized bed reactor. Thin Solid Films, 2008. 516(23): p. 8517-8523.

83. King, D.M., et al., Atomic layer deposition of TiO2 films on particles in a fluidized bed reactor. Powder Technology, 2008. 183(3): p. 356-363.

84. King, D.M., et al., Atomic layer deposition on particles using a fluidized bed reactor with in situ mass spectrometry. Surface & Coatings Technology, 2007. 201(22-23): p. 9163-9171.

85. King, D.M., et al., In situ synthesis of TiO2-functionalized metal nanoparticles. Industrial & Engineering Chemistry Research, 2009. 48(1): p. 352-360.

86. King, J.S., et al., Ultralow loading Pt nanocatalysts prepared by atomic layer deposition on carbon aerogels. Nano Letters, 2008. 8(8): p. 2405-2409.

87. Kraeutler, B. and A.J. Bard, Heterogeneous Photocatalytic Synthesis of Methane from Acetic-Acid - New Kolbe Reaction Pathway. Journal of the American Chemical Society, 1978. 100(7): p. 2239-2240.

88. Kresse, G., et al., Efficient iterative schemes for ab initio total-energy calculations using a plane-wave basis set. Physical Review B, 1996. 54(16): p. 11169.

89. Kresse, G. and J. Furthmüller, Efficiency of ab-initio total energy calculations for metals and semiconductors using a plane-wave basis set. Computational Materials Science, 1996. 6(1): p. 15-50.

90. Kresse, G. and D. Joubert, From ultrasoft pseudopotentials to the projector augmented-wave method. Physical Review B, 1999. 59(3): p. 1758-1775.

91. Kryukova, G.N., et al., Structural peculiarities of TiO2 and Pt/TiO2 catalysts for the photocatalytic oxidation of aqueous solution of Acid Orange 7 Dye upon ultraviolet light. Applied Catalysis B-Environmental, 2007. 71(3-4): p. 169-176.

92. Labat, F., et al., Density functional theory analysis of the structural and electronic properties of TiO2 rutile and anatase polytypes: Performances of different exchange-correlation functionals. Journal of Chemical Physics, 2007. 126(15).

93. Lam, S., et al, The effect of Platinum and Silver deposits in the photocatalytic oxidation of resorcinol. Applied Catalysis B-Environmental, 2007. 72: p. 363-372.

94. Law, S., The effect of Platinum and Silver deposits in the photocatalytic oxidation of resorcinol. Applied Catalysis B-Environmental, 2007. 72: p. 363-372.

95. Lee, S.K., Platinum and palladium in semiconductor photocatalytic systems. Platinum metals review 2003. 47(2): p. 61-72.

96. Lee, S.L. and J. Scott, Gas-phase phtocatalytic degradation of volatile organic compounds using metallised titania, in Chemeca 2007. 2007: Australis.

97. Li, F.B. and X.Z. Li, The enhancement of photodegradation efficiency using Pt-TiO2 catalyst. Chemosphere, 2002. 48(10): p. 1103-1111.

98. Li, G.X., et al., Study of Pt/TiO(2) nanocomposite for cancer-cell treatment. Journal of Photochemistry and Photobiology B-Biology, 2010. 98(3): p. 207-210.

99. Liang, X.H., S.M. George, and A.W. Weimer, Synthesis of a novel porous Polymer/Ceramic composite material by low-temperature atomic layer deposition. Chemistry of Materials, 2007. 19(22): p. 5388-5394.

100. Liang, X.H., et al., Novel processing to produce polymer/ceramic nanocomposites by atomic layer deposition. Journal of the American Ceramic Society, 2007. 90(1): p. 57-63.

101. Liang, X.H., et al., Alumina atomic layer deposition nanocoatings on primary diamond particles using a fluidized bed reactor. Diamond and Related Materials, 2008. 17(2): p. 185-189.

102. Lin, Y.H., et al., Enhancing the Photon-Sensing Properties of ZnO Nanowires by Atomic Layer Deposition of Platinum. Electrochemical and Solid State Letters, 2010. 13(12): p. K93-K95.

103. Litter, M.I. and J.A. Navio, Photocatalytic properties of iron-doped titania semiconductors. Journal of Photochemistry and Photobiology a-Chemistry, 1996. 98(3): p. 171-181.

104. Liu, C.J., Y. Han, and Q.F. Ge, Interaction of Pt clusters with the anatase TiO2(101) surface: A first principles study. Journal of Physical Chemistry B, 2006. 110(14): p. 7463-7472.

105. Liu, C.W., C.C.; Kei C.C.; Hsueh, Y.C.; Perng, T.P., Atomic ayer deposition of platinum nanoparticles on carbon nanotubes for application in proton-exchange membrane fuel cells, in Fuel cells. 2009. p. No.x,1-4.

106. Manke, C., et al., Atomic vapor deposition of Ru and RuO2 thin film layers for electrode applications. Microelectronic Engineering, 2005. 82(3-4): p. 242-247.

107. Mayer, T.M., J.W. Rogers, and T.A. Michalske, Mechanism of Nucleation and Atomic Layer Growth of Aln on Si. Chemistry of Materials, 1991. 3(4): p. 641-646.

108. Miller, K.L., et al., Effects of water and formic acid adsorption on the electronic structure of anatase TiO2 (101). Journal of Physical Chemistry C, 2011.

109. Mills, A., Platinisation of Semiconductor Particles. J.Chem.Soc.,Chem.Commun., 1982: p. 367.

110. Mills, A.a.L., SK, Platinum group metals and their oxides in semiconductor photosensitisation. Platinum metals review, 2003. 47(1): p. 2-12.

111. Mills, G., H. Jonsson, and G.K. Schenter, Reversible Work Transition-State Theory - Application to Dissociative Adsorption of Hydrogen. Surface Science, 1995. 324(2-3): p. 305-337.

112. Neyman, K.M., A. Bruix, and F. Illas, Adsorption, Oxidation State, and Diffusion of Pt Atoms on the CeO(2)(111) Surface. Journal of Physical Chemistry C, 2010. 114(33): p. 14202-14207.

113. Ngomsik, A.F., et al., Magnetic nano- and microparticles for metal removal and environmental applications: a review. Comptes Rendus Chimie, 2005. 8(6-7): p. 963-970.

114. Niinisto, L., et al., Advanced electronic and optoelectronic materials by Atomic Layer Deposition: An overview with special emphasis on recent progress in processing of high-k dielectrics and other oxide materials. Physica Status Solidi a-Applied Research, 2004. 201(7): p. 1443-1452.

115. Payne, M.C., et al., Iterative Minimization Techniques for Abinitio Total-Energy Calculations - Molecular-Dynamics and Conjugate Gradients. Reviews of Modern Physics, 1992. 64(4): p. 1045-1097.

116. Perdew, J.P., K. Burke, and M. Ernzerhof, Generalized Gradient Approximation Made Simple. Physical Review Letters, 1996. 77(18): p. 3865.

117. Pirkanniemi, K. and M. Sillanpaa, Heterogeneous water phase catalysis as an environmental application: a review. Chemosphere, 2002. 48(10): p. 1047-1060.

118. Pore, V., et al., Atomic layer deposition of TiO2-xNx thin films for photocatalytic applications. Journal of Photochemistry and Photobiology a-Chemistry, 2006. 177(1): p. 68-75.

119. Pore, V., et al., Atomic layer deposition of photocatalytic TiO2 thin films from titanium tetramethoxide and water. Chemical Vapor Deposition, 2004. 10(3): p. 143-148.

120. Puurunen, R.L., Surface chemistry of atomic layer deposition: A case study for the trimethylaluminum/water process. Journal of Applied Physics, 2005. 97(12): p. -.

121. Puurunen, R.L., et al., Successive reactions of gaseous trimethylaluminium and ammonia on porous alumina. Physical Chemistry Chemical Physics, 2001. 3(6): p. 1093-1102.

122. Puurunen, R.L., et al., Growth of aluminum nitride on porous alumina and silica through separate saturated gas-solid reactions of trimethylaluminum and ammonia. Chemistry of Materials, 2002. 14(2): p. 720-729.

123. Puurunen, R.L.R., A.; Sarv, P.; et al, Growth of aluminium nitride on porous silica by atomic layer chemical vapour deposition. Applied Surface Science, 2000. 165: p. 193-202.

124. Qiang, Y., et al., Iron/iron oxide core-shell nanoclusters for biomedical applications. Journal of Nanoparticle Research, 2006. 8(3-4): p. 489-496.

125. Qu, Z.W. and G.J. Kroes, Theoretical study of stable, defect-free (TiO2)(n) nanoparticles with n=10-16. Journal of Physical Chemistry C, 2007. 111(45): p. 16808-16817.

126. Ratke, L. and P.W. Voorhees, Growth and coarsening: ripening in material processing. 2002.

127. Remita, H., et al., Modification of titanium dioxide with platinum ions and clusters: Application in photocatalysis. Journal of Physical Chemistry C, 2008. 112(4): p. 1124-1131.

128. Ren, M.M., R. Ravikrishna, and K.T. Valsaraj, Photocatalytic degradation of gaseous organic species on photonic band-gap titania. Environmental Science & Technology, 2006. 40(22): p. 7029-7033.

129. Riassetto, D., C. Holtzinger, and M. Langlet, Influence of platinum nano-particles on the photocatalytic activity of sol-gel derived TiO2 films. Journal of Materials Science, 2009. 44(10): p. 2637-2646.

130. Roh, Y., et al., HfO2 gate insulator formed by atomic layer deposition for thin-film-transistors. Thin Solid Films, 2007. 515(12): p. 5109-5112.

131. Ropo, M., K. Kokko, and L. Vitos, Assessing the Perdew-Burke-Ernzerhof exchange-correlation density functional revised for metallic bulk and surface systems. Physical Review B, 2008. 77(19).

132. Roudgar, A., L.Y. Wang, and M. Eikerling, Ab Initio Study of Stability and Site-Specific Oxygen Adsorption Energies of Pt Nanoparticles. Journal of Physical Chemistry C, 2009. 113(42): p. 17989-17996.

133. Sano, T., et al, Degradation of toluene and acetaldehyde with Pt-loaded TiO2 catalyst and parabolic trough concentrator. Solar enengy, 2004. 77: p. 543-552.

134. Sano, T., et al., Effect of Pd-photodeposition over TiO2 on product selectivity in photocatalytic degradation of vinyl chloride monomer. Journal of Molecular Catalysis a-Chemical, 2002. 189(2): p. 263-270.

135. Sano, T., et al., Photocatalytic degradation of gaseous acetaldehyde on TiO2 with photodeposited metals and metal oxides. Journal of Photochemistry and Photobiology a-Chemistry, 2003. 160(1-2): p. 93-98.

136. Sanville, E., et al., Improved grid-based algorithm for Bader charge allocation. Journal of Computational Chemistry, 2007. 28(5): p. 899-908.

137. Sauls, F.C., L.V. Interrante, and Z.P. Jiang, Me3al.Nh3 Formation and Pyrolytic Methane Loss - Thermodynamics, Kinetics, and Mechanism. Inorganic Chemistry, 1990. 29(16): p. 2989-2996.

138. Serpone, N., et al., Subnanosecond Relaxation Dynamics in Tio2 Colloidal Sols (Particle Sizes R(P)=1.0-13.4 Nm) - Relevance to Heterogeneous Photocatalysis. Journal of Physical Chemistry, 1995. 99(45): p. 16655-16661.

139. Serrano, B. and H. deLasa, Photocatalytic degradation of water organic pollutants. Kinetic modeling and energy efficiency. Industrial & Engineering Chemistry Research, 1997. 36(11): p. 4705-4711.

140. Shu, C., N. Sukumar, and C.P. Ursenbach, Adsorption of O-2 on TiO2(110): A theoretical study. Journal of Chemical Physics, 1999. 110(21): p. 10539-10544.

141. Sivalingam, G., et al., Photocatalytic degradation of various dyes by combustion synthesized nano anatase TiO2. Applied Catalysis B-Environmental, 2003. 45(1): p. 23-38.

142. Sun, B., P.G. Smirniotis, and P. Boolchand, Visible light photocatalysis with platinized rutile TiO2 for aqueous organic oxidation. Langmuir, 2005. 21(24): p. 11397-11403.

143. Suntola, T., Atomic Layer Epitaxy. Acta Polytechnica Scandinavica-Electrical Engineering Series, 1989(64): p. 242-270.

144. Suntola, T., Atomic Layer Epitaxy. Thin Solid Films, 1992. 216(1): p. 84-89.

145. Suntola, T. and J. Hyvarinen, Atomic Layer Epitaxy. Annual Review of Materials Science, 1985. 15: p. 177-195.

146. Tartaj, P., et al., The preparation of magnetic nanoparticles for applications in biomedicine. Journal of Physics D-Applied Physics, 2003. 36(13): p. R182-R197.

147. Toyoda, M., et al., Effect of crystallinity of anatase on photoactivity for methyleneblue decomposition in water. Applied Catalysis B-Environmental, 2004. 49(4): p. 227-232.

148. Truong, T.N., V. Shapovalov, and E.V. Stefanovich, Nature of the excited states of the rutile TiO2(110) surface with adsorbed water. Surface Science, 2002. 498(1-2): p. L103-L108.

149. Tsouris, C., et al., Surfactant effects on the mechanism of particle capture in high-gradient magnetic filtration. Separation and Purification Technology, 2006. 51(2): p. 201-209.

150. Valden, M., X. Lai, and D.W. Goodman, Onset of catalytic activity of gold clusters on titania with the appearance of nonmetallic properties. Science, 1998. 281(5383): p. 1647-1650.

151. Valdes, A., et al., Oxidation and photo-oxidation of water on TiO2 surface. Journal of Physical Chemistry C, 2008. 112(26): p. 9872-9879.

152. Vidotti, M., et al., Platinum nanoparticle-modified electrodes, morphologic, and electrochemical studies concerning electroactive materials deposition. Journal of Solid State Electrochemistry, 2010. 14(4): p. 675-679.

153. Vlachos, D.G. and Y. Chen, Hydrogenation of Ethylene and Dehydrogenation and Hydrogenolysis of Ethane on Pt(111) and Pt(211): A Density Functional Theory Study. Journal of Physical Chemistry C, 2010. 114(11): p. 4973-4982.

154. Vlachos, D.G., M. Salciccioli, and Y. Chen, Microkinetic Modeling and Reduced Rate Expressions of Ethylene Hydrogenation and Ethane Hydrogenolysis on Platinum. Industrial & Engineering Chemistry Research, 2011. 50(1): p. 28-40.

155. Vorontsov, A.V., E.N. Savinov, and Z.S. Jin, Influence of the form of photodeposited platinum on titania upon its photocatalytic activity in CO and acetone oxidation. Journal of Photochemistry and Photobiology a-Chemistry, 1999. 125(1-3): p. 113-117.

156. Wang, S.B., Application of solid ash based catalysts in heterogeneous catalysis. Environmental Science & Technology, 2008. 42(19): p. 7055-7063.

157. Weimer, A.W., et al., Atomic layer deposition of TiO2 films on particles in a fluidized bed reactor. Powder Technology, 2008. 183(3): p. 356-363.

158. Weimer, A.W., et al., Atomic layer deposition on particles using a fluidized bed reactor with in situ mass spectrometry. Surface & Coatings Technology, 2007. 201(22-23): p. 9163-9171.

159. Weimer, A.W., et al., Highly dispersed Pt nanoparticle catalyst prepared by atomic layer deposition. Applied Catalysis B-Environmental, 2010. 97(1-2): p. 220-226.

160. Weimer, A.W., et al., Alumina atomic layer deposition nanocoatings on primary diamond particles using a fluidized bed reactor. Diamond and Related Materials, 2008. 17(2): p. 185-189.

161. Witkin, D.B. and E.J. Lavernia, Synthesis and mechanical behavior of nanostructured materials via cryomilling. Progress in Materials Science, 2006. 51(1): p. 1-60.

162. Yamakata, A., T. Ishibashi, and H. Onishi, Water- and oxygen-induced decay kinetics of photogenerated electrons in TiO2 and Pt/TiO2: A time-resolved infrared absorption study. Journal of Physical Chemistry B, 2001. 105(30): p. 7258-7262.

163. Yang, H. and Z.M. Peng, Designer platinum nanoparticles: Control of shape, composition in alloy, nanostructure and electrocatalytic property. Nano Today, 2009. 4(2): p. 143-164.

164. Yi, Z., et al., Photocatalytic performance of plasma sprayed Pt-modified TiO2 coatings under visible light irradiation. Catalysis Communications, 2007. 8(6): p. 906-912.

165. Yin, S.F., et al., The direct transformation of carbon dioxide to organic carbonates over heterogeneous catalysts. Applied Catalysis a-General, 2009. 366(1): p. 2-12.

166. Yu, J., L.Qi, and M. Jaroniec, Hydrogen Production by Photocatalytic Water Splitting over Pt/TiO2 Nanosheets with Exposed (001) Facets. J.phys.Chem.C, 2010. 114(30): p. 13118-13125.

167. Zhang, L., et al., Oxygen adsorption on anatase surfaces and edges. Applied Surface Science, 2011. 257(20): p. 8402-8408.

168. Zhao, J. and X.D. Yang, Photocatalytic oxidation for indoor air purification: a literature review. Building and Environment, 2003. 38(5): p. 645-654.

169. Zhao, W., et al., Photodegradation of sulforhodamine-B dye in platinized titania dispersions under visible light irradiation: Influence of platinum as a functional co-catalyst. Journal of Physical Chemistry B, 2002. 106(19): p. 5022-5028.

170. Zhong, H., Y. Yang, and C.X. Tian, Photocatalytic mechanisms of modified titania under visible light. Research on Chemical Intermediates, 2011. 37(1): p. 91-102.

171. Zhou, Y., et al., Optimal preparation of Pt/TiO2 photocatalysts using atomic layer deposition. Applied Catalysis B-Environmental, 2010. 101(1-2): p. 54-60.